Titre: Title:	Innovative Millimeter-Wave Components Based on Mixed Substrate Integrated Dielectric-Metallic Waveguides
Auteur: Author:	Jawad Arif Al Attari
Date:	2013
Type:	Mémoire ou thèse / Dissertation or Thesis
Référence: Citation:	Al Attari, J. A. (2013). Innovative Millimeter-Wave Components Based on Mixed Substrate Integrated Dielectric-Metallic Waveguides [Ph.D. thesis, École Polytechnique de Montréal]. PolyPublie. https://publications.polymtl.ca/1165/

UNIVERSITÉ DE MONTRÉAL

INNOVATIVE MILLIMETER-WAVE COMPONENTS BASED ON MIXED SUBSTRATE INTEGRATED DIELECTRIC-METALLIC WAVEGUIDES

JAWAD ARIF AL ATTARI

DÉPARTEMENT DE GÉNIE ÉLECTRIQUE

ÉCOLE POLYTECHNIQUE DE MONTRÉAL

THÈSE PRÉSENTÉE EN VUE DE L'OBTENTION

DU DIPLÔME DE PHILOSOPHIAE DOCTOR

(GÉNIE ÉLECTRIQUE)

JUIN 2013

UNIVERSITÉ DE MONTRÉAL

ÉCOLE POLYTECHNIQUE DE MONTRÉAL

Cette thèse intitulée:

INNOVATIVE MILLIMETER-WAVE COMPONENTS BASED ON MIXED SUBSTRATE INTEGRATED DIELECTRIC-METALLIC WAVEGUIDES

présentée par : AL ATTARI Jawad Arif

en vue de l'obtention du diplôme de : Philosophiæ Doctor

a été dûment acceptée par le jury d'examen constitué de :

M. KASHYAP Raman, Ph.D., président

M. WU Ke, Ph.D., membre et directeur de recherche

M. TATU Serioja, Ph.D., membre

M. KISHK Ahmed, Ph.D., membre externe

DEDICATION

To my family.

ACKNOWLEDGEMENTS

The author is indebted to many people without whom this report would not have seen light.

First of all, I would like to express my gratitude to my PhD advisors, Prof. Ke Wu, who offered unconditional support and motivation. His creativity, perseverance and reassurance thrust me to attain the furthest of frontiers possible in academic research.

I would also like to thank all the personnel at the Poly-Grames Research Center, in particular Mr. Jules Gauthier, Mr. Traian Anretsu, Mr. Steve Dubé and Mr. Maxim Thibault, whose technical assistance was essential for the realization of the prototypes. Special thanks are extended to Mrs. Ginette Desparois and Mrs. Nathalie Lévesque for guiding me through the administrative procedure and to Mr. Jean-Sébastien Décarie for assistance with IT-related issues.

I am also grateful to Dr. Tarek Djerafi and other colleagues, especially Dr. David Dousset and Dr. Simon Hermour, for all the intellectual and technical advice and insight.

A special thank goes to the members of the examination jury, for the time they invested in reading this thesis and the invaluable comment they provided.

Last but not least, I am truly indebted to my parents who invested all their passion, time and resources to raise me to this level of academia. I also thank my relatives for their sincere moral support.

RÉSUMÉ

En recherche, un défi majeur pour l'onde millimétrique et les bandes Terahertz (THz) sont l'intégration des différents composants d'une manière compacte, efficace et à faible coût. La notion de circuits intégrés aux substrats (CIS) muni d'une variante de tradition pour une essentiel conception en simplifiant l'intégration du guide d'ondes rectangulaire (donc le GIS) avec d'autres lignes de transmission planaires telles que les lignes microbande et CPW. Bien que cette amélioré considérable conçue aux bandes de fréquences K et X, des limitations persistent dans des bandes plus élevées, en particulier la bande W. Nouvelles implémentations du concept de CIS en utilisant des guides d'ondes diélectriques, tels que le guide d'onde diélectrique non rayonnant (guide NRD), ont ainsi été proposées et avec un certain nombre de circuits à base de guide d'onde diélectrique non rayonnant intégrés aux substrats (SINRD) ont été conçus à des fréquences W-bande. Néanmoins, les critères de conception des guides rigides SINRD sont limités par leurs utilisations pratiques.

Dans cette thèse, une version modifiée du guide SINRD, basée sur le guide image NRD (iNRD), est proposé. Ce travail sera le premier à étudier la faisabilité de la conception du guide iNRD avec le concept du CIS. La polyvalence du guide image SINRD résultant (iSINRD) sera démontrée par la conception d'un certain nombre de composants passifs qui fonctionnent à la fréquence centrale 94 GHz à la bande W.

Plus précisément, les contributions suivantes ont été étudiées aux deux fréquences 88 GHz et 94 GHz:

1. Une méthodologie de conception pour l'optimisation des circuits du classe NRD. À date, Cette méthode est l'alternative le plus simple et la méthode la plus informative.
2. Un certain nombre de lignes de transmission pour guidage iSINRD qui sont conçus avec des différents profils de perforation et avec un nombre différent de lacunes sur la paroi métallique de l'image vertical.
3. Des Guides iSINRD à angles aigus à large bande et à bande étroite.
4. Deux configurations différentes de coupleurs directionnels pour le guide iSINRD qui prennent en charge le mode double (LSM_{10} et TE_{20} modes) et le fonctionnement bi-bande

(Couplage de 0-dB tandis que l'autre avec 3-dB de couplage). La bande de la matière à l'accouplement 0-dB est exclusive pour une des configurations. Ainsi, un total de six coupleurs directionnels est présenté.

5. Une structure croisée qui utilise la nature bi-bande selon l'une des configurations pour coupleur directionnel iSINRD est conçu. Dans cette structure, la LSM_{10} et les modes TE_{20} qui sont simultanément alimentés aux deux ports d'entrée sont collectées au niveau des ports opposés par l'intermédiaire du mécanisme de couplage 0-dB.
6. Hybride d'iSINRD 180° fonctionnant en mode LSM_{10}.
7. Coupler Asymmetric d'iSINRD et SIW en modes LSM_{10} et TE_{01}
8. Orthogonal Mode Transducer compact et simple (OMT ou duplexeur de polarisation), avec les modes orthogonaux ayant les modes LSM_{10} et TE_{20}.
9. Technique du mode correspondant est utilisé pour construire un coupleur en croix très compact iSINRD.
10. Un iSINRD Té magique circuit est développé en modifiant les longueurs de l'un des bras du coupleur croix iSINRD.
11. Mettre en évidence les avantages de la HFSS Eigen-mode solveur.

ABSTRACT

A major challenge facing the millimetre-wave and terahertz (THz) research fields, is the integration of different components in a compact, efficient and low-cost fashion. The concept of substrate integrated circuits (SICs) provides a vital alternative to traditional design by simplifying the integration of the rectangular waveguide (thus the SIW) with other planar transmission lines such as microstrip and CPW lines. While this has substantially enhanced the design techniques at the X- and K-band frequencies, limitations still persist at higher bands, especially the W-band and beyond. New implementations of the SICs concept using dielectric waveguides such as the substrate integrated non-radiative dielectric (SINRD) guide, were thus proposed and a number of SINRD-based circuits were designed at the W-band frequencies. Nonetheless, the SINRD guide has rigid design criteria that limit its practical use.

In this thesis, a modified version of the SINRD guide, based on the image NRD (iNRD) guide, is investigated. This work will be the first to investigate the feasibility of designing the iNRD guide with the SICs concept. The versatility of the resulting image SINRD (iSINRD) guide will be demonstrated by designing a number of passive components that operate at the W-band centre frequency of 94 GHz.

Specifically, the following contributions have been made at the W band frequencies of 88 GHz and 94 GHz:

1. An optimised design methodology of the NRD-class circuits. This method is a simpler alternative to earlier methods and is more informative.
2. A number of iSINRD guide transmission lines that are designed with different perforation profiles and with a different number of gaps in the metal wall.
3. Broadband and narrowband iSINRD guide sharp corners
4. Two different configurations of iSINRD guide directional couplers that support dual mode (LSM_{10} and TE_{20} modes) and dual band operation (one band for 0-dB coupling while the other for 3-dB coupling). The band pertinent to the 0-dB coupling is exclusive for one of the configurations. Thus, a total of six directional couplers are presented.

5. A cross-over structure that utilizes the dual band nature of one of the iSINRD directional coupler configurations is designed. In this structure, the LSM_{10} and TE_{20} modes that are concurrently fed at the two input ports are collected at the opposite ports through the mechanism of 0-dB coupling.
6. A 180^{o} iSINRD hybrid based on the LSM_{10} mode
7. An asymmetric iSINRD-SIW coupler based on the LSM_{10} and TE_{01} modes
8. A compact and simple orthogonal mode transducer (OMT), with the orthogonal modes being the LSM_{10} and the TE_{20} modes
9. Even-odd mode analysis technique is used to construct a very compact iSINRD cruciform coupler.
10. An iSINRD magic-T circuits is developed by modifying the lengths of one of the arms of the iSINRD cruciform coupler.
11. Highlighting the advantages of the HFSS Eigen-mode solver.

TABLE OF CONTENTS

LIST OF TABLES

LIST OF FIGURES

LIST OF SYMBOLS AND ABBREVIATIONS

ε_1	Dielectric Constant of the Central Channel
ε_2	Effective Permittivity of the Side Regions
α	Attenuation Constant
β	Propagation Constant
λg	Wavelength inside the Waveguide
ALMA	Atacama Large Millimeter-wave Array
C	Calculated
CBCPW	Conductor-Backed Co-Planar Waveguide.
CPW	Coplanar Waveguide
E-band	Frequencies in the range of 40 GHz to 65 GHz
E-field	Electric Field
EM	Electromagnetic
f_c	Cut-off Frequency
f_g	Center Frequency
FHMSIW	Folded Half Mode Substrate Integrated Waveguide
f_n	Minimum Operating Frequency
FSIW	Folded Substrate Integrated Waveguide
f_x	Maximum Operating Frequency
H-field	Magnetic Field
HFSS	High Frequency Structure Simulator
HMSIW	Half Mode Substrate Integrated Waveguide
IG	Image Guide
iNRD	Image Non-Radiative Dielectric Guide

iSINRD	Image Substrate Integrated *Non-Radiative* Dielectric Waveguide
iSIW	Inverted Substrate Integrated Waveguide
K-band	Frequencies in the range of 40 GHz to 65 GHz
LSM	Longitudinal Section Magnetic
LSE	Longitudinal Section Electric
LTCC	Low Temperature Co-fired Ceramic
M	Measured
MATLAB	Matrix Laboratory
MHMIC	Miniature Hybrid Microwave Integrated Circuits
MOF	Maximum Operating Frequency
NRD	Non-Radiative Dielectric Guide
OMT	Ortho-mode Transducer
PEC	Perfect Electric Condition
PCB	Printed Circuit Board
PMC	Perfect Magnetic Condition
PML	Perfectly Matched Layer
RF	Radio Frequency
S	Simulated
SIC	Substrate Integrated Circuits
SINRD	Substrate Integrated Non-Radiative Dielectric Guide
SIIG	Substrate Integrated Image Guide
SIW	Substrate Integrated Waveguide
tanδ	Loss Tangent
TE	Transverse Electric

TM	Transverse Magnetic
V band	Frequencies in the range of 40 GHz to 65 GHz
VNA	Vector Network Analyzer
W band	Frequencies in the range of 65 GHz to 110 GHz
WR10	Rectangular Waveguide operating in the W-band
X-band	Frequencies in the range of 40 GHz to 65 GHz

LIST OF ANNEXES

INTRODUCTION

Economic, compact, light, multifunctional and broadband, are but a few golden words that has been defining the evolution trend of telecommunication systems in recent decades. Coupled with the fact that technology in general is becoming increasingly ubiquitous and more readily available worldwide, meant that satisfying the aforementioned development trends ought to be on a large-scale, reproducible and reliable. In addition, access to higher frequency bands has proved to be a necessary requirement in order to satisfy increasing demand for bandwidth as well as frequency constraints some scientific applications have (e.g. the Atacama Large Millimeter-wave Array (ALMA) millimeter-wave astrophysics project [1]). To that end, classical system design approach requires a radical overhaul that continues to this very date, and this overhaul affects all stages of systems design, especially that pertaining to the design of RF circuitry.

The advent of WWII marked the real birthdate of RF and microwave communications systems. At that time, the state-of-the-art was circuits based mostly on the rectangular metal waveguide [2], [3]. While it is still vital for some contemporary applications such as conservative aerospace industry, it alone could not have accounted for the exponential technological growth of recent decades, as it fails to satisfy most of the trendy requirements mentioned above, especially low-cost, integration and compactness [4]. This has inspired researchers to develop more practical alternatives, such as the microstrip and the coplanar waveguide (CPW), which have proliferated the innovative circuits developed at the X band and other microwave ranges. At higher frequency bands, however, their loss performance degrades significantly, which has prompted the development of dielectric-based waveguides, such as the image [5] and the NRD-class guides [6–8]. All the above waveguides, however, share the same major challenge – seamless integration within the RF system as a whole in a manner that is amicable to mass production.

A new door to innovation was thus opened, with the substrate integrated circuits (SICs) design technology [9–11] taking center stage in the paradigm of RF circuits, thanks to its satisfaction of most, if not all, the modern trendy requirements. In the initial stages, the SICs technology facilitated seamless planar integration of the rectangular waveguide (thus called the substrate integrated waveguide or SIW) with other waveguide technologies [12–16]. Furthermore, it is scalable and flexible, as it supports single as well as multi-layer designs and can be realized with

different fabrication techniques such as PCB, MHMIC and LTCC. Consequently, the application portfolio of the EM spectrum witnessed an unprecedented growth, with the conception of a myriad of innovative K-band, and a couple of V- and E-band, SIW-based circuits (HMSIW, FSIW, FHMSIW, etc.) [17–27].

The design of SIW circuits, however, faces many limitations at bands higher than the Ka band. This is mainly because of the guide dimensions that approach fabrication tolerance with increasing frequencies; a characteristic problem of the rectangular waveguide [28]. In addition, the SIW does not support any *TM* mode, and it is limited predominantly to the TE_{10} mode. While this could be an advantage, in the sense that mode conversion and interference is reduced, it nonetheless limits the full potential of the original rectangular waveguide for multi-mode applications. As a result, the scope of the SICs technology had to be expanded to include the image guide (IG) and the NRD guide. Generally speaking, the losses associated with dielectric guides could be much lower than the SIW counterparts, because less metal is involved. Furthermore, the dimensions of these guides are relatively above the fabrication tolerance, even at the W-band frequencies and beyond [28]. Therefore, the incorporation of these guides has proved to be a worthwhile initiative, as a number of novel V-band and W-band circuits based on the substrate integrated IG (SIIG) [28] and the substrate integrated NRD (SINRD) [29], [30] guides were recently reported. Unlike the SIW, the SINRD guide supports both the *TM* and *TE* (better known as *LSM* and *LSE* in the NRD literature) modes of the original NRD guide, and thus has deeper research potential. The SIW, SIIG and the SINRD guides are illustrated in Figure 1.

The NRD guide offers additional advantages over the IG; namely the electric symmetry of its dominant LSM_{10} mode and the orthogonality of LSM_{10} to the TE_{10} mode of the rectangular waveguide (and the NRD guide, in which it can propagate at zero cut-off). Those advantages span two additional ones, namely doubled compactness and mode "quietness". These extra advantages are better manifested in the image NRD (iNRD) guide [31–33] shown in Figure 2; the vertical metal wall facilitating size reduction as well as suppression of several modes, especially the LSE_{10} mode, which may be considered unwanted in most cases. While both advantages are of paramount significance, the latter is particularly worth mentioning because LSM_{10}-LSE_{10} mode conversion is inevitable in the design of NRD circuits with sharp corners [34–38], which limits the design of NRD circuits; unless otherwise required [39].

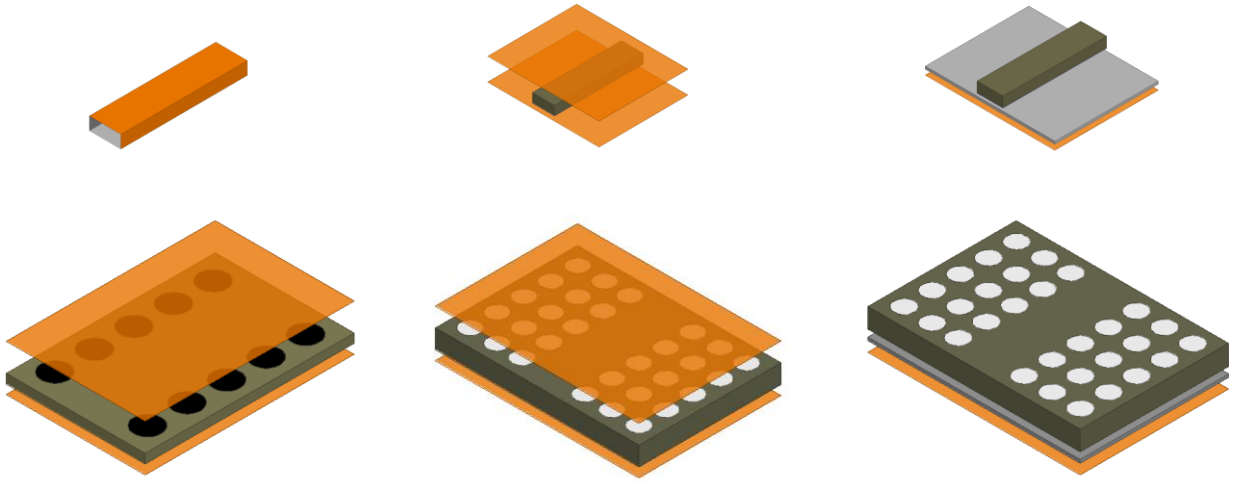

Figure 1 : Upper segment: exploded views of the rectangular waveguide (left), the NRD guide (centre) and the image guide (right). Lower segment: exploded views of the SIW (left), the SINRD guide (centre) and the SIIG (right). Orange: metal covers, black: metal vias, grey: insulating substrate of the SIIG, white: air vias, dark green: dielectric substrate which contains the waveguide.

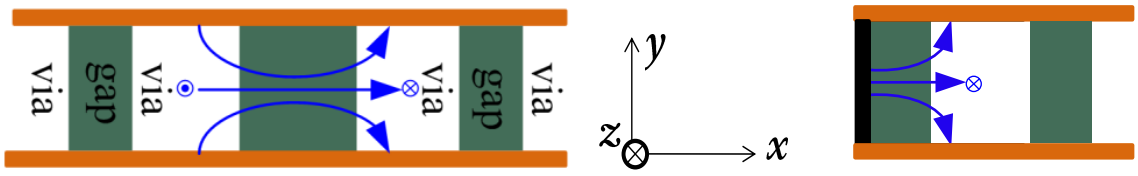

Figure 2 : Cross-sectional front view of the E-field lines of the LSM_{10} mode in the SINRD guide (left) and the image SINRD (iSINRD) guide (right).

In spite of the many advantages of the NRD and iNRD guides, they are not fully exploited in the literature. Furthermore, the iNRD guide is yet to be incorporated in the SICs design paradigm. It is thus envisioned that developing a substrate integrated iNRD (iSINRD) shall yield a multitude of innovative circuits with manifold advantages, especially at the W-band frequencies. This indeed is the objective of this thesis, with chapter 1 shedding more light on the proposed iSINRD and introducing a concise design scheme for the NRD-class waveguides, which is validated by practical implementations of iSINRD transmission lines in Chapter 2. Chapter 3 then highlights the aforementioned advantages of the iSINRD guide by implementing it in a number

of single-mode, multi-mode and dual-band directional coupler circuits.. The suppression of the LSE_{10} mode at sharp bends is highlighted in Chapter 4, which details the implementation of the iSINRD guide in the design of four-port junctions such as cruciform couplers, cruciform magic-T, and ortho-mode transducer circuit circuits. The discussion then wraps up with concluding remarks and a future outlook.

Chapter 1 INVESTIGATION OF THE IMAGE SINRD GUIDE AT THE W-BAND FREQUENCIES

1.1 Introduction

In the build-up to the implementation of the iNRD guide with the SICs technique, a theoretical discussion pertaining to the guide geometry and operating modes, alternative design methodology and procedure for selecting the guide parameters, as well as propagation and attenuation in the iSINRD guides, is carried out in the following sections. The alternative methodology discussed here is flexible in that it can be used for any perforation profile, although the discussion here focuses on the circular and square perforation profiles. It follows that a maximum of only two graphs is needed to design the iSINRD guide, although it involves *at least* triple the number of parameters of the original NRD guide; and if the substrate of effective permittivity is used instead of perforation, then only one graph is required.

1.2 Review of the NRD and SINRD Waveguides

1.2.1 Geometry of the NRD and SINRD Guides

The NRD waveguide, shown in Figure 1-1 (top, left), was first proposed in [6] as a low-loss waveguide that addressed the radiation-at-bends-and-discontinuities, which has been a well-known shortcoming of its H-guide predecessor [7], [8]; thus the name "non-radiative". This is simply achieved by ensuring that the operating frequency is lower than f_x; the cut-off frequency of the 1st parallel-plate mode in the air side-regions ($f_g < f_x$; $f_x = c/2a$) [6]. So below f_x, leakage into the side regions due to bends and discontinuities is suppressed or contained [6]. Designing the NRD guide with the SICs technique yields the substrate integrated NRD (SINRD) guide [29], [30], which differs from the NRD guide by the fact that the side regions that flank the guiding channel are made of a lower permittivity dielectric (other than air). It naturally inherits all the features of the NRD guide, in addition to the SICs advantage of seamless integration with other planar circuitry. This dielectric contrast between the two regions can be done by perforating the substrate, less the NRD channel width, as per Figure 1-1 (top, right). In the rest of this work, the

lateral height and width of the guide are denoted by *a* and *b*, respectively; as shown in Figure 1-1 (bottom). Perforation is sometimes done with uniformly distributed non-metalized circular holes, but may not be limited to that, as shown in Figure 1-2. Obviously, there exist an infinite number of perforation profiles. The choice of a perforation profile depends on many factors such as the profile's geometrical complexity, perforation impact on substrate's fragility, practical feasibility with available fabrication tools, etc. The perforated regions have a lower effective permittivity compared to the ε_1 of the middle channel. Perforation thus introduces more design variables, and their number depends on the perforation techniques. For example, if perforation is done with circular via holes, then three new parameters are introduced: via diameter (*D*), the via-to-via spacing (*gap*) and the effective permittivity (ε_{r2}) of the perforated regions. The variable ε_2, anyhow, is always present in any SINRD guide design as it is a natural consequence of substrate perforation (regardless of the perforation technique). It is necessary for the calculation of $f_x = c/\left(2a\sqrt{\varepsilon_2}\right)$ of the 1st parallel-plate mode in the perforated regions and β of the SINRD guide (see section 1.4.7). Sometimes, f_x is called the maximum operating frequency (*MOF*) [29], [30], because at f_x, leakage into the side regions due to bends or discontinuities occurs. Hence, f_x designates the maximum frequency at which the SINRD guide can be operated; thus the name *MOF*. In the rest of this work, f_x is used to designate the *MOF* limit. It is essential to determine the f_x limit in order to design the SINRD for optimum performance. Note that the f_x limit is pertinent to the LSM_{10} mode discussed in the next subsection.

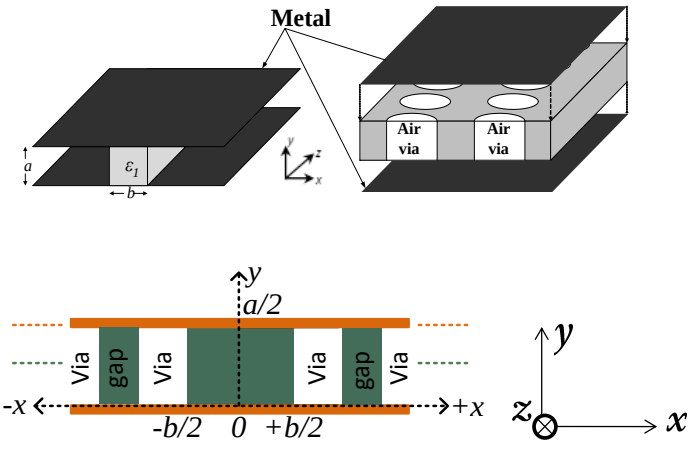

Figure 1-1: The NRD guide (top, left) and the SINRD guide (top, right). Bottom: Cross-sectional front view of the SINRD guide.

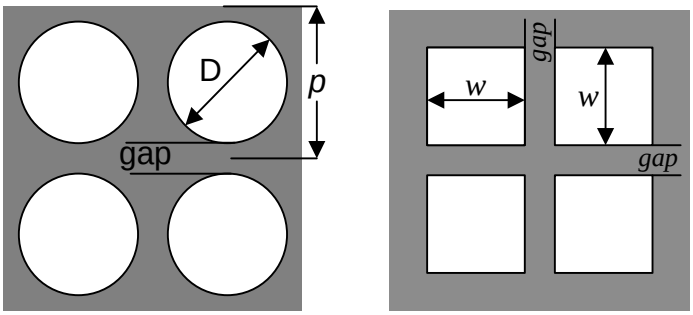

Figure 1-2: Perforation Profiles (top view): circular profile (left), and square (right) perforation profiles; to name a few.

1.2.2 Dominant Modes

Another distinguishing feature of the NRD/SINRD guide is its multi-mode nature, as it supports four classes of hybrid symmetric and anti-symmetric TM^{x}_{mn} (H_x = 0) and TE^{x}_{mn} (E_x = 0) modes. In this thesis, the mode nomenclature used in [6] is adopted, without loss of generality. It then follows that the dominant or fundamental modes of the NRD/SINRD guide are the symmetric TM^{x}_{10}(or LSM_{10}), the symmetric TE^{x}_{00} (or TE_{10} in rectangular waveguide) and the symmetric TE^{x}_{10} (or LSE_{10}) modes. This mode richness expands the scope of the SICs design paradigm to encompass more diverse applications such as the dual-polarized planar antenna arrays reported in [40], [41], and the H-guide antenna reported in [42], which operates with the TE^{x}_{00} mode. Cross-sectional front views of the three modes are shown in Figure 1-3. For other mode profiles, the interested reader is referred to [43], [44] and [45].

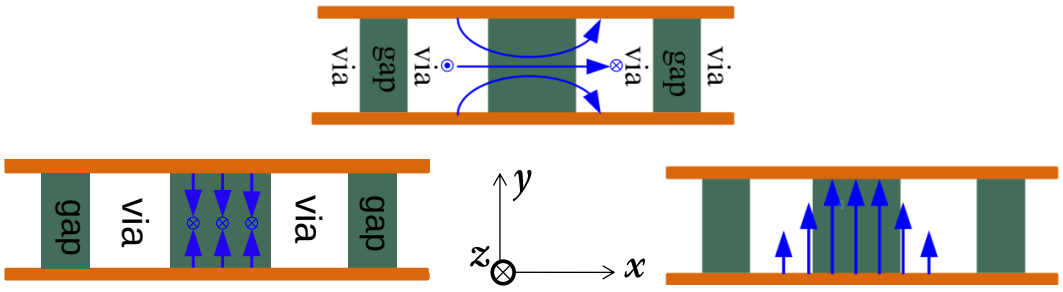

Figure 1-3: Cross-sectional front view of the E-field lines of the LSM_{10} (top), TE_{10} (bottom. right) and LSE_{10} (bottom, left) modes in the (SI)NRD guide. Encircled × (into page) or · (out of page) represent the longitudinal E_z component.

The field equations for each mode are given by the equations below, where regions 1 and 2 refer to the central guiding channel and the perforated side regions, respectively [43]. It can be deduced from those equations that the three dominant modes are mutually quasi-orthogonal [39], [46]. Furthermore, it is important to note the E-field of the LSM_{10} mode has all three components, and that the E_z component is maximum at the interface between guiding channel and the perforation region ($x = b/2$), and null at the centre ($x = 0$). This is property of the E_z component is fundamental to the design of many circuits in the subsequent chapters. The general field equations of symmetric and asymmetric TM_{mn}^{x} and TE_{mn}^{x} modes are given in Annex 1. In the remaining discussion, the three modes presented in this sub-section are referred to as LSM_{10}, LSE_{10}, and TE_{10}, respectively.

Symmetric TM_{10}^{x} (or LSM_{10}) Mode

$Region\ 1,\ \varepsilon_{r1}\ (x\ <|b/2|)$

.
$$E_x = (A/\varepsilon_r)p^2 \sin(\pi y/a)\cos(\beta_x x) \quad (1.1\text{ a})$$

$$E_y = -A(\beta_x/\varepsilon_r)(\pi/a)\cos(\pi y/a)\sin(\beta_x x) \quad (1.1\text{ b})$$

$$E_z = j(A/\varepsilon_r)\beta\beta_x \sin(\pi y/a)\sin(\beta_x x) \quad (1.1\text{ c})$$

$$H_x = 0 \quad (1.1\text{ d})$$

$$H_y = -A\omega\varepsilon_0\beta \sin(\pi y/a)\cos(\beta_x x) \quad (1.1\text{ e})$$

$$H_z = jA\omega\varepsilon_0(\pi/a)\cos(\pi y/a)\cos(\beta_x x) \quad (1.1\text{ f})$$

$Region\ 2,\ \varepsilon_{r2}\ (x\ >|\ b/2\ |)$

.
$$E_x = Ap^2 \sin(\pi y/a)\cos(\beta_x\, b/2)e^{\varphi(b/2-|x|)} \quad (1.1\text{ g})$$

$$E_y = \mp A\varphi(\pi/a)\cos(\pi y/a)\cos(\beta_x\, b/2)e^{\varphi(b/2-|x|)} \quad (1.1\text{ h})$$

$$E_z = \pm jA\beta\varphi \sin(\pi y/a)\cos(\beta_x\, b/2)e^{\varphi(b/2-|x|)} \quad (1.1\text{ i})$$

$$H_x = 0 \quad (1.1\text{ j})$$

$$H_y = -A\omega\varepsilon_0\beta\sin(\pi y/a)\cos(\beta_x\, b/2)e^{\varphi(b/2-|x|)} \quad (1.1\text{ k})$$

$$H_z = jA\omega\varepsilon_0(\pi/a)\cos(\pi y/a)\cos(\beta_x\, b/2)e^{\varphi(b/2-|x|)} \quad (1.1\text{ l})$$

Symmetric TE_{10}^{x}(or LSE_{10}) Mode

$Region\ 1,\ \varepsilon_{r1}\ (x\ <|b/2|)$

. $E_x = 0$ (1.2 a)

$E_y = C\omega\mu_0\beta\cos(\pi y/a)\cos(\beta_x x)$ (1.2 b)

$E_z = jC\omega\mu_0(\pi y/a)\sin(\pi y/a)\cos(\beta_x x)$ (1.2 c)

$H_x = Cp^2\cos(\pi y/a)\cos(\beta_x x)$ (1.2 d)

$H_y = C\beta_y(\pi y/a)\sin(\pi y/a)\sin(\beta_x x)$ (1.2 e)

$H_z = jC\beta\beta_x\cos(\pi y/a)\sin(\beta_x x)$ (1.2 f)

$Region\ 2,\ \varepsilon_{r2}\ (x\ >|\ b/2\ |)$

. $E_x = 0$ (1.2 g)

$E_y = C\omega\mu_0\beta\cos(\pi y/a)\cos(\beta_x\ b/2)\ e^{\varphi(b/2-|x|)}$ (1.2 h)

$E_z = jC\omega\mu_0(\pi y/a)\sin(\pi y/a)\cos(\beta_x\ b/2)\ e^{\varphi(b/2-|x|)}$ (1.2 i)

$H_x = Cp^2\cos(\pi y/a)\cos(\beta_x\ b/2)e^{\varphi(b/2-|x|)}$ (1.2 j)

$H_y = \pm C\varphi(\pi y/a)\sin(\pi y/a)\cos(\beta_x\ b/2)\ e^{\varphi(b/2-|x|)}$ (1.2 k)

$H_z = \pm jC\beta\varphi\cos(\pi y/a)\cos(\beta_x\ b/2)\ e^{\varphi(b/2-|x|)}$ (1.2 l)

Symmetric TE_{00}^{x}(or TE_{10}) Mode

$Region\ 1,\ \varepsilon_{r1}\ (x\ <|b/2|)$

. $E_x = 0$ (1.3 a)

$E_y = C\omega\mu_0\beta\cos(\beta_x x)$ (1.3 b)

$E_z = 0$ (1.3 c)

$H_x = Cp^2\cos(\beta_x x)$ (1.3 d)

$H_y = 0$ (1.3 e)

$$H_z = jC\beta\beta_x \sin(\beta_x x) \quad (1.3\text{ f})$$

$Region\ 2,\ \varepsilon_{r2}\ (x\ > |\ b/2\ |)$

. $$E_x = 0 \quad (1.3\text{ g})$$

$$E_y = C\omega\mu_0\beta \cos(\beta_x\, b/2)\, e^{\varphi(b/2-|x|)} \quad (1.3\text{ h})$$

$$E_z = 0 \quad (1.3\text{ i})$$

$$H_x = Cp^2 \cos(\beta_x\, b/2) e^{\varphi(b/2-|x|)} \quad (1.3\text{ j})$$

$$H_y = 0 \quad (1.3\text{ k})$$

$$H_z = \pm jC\beta\varphi \cos(\beta_x\, b/2)\, e^{\varphi(b/2-|x|)} \quad (1.3\text{ l})$$

In all of the above equations, *p* and *q* are related by the following relationship:

$$p^2 = \beta^2 + (m\pi/a)^2 = {k_0}^2\varepsilon_1 - {\beta_x}^2 = {k_0}^2\varepsilon_2 + \varphi^2 \quad (1.4)$$

where β is the propagation constant in the waveguide, *m* is the order of the mode (1 for the LSM_{10} and LSE_{10} modes; 0 for the TE_{10}), ε_1 is the permittivity of the substrate, ε_2 is the effective permittivity of the perforated regions, β_x is the transverse propagation constant in the dielectric, and φ is the attenuation constant in the perforated region. While the cut-off frequency of the TE_{10} mode is zero [43], that of the LSM_{10} mode can be deduced from equation 1.5, by matching the *E* components at the air-dielectric interface. Cut-off of the LSE_{10}, and other, modes is give in [43].

LSM_{10} mode:

$$\beta^2 = k_0^2 - (\pi/a)^2 - \beta_x^2 \quad (1.5\text{ a})$$

$$\beta_x \tan(\beta_x\, b/2) = (\varepsilon_{r1}/\varepsilon_{r2})\varphi \quad (1.5\text{ b})$$

$$\varphi^2 = k_0^2(\varepsilon_{r1} - \varepsilon_{r2}) - \beta_x^2 \quad (1.5\text{ c})$$

1.3 Design Challenges of the SINRD Guide

Although perforation simplifies the physical fabrication of the SINRD guide, it nonetheless limits the application scope of the SINRD guide since the perforated regions are strictly reserved for the air vias, and increase the total width of the guide to more than twice that of the guiding channel (width b). Furthermore, it complicates its theoretical design since any perforation profile will entail additional design parameters that must be accurately identified for operation at a desired f_g; a problem that is not treated in-depth in the SINRD literature.

The design method of SINRD guide circuits is not so straightforward. This is attributed to the lack of an accurate justification of the optimum dimensions for a desired frequency of operation, henceforth called f_g. Specifically, the f_x limit is insufficient for precisely determining the thickness a (and thus width b) of the guide. For the SINRD and iSINRD guides, the situation is further complicated because of the additional perforation variables that are difficult to inter-relate with the lateral dimensions. It is thus imperative to accurately determine all those parameters in order to obtain a correct operation at the desired operating frequency, f_g, and operating mode. Some effort has been made at relating those many variables [47], but they are incomplete and rather vague, with insufficient explanation of how the lateral dimensions (a and b), and the perforation geometry should be selected. Furthermore, the analysis in [47] is limited to a few variations of the circular perforation profile, and does not consider the general case. Also, the existing relations for calculating ε_2 [30] do not take into account the variations of ε_2 with frequency reported by [48], [49].

In the next section, the first problem is mitigated by implementing a metal image plane at the center of the guide which reduces the total size by 50%, and does away with one of the perforated regions. For the second problem, a new (missing) design limit that should supplements the f_x limit is introduced, and will substantially improve the way in which the dimensions of SINRD circuits are chosen. Then, a concise and clear method for determining all pertinent dimensions is presented. As will be shown, this approach is versatile in the sense that it is applicable to any perforation profile. Only a couple of extra steps are required for the SINRD guide. For the iSINRD guide, one further "step" is required, which is simply halving the value of width b! Prior to that, a fast, accurate and novel analysis approach is proposed that substantially simplifies the analysis and accurately characterizes the SINRD guide.

1.4 Proposed Alternative Design Approach of the SINRD Guide

1.4.1 The Image SINRD (iSINRD) Guide

The mode diversity discussed above can equally be a nuisance for some applications as mode conversion may take place, especially between the LSE_{10} and LSM_{10} modes and also along waveguide bends, as mentioned above. Mode suppressors would then be needed to suppress one of the two modes [47], [50].

Looking at the H-field of the LSM_{10} mode in Figure 1-3, it has a vertical electric symmetry. Based on the image theory, bisecting the NRD guide with a vertical longitudinal metal wall yields the image NRD (iNRD) guide [31–33], which supports the propagation of the LSM_{10} mode; as shown in Figure 1-4. Conversely, the LSE_{10} and the TE_{10} modes are suppressed. In fact, all symmetric TE^{x}_{mn} modes are consequently suppressed [31]. This situation is advantageous for applications that rely solely on the LSM_{10} mode, and/or waveguide bends, since LSE_{10}-LSM_{10} mode conversion can safely be ignored. The iNRD guide is thus a very simple LSE_{10} mode suppressor.

Other than the LSM_{10}, the iNRD guide also supports the asymmetric TE^{x}_{01} (TE_{20} in rectangular waveguide) mode, which is shown in Figure 1-4. This fact is utilized to design a set of multimode planar circuits; as shall be shown in Chapter 3. Similar to the LSM_{10} mode, the TE^{x}_{01} mode is hitherto called the TE_{20} mode.

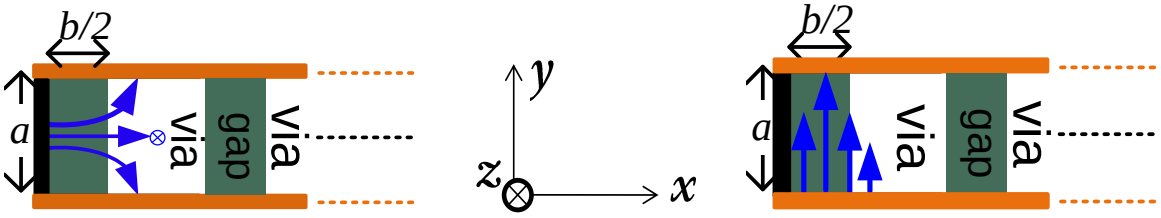

Figure 1-4: The cross-sectional front view of the E-field lines of the LSM_{10} (left) and TE_{20} (right) modes in the iSINRD guide.

The field equations for the TE_{20} mode are given by:

Asymmetric TE_{01}^{x}(or TE_{20}) Mode

$Region\ 1,\ \varepsilon_{r1}\ (x\ <|b/2|)$

. $E_x = 0$ (1.6 a)

$E_y = D\omega\mu_0\beta \sin(\beta_x x)$ (1.6 b)

$E_z = 0$ (1.6 c)

$H_x = Dp^2 \sin(\beta_x x)$ (1.6 d)

$H_y = 0$ (1.6 e)

$H_z = -jD\beta\beta_x \sin(\beta_x x)$ (1.6 f)

$Region\ 2,\ \varepsilon_{r2}\ (x\ >|\ b/2\ |)$

. $E_x = 0$ (1.6 g)

$E_y = \pm D\omega\mu_0\beta \sin(\beta_x\ b/2)\ e^{\varphi(b/2-|x|)}$ (1.6 h)

$E_z = 0$ (1.6 i)

$H_x = \pm Dp^2 \sin(\beta_x\ b/2) e^{\varphi(b/2-|x|)}$ (1.6 j)

$H_y = 0$ (1.6 k)

$H_z = jD\beta\varphi \sin(\beta_x\ b/2)\ e^{\varphi(b/2-|x|)}$ (1.6 l)

The cut-off of the TE_{20} mode is obtained by matching the H_z components at the air-dielectric interface. Re-arranging equation 1.6 and setting $m = 0$, yields the following conditions:

TE_{20} mode:

$\beta^2 = k_0^2 - \beta_x^2$ (1.7 a)

$\beta_x \cot(\beta_x\ b/2) = -\varphi$ (1.7 b)

$\varphi^2 = k_0^2(\varepsilon_r - \varepsilon_{r2}) - \beta_x^2$ (1.7 c)

Besides the mode suppression, the iSINRD guide offers an additional advantage over the SINRD guide; namely size compactness, since the iSINRD guide is half the size of the SINRD guide. The iSINRD guide is thus an optimum choice between the SINRD guide and the SIW. Nonetheless, it is yet to be reported in the SINRD literature. Thus, the objective of this thesis is to exploit the rich potential of the iNRD guide in the SICs paradigm; i.e. the iSINRD guide. Prior to that, however, an optimisation of the design approach of the SINRD circuits is worthwhile, which is detailed in the next section. Unless otherwise stated, it must be emphasized that the following discussion focuses on the LSM_{10} mode, since the iSINRD guide is the cornerstone of this thesis.

1.4.2 Eigen-Mode Analysis of Periodic SINRD Guides

Full-wave analysis of periodic general NRD-class guides, such as the SINRD guide, is expensive in terms of computational time and resources. This fact is manifested when computing the cut-off frequency and the propagation curve of the LSM_{10} mode, especially when the side regions are not air and the effective permittivity is unknown a priori. Alternatively, the guide should be analysed with a 3D Eigen-mode technique that is available in well-known microwave solvers such as [51], [52]. Floquet's theorem [44] is the underlying principle of Eigen-mode analysis for periodic structures. In brief, in a periodic structure, the electromagnetic fields at point x differ from those at point $x + p$, by only $e^{\gamma p}$ where p is the period of the structure [44]. Obviously, this requires the guide, and thus the perforation profile, to be periodic. Then, only a "unit-cell" of the guide needs to be analysed. Consequently, the computational time and resources needed for the analysis are reduced enormously. Furthermore, the values of the cut-off frequency, f_c, and the propagation constant, β, that are obtained with this technique are more accurate because the analysis is done *inside* the guide, instead of relative to the wave-port in a full-wave analysis. With this technique, many essential parameters can be extracted, such as the propagation and attenuation constants (β and α). For the iSINRD guide, only half the SINRD guide needs to be studied, as shown in Figure 1-5. To simulate the open end of the iSINRD, a perfectly matched layer (PML) boundary condition should be applied at the edge of the unit cell. By default, perfect electric conductor (PEC) is assigned to the top and bottom planes. Note that the vias are also *covered* with metal, but are not metallized from the inside. To further enhance the efficiency, the perforated region can be replaced with an equivalent ε_2-dielectric. The value of

ε_2 may not be initially known, in which case it will be determined based on the desired cut-off frequency as well as the feasibility of a corresponding perforation profile. The advantages of the Eigen mode solver are further highlighted in [101].

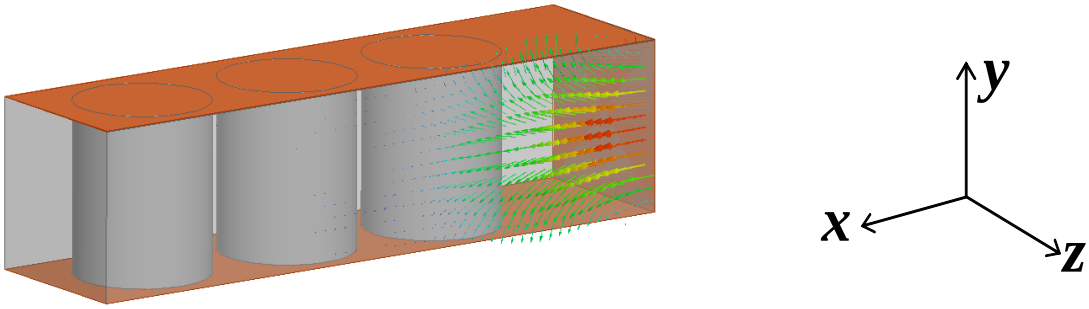

Figure 1-5: A 3-D view of a unit-cell of the iSINRD waveguide in HFSS Eigen-mode solver together with a cross-sectional front view of the simulated E-field of the LSM_{10} mode.

1.4.3 The SINRD Guide as a Generalised NRD Guide

The best way to approach the design of an SINRD guide is to visualize it as a generalized NRD waveguide with the side regions filled with an arbitrary dielectric material ($1 < \varepsilon_2 < \varepsilon_1$). This simplifies the discussion substantially. The ε_2-dielectric is an abstract representation of the perforated regions. Hence, regardless of what the perforation profile is, the designer needs only to look at the resultant ε_2; hereby reducing the design complexity to only three variables (a, b, and ε_2). Relating the ε_2 to the dimensions of the perforation profile is then left as a last step, which varies depending on the perforation profile. Figure 1-6 illustrates a cross-sectional view of this visualisation.

The choice of dielectric substrate suitable for the W-band applications is very tricky because not many materials maintain low loss tangent ($\tan\delta$) characteristics over a wide frequency range. Several studies confirm that the $\tan\delta$ of many polymer (e.g. Teflon $\varepsilon_1 = 2.06$, $\tan\delta = 0.00024$ and Polystyrene $\varepsilon_1 = 2.53$, $\tan\delta = 0.0007$) and ceramic substrates (such as Alumina $\varepsilon_1 = 9.8$, $\tan\delta = 0.00015$) up to 110 GHz is on the order of 10^{-4} [45], [53–59], which is roughly ten times less than its Rogers counterparts (e.g. RO6010) even at 10 GHz [60]. For the design of SINRD circuits, other factors should also be considered. For optimal wave guidance in the central channel,

dielectric guides in general are typically designed with a high permittivity ($\varepsilon_1 > 9$) dielectric material [61]**.** This is because waves in such waveguides are primarily surface waves, and hence a higher dielectric contrast between the dielectric and the surrounding medium correspond to better attenuation of the field in the surrounding; i.e. waves are more confined in the central dielectric [61]. Therefore, Alumina is chosen in the rest of this work. The discussion in the following subsection confirms this choice. Table 1.1 presents a comparison between a numbers of dielectric material candidates with which an iSINRD guide can be realised. For the sake of certainty, the loss tangent of Alumina was measured at our lab at 94 GHz and the measured value indeed conforms with the one cited in [59].

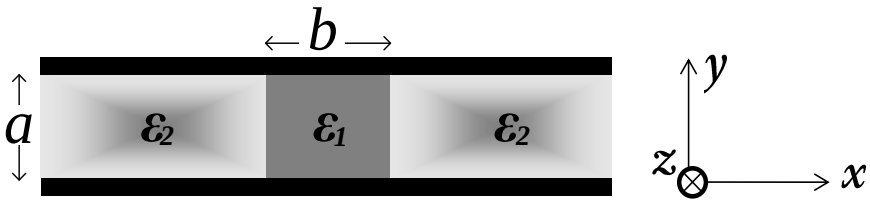

Figure 1-6: The cross-sectional front view of a generalised NRD guide.

Table 1.1: Comparison of different dielectric materials at different millimeter-wave frequencies.

Material	**Frequency (GHz)**	ε_r	**tanδ (×10^{-4})**	**Reference**
Teflon	100	2.06	2.4	[53–59]
Polyethylene	100	2.53	0.7	[53–59]
Alumina	94	9.8	1.5	[59]; measured
RO6010	10	10.2	23	[60]
Polypropylene	100	2.25	7.3	[59]

1.4.4 The Minimum Operating Frequency, f_n and the Choice of Thickness a

For any given a, b can theoretically assume any value in the abstract range [0:∞]. If b = 0, then the structure is a parallel-plate waveguide filled with a ε_2-dielectric, whose 1st mode cut-off frequency is

$$f_{c1} = c/(2a\sqrt{\varepsilon_2}) \qquad (1.8)$$

Equation 1.8 is the f_x limit discussed in Section 1.2. Since this is the maximum operating frequency of the general NRD guide, then, for $b > 0$, the structure becomes an NRD guide whose $f_g < f_x$; a rather obvious result. Now, if b is continuously increased to $b = \infty$, then the structure is again a parallel-plate waveguide, filled with a ε_1-dielectric material, whose 1st mode cut-off frequency is

$$f_{c1} = f_n = c/(2a\sqrt{\varepsilon_1}) \qquad (1.9)$$

Since f_n can only be obtained for $b = \infty$, and is independent of ε_2, then it is intuitive to conclude that operation below this frequency is impossible for $0 < b < \infty$. Hence, f_n is the "minimum operating frequency" at which the NRD guide can operate. This is the supplementary limit mentioned at the end of the previous section. Since both f_x and f_n depend on a, each value of a corresponds to a distinct set of f_x - f_n limits or operating frequency bands (f_g -bands), as shown in Figure 1-7. Thus, varying a in the range [0:∞] results in a super-band of f_g-bands. At the lower part of the spectrum, the bands strongly overlap, and the choice of a is no longer critical; i.e. the super-band saturates at lower frequencies. This scenario is reversed at the upper part of the spectrum. Hence, a should be chosen such that it corresponds to an f_g-band that covers the desired f_g.

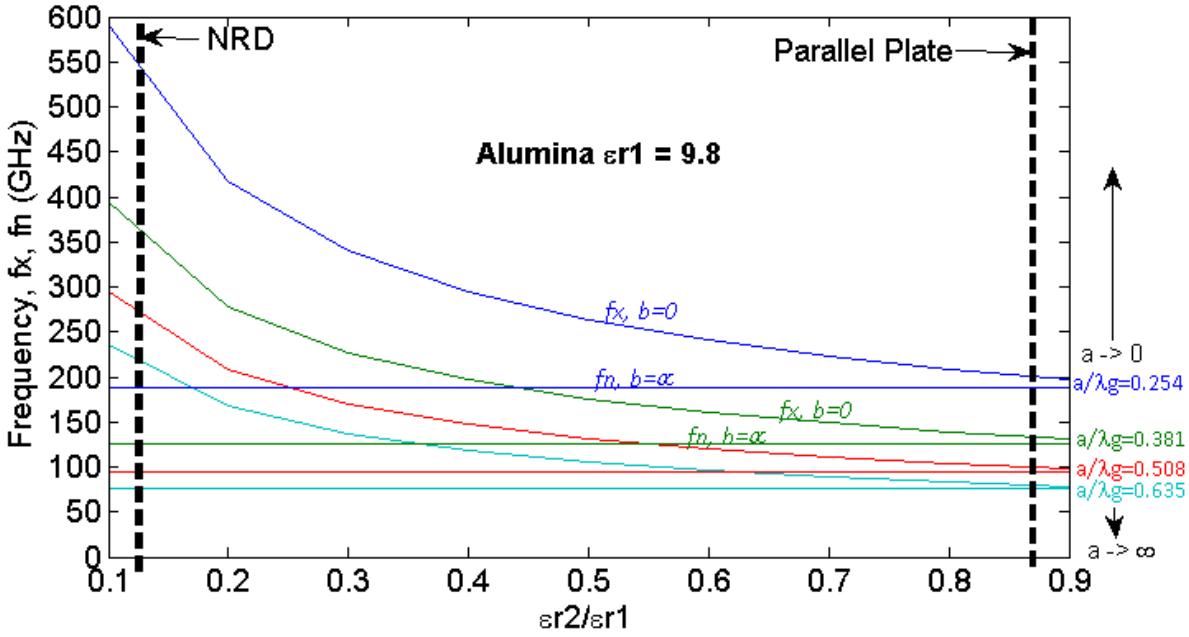

Figure 1-7: Frequency f_x-f_n bands corresponding to different thicknesses computed with [62].

1.4.5 Determining the Optimum Thickness *a*

The significance of the f_n limit is subtle yet crucial, as without the f_n limit, one can be misled into thinking that operating at any $f_g < f_x$ is possible for a given thickness. It is therefore important to supplement the f_x limit with this new f_n limit. This scenario is illustrated in Figure 1-8. Note that as ε_2 approaches ε_1, the f_x and f_n limits converge to the same single point. This point is another way of visualising a channel width b equal to infinity; except that no substrate perforation is performed.

The choice of thickness a should be such that the desired f_g is not close to either f_x or f_n, as unrealistic values of channel width b would be required (close to zero or infinity). For small increments of a (typically, Δa = 5 mil), the decision should be made based on which band corresponds to the maximum number of ε_2 values for the desired f_g. This is to ensure design flexibility and robustness. That is, a wider range of ε_2 values gives more flexibility in choosing the perforation profile. This is illustrated in Figure 1-9.

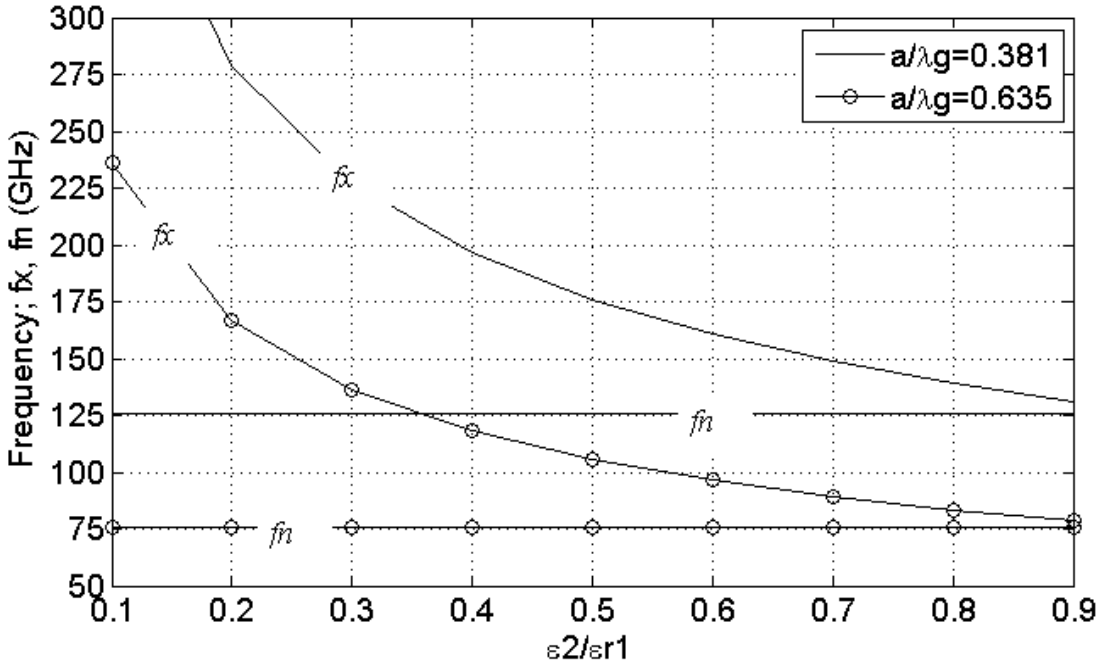

Figure 1-8: Comparison of two operation bands: a/λ_g = 0.381 and a/λ_g = 0.635. Operation at 94 GHz with a/λ_g = 0.381 using Alumina is impossible.

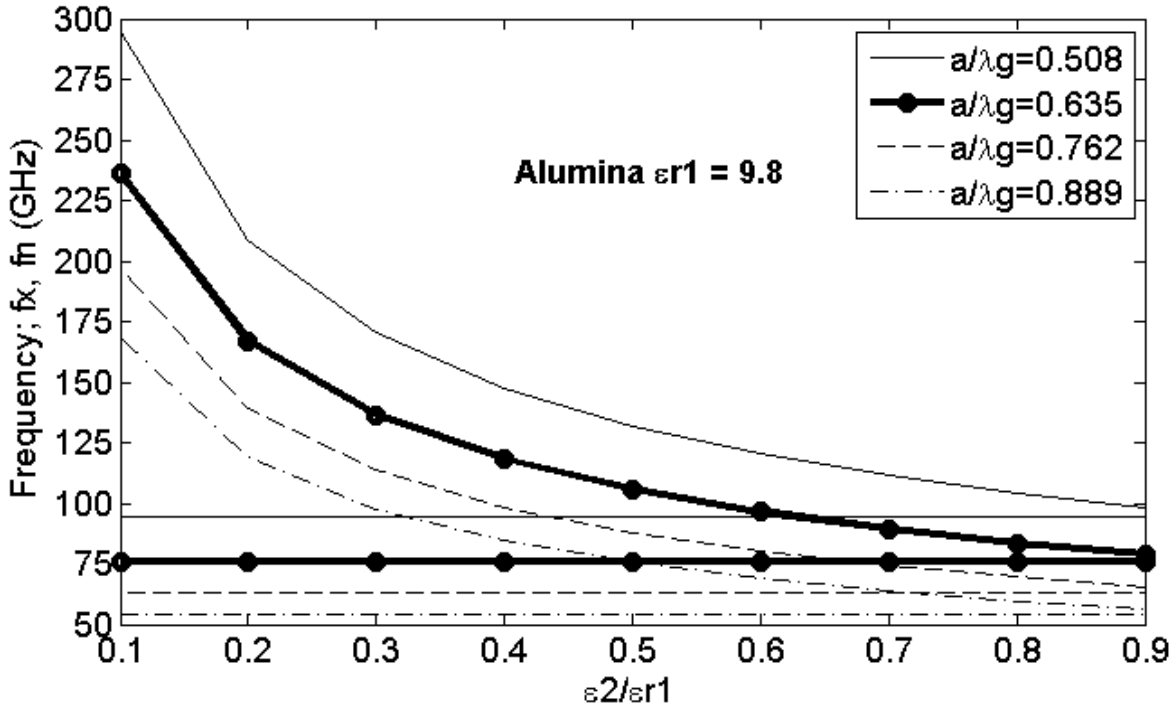

Figure 1-9: Choosing the optimum f_x-f_n band for W-band operation.

The above analysis is valid for any dielectric material and for any thickness. In fact, any particular f_g-band can be obtained with different ε_1-dielectrics by adjusting their respective thicknesses, a; as per Figure 1-10. Obviously, for the same f_g-band, higher f_x, (and thus f_g and bandwidth) values can be attained with high ε_1 dielectrics, since a smaller $\varepsilon_2/\varepsilon_1$ contrast ratio can be theoretically conceived compared to the dielectrics with smaller ε_1. This verifies the observation in [43] that high ε_1 substrates yield considerably larger bandwidth. Furthermore, compared to low ε_1 dielectrics, high ε_1 dielectrics require a smaller thickness "a" to obtain the same f_g-band; which is in-line with the miniaturization trend of RF circuits. In light of the above, the optimum substrate and its thickness, for the W-band, are Alumina and a/λ_g = 0.635, respectively.

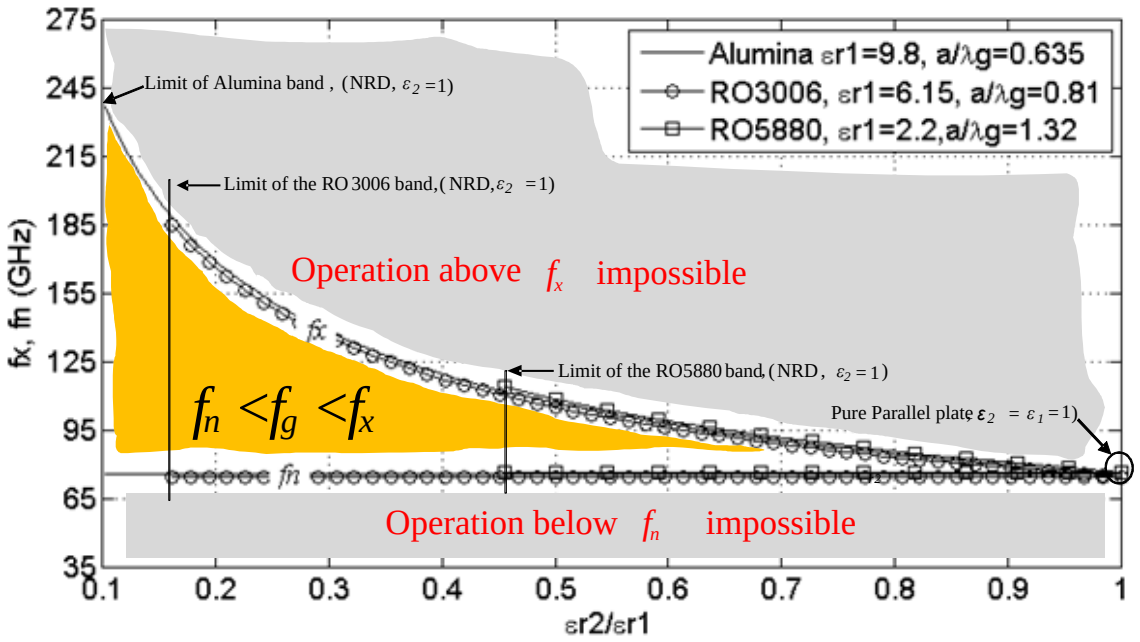

Figure 1-10: Different dielectrics with unequal thicknesses corresponding to the same f_g-band.

1.4.6 Determining channel width, *b* and effective permittivity ε_2

Intuitively, each f_g-band should in turn contain operation curves for different values of b, as shown in Figure 1-11 for Alumina (ε_1 = 9.8) with a/λ_g = 0.635. Ideally, minimizing ε_2 is desired as f_x would then be maximized; but this requires intense perforation and can increase substrate

fragility. Conversely, high values of ε_2 reflect very little perforation and thus higher susceptibility to leakage. As a compromise, $\varepsilon_2/\varepsilon_1 = 0.5$. According to Figure 1-12, this corresponds to $b = 0.826\ \lambda_g$. In terms of bandwidth ($\%\Delta f$), these values correspond to a 16.5% bandwidth, as per Figure 1-13. The bandwidth is calculated using:

$$\%\Delta f = [(f_x - f_{c,\,LSM10})/f_g] \times 100\% \qquad (1.10)$$

The choice of $\varepsilon_2/\varepsilon_1 = 0.5$ is further justified in the next subsection.

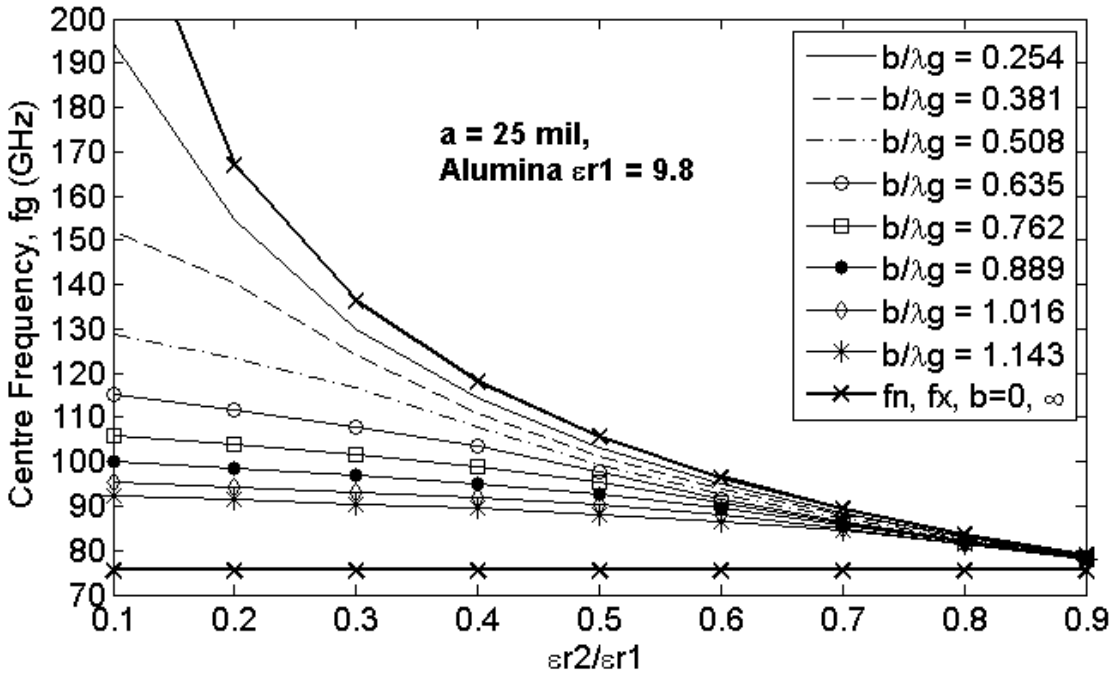

Figure 1-11: Operation curves, within an f_g-band, for different values of the width, b, and for a specific value of the thickness a.

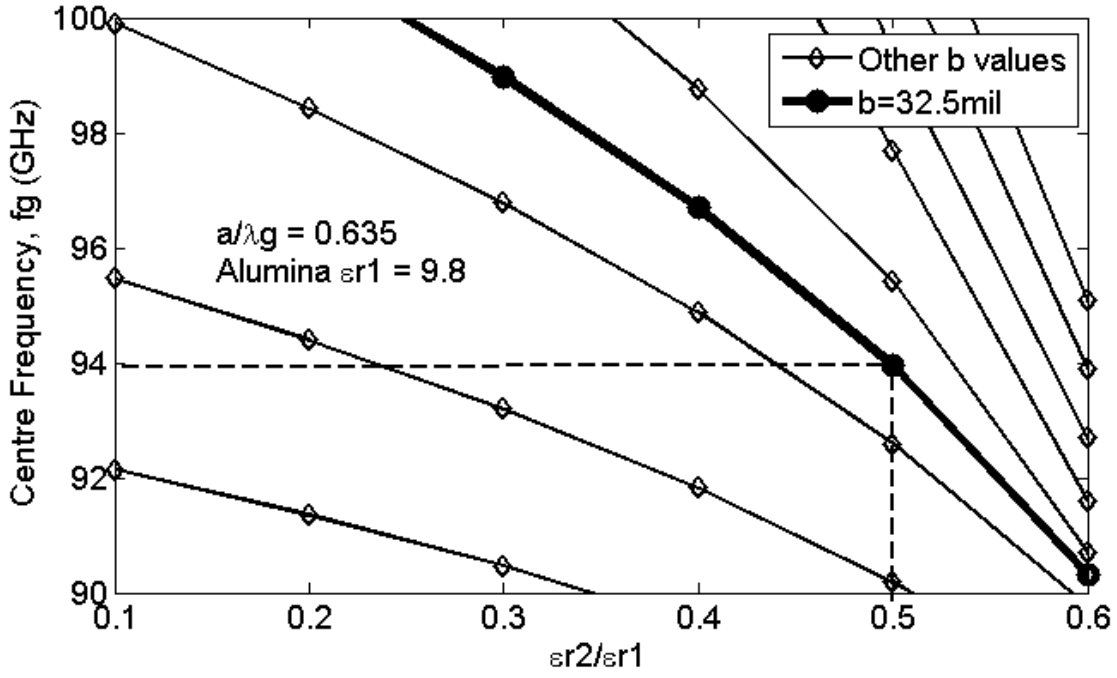

Figure 1-12: Choosing the width, b, based on the desired $\varepsilon_{r2}/\varepsilon_{r1}$ ratio operating frequency, f_g.

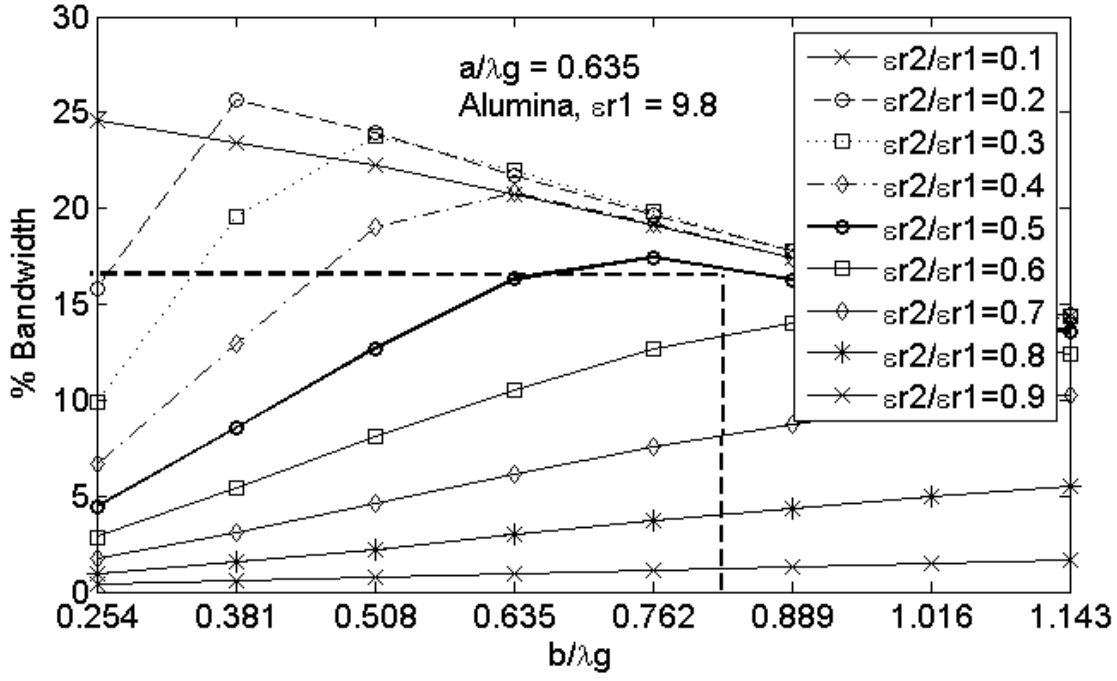

Figure 1-13: The variation of the LSM_{10} bandwidth with the width, b, for different $\varepsilon_2/\varepsilon_1$ ratios.

1.4.7 Relating ε_2 to Perforation Dimensions

The remaining task now is to choose the perforation profile. Typically, factors such as fabrication feasibility and performance significantly influence the decision. On one hand, at our lab, the most feasible perforation profile is the periodic circular-via profile. On the other hand, a square-via perforation profile models the original NRD/iNRD guide more closely (since the only difference would be the periodic inter-via gaps). Hence, a trade-off is needed that would depend on the target application and/or the performance parameter being investigated. Figure 1-14 and Figure 1-15 display the relationship between the ratio $\varepsilon_2/\varepsilon_1$ and the period p of circular-via and square-via unit-cells, respectively, for different values of *gap*. These relationships were obtained by simulating, for different *gap* values, a set of SINRD guide unit-cells with different p values, and a set of general NRD guides for different $\varepsilon_2/\varepsilon_1$ ratios, and then comparing their dispersion curves. Then, if the dispersion curves of a generalized NRD guide with $\varepsilon_2/\varepsilon_1$ = x, and an SINRD guide with p = y, *gap* = z, are identical, it means that the two are identical waveguides. For example, in Figure 1-14, a circular-via perforation profile with D/λ_g = 0.508, gap/λ_g = 0.254 (i.e. p/λ_g = 0.762) results in $\varepsilon_2/\varepsilon_1$ = 0.5 as selected above; i.e. almost 50% substrate perforation. Similarly, in Figure 1-15, a square-via perforation profile with w/λ_g = 0.55, gap/λ_g = 0.254 (i.e. p/λ_g = 0.8) would be needed to obtain the desired $\varepsilon_2/\varepsilon_1$ = 0.5 ratio. In fact, these are roughly the "safe" fabrication limits at our lab [63].

To conclude, this section provides an efficient way of choosing the optimum dimensions of the SINRD guide. Specifically, at 94 GHz using Alumina, and circular-via perforation, its dimensions are: a/λ_g = 0.635, b/λ_g = 0.826, D/λ_g = 0.508, and gap/λ_g = 0.254, respectively; corresponding to f_c = 84 GHz, and f_x = 102.5 GHz. Alternatively, the same performance can be achieved with a square-via perforation that differs from the circular counterpart only in the dimension of the square-via. In the case of the iSINRD guide, the width is $b_i = b/2\lambda_g$ = 0.413. Unless otherwise specified, those dimensions shall be used in the entirety of this thesis.

Field plots for both profiles at f_c, f_g, and f_x are shown in the Appendix B. Figure 1-16 verifies that the NRD, iSINRD and SINRD guides are identical, by plotting the dispersion curve of the LSM_{10} mode, obtained with the Eigen-mode solver using the equation (where ϕ and Δl are the phase difference and the length of the unit cell):

$$\beta = \frac{\pi\phi}{\Delta l} \qquad (1.11)$$

The calculated dispersion curve of the generalised NRD guide is also included and is identical to the simulated ones. It was obtained by solving equation 1.5 above [64]. Also included in Figure 1-16 is the propagation curve for the TE_{20} mode, obtained by solving the equation 1.7 above. It is clear that the cut-off of the TE_{20} mode in the NRD guide differs from that in the rectangular waveguide [48].

It must be mentioned that while the value of the width *b* deduced in the above discussion is the optimum for the desired f_g, other values can still be used. This is not a contradiction, given the fact that a specific value of *b* also corresponds to a bandwidth of frequencies, and thus any *b* value can well correspond to the desired f_g. The optimum value in this context refers to a value of *b* that results in a bandwidth centered at f_g. A non-optimum value of *b* then corresponds to a bandwidth that includes f_g but is centered at another frequency. This explains the reason behind using the term operating frequency instead of center frequency.

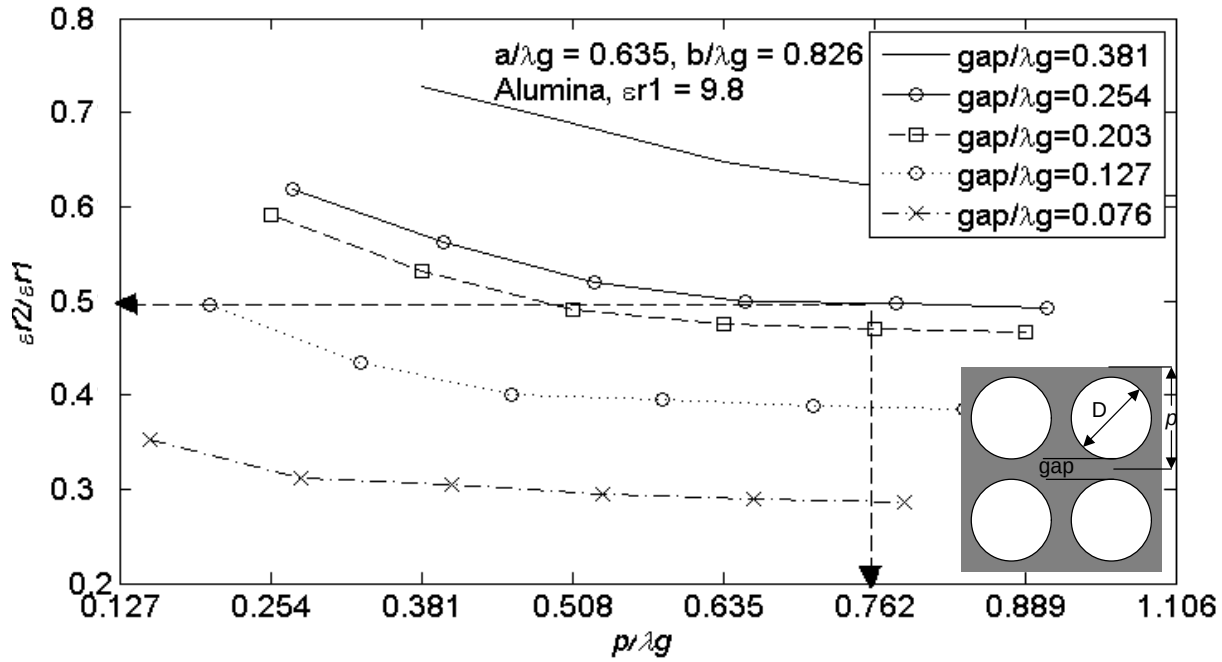

Figure 1-14: Relating $\varepsilon_{r2}/\varepsilon_{r1}$ to p/λ_g ($p = gap + D$) for the circular via profile.

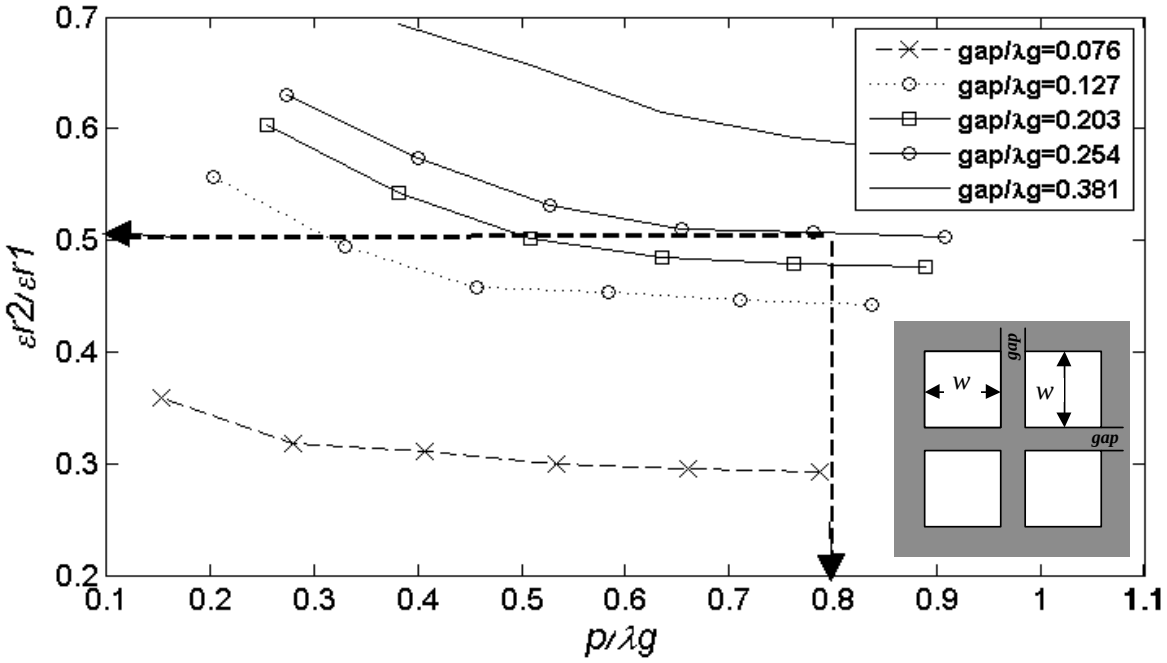

Figure 1-15: Relating $\varepsilon_{r2}/\varepsilon_{r1}$ to p/λ_g ($p = gap + w$) for the square-via profile.

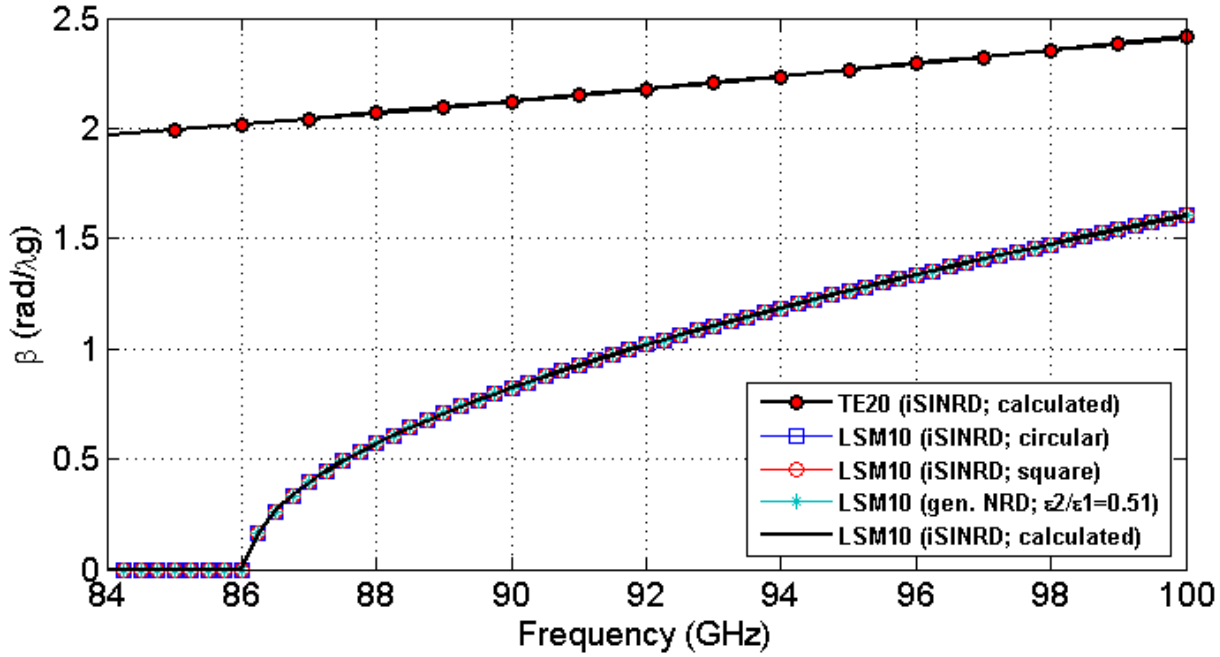

Figure 1-16: Propagation curves of the TE_{20} and LSM_{10} modes in the iSINRD guide.

1.4.8 Note on Determining ε_2

In previous studies of the SINRD guide, the effective permittivity was calculated using geometric formulae that are mainly useful for the circular-via profile. For example, according to [29], the effective permittivity ought to be calculated using:

$$\varepsilon_2 = \frac{\varepsilon_r \left\{ \left[p^2 - \pi \left(\frac{D^2}{4} \right) \right] + \pi \left(\frac{D^2}{4} \right) \right\}}{p^2} \qquad (1.12)$$

In this relationship, and others [30], the ε_2 depends only on the dimensions of the waveguide. Therefore, it assumes no frequency dependence. However, in the above curves, it is clear that there is a correlation between the frequency and the effective permittivity which must be considered during the design. This observation was also confirmed in [49]. For this reason, equation (1.12) above, or others, are not used in this work, and instead the method outlined above is employed.

1.5 Loss Analysis

For a complete characterisation of a waveguide, it is imperative to determine its loss behavior at the desired f_g. In this section, the attenuation of the iSINRD guide is compared with that of the SINRD guide and the SIW. Since [51] treats the unit cell as a resonator, its unloaded quality factor, Q, can be extracted and, thus, attenuation can be calculated using [61], [65]:

$$\alpha = \frac{f}{2Q} \cdot \frac{2\pi}{v_g} = \frac{f}{2Q} \cdot \frac{d\beta}{df} \qquad (1.13)$$

where β is the propagation constant, f is the frequency, and v_g is the group velocity.

Attenuation due to the ground conductors, α_c is calculated by replacing the PEC planes with a realistic conductor, while keeping the dielectric material as lossless ($\tan\delta$ = 0). At our lab, metalizing Alumina is routinely done with gold, thus the curves in Figure 1-17 are obtained for

gold (σ = 4.10×10^7). Notice that the α_c of the iSINRD guide are slightly higher than that of the SINRD guide counterpart; due to the vertical metallic wall in the iSINRD guide that is absent in the SINRD guide. The difference, however, is acceptable (≈ 0.025 dB/mm) at such a high f_g.

Similarly, attenuation in the dielectric α_d is calculated by entering the correct tanδ value for Alumina at 94 GHz (tanδ = 0.00015), while the electric planes are set as PEC walls. The corresponding α_d is shown in Figure 1-17. As expected, the α_d is identical in the iSINRD and SINRD guides, because both the incident power, P_i and the power dissipated in the dielectric, P_d will be halved in the iSINRD, thus the ratio $\alpha_d = (P_d / l)/(2P_i)$ is the same for both guides; l is the longitudinal length of the guide. The proof is detailed in Annex 4. The total loss α_t, is simply obtained by adding the α_c and α_d losses, and is also shown in the same Figure 1-17. Note that the curves in Figure 1-17 are obtained for the iSINRD guide with $\varepsilon_2/\varepsilon_1$ = 0.5. Finally, the total losses of the iSINRD guide are compared, in Figure 1-18, with that of the SINRD guide and the SIW, from which it can be confirmed that the attenuation of the iSINRD guide is lower than that of the SIW and comparable to those of the SINRD guide. The attenuation in the different waveguide is compared in Table 1.2.

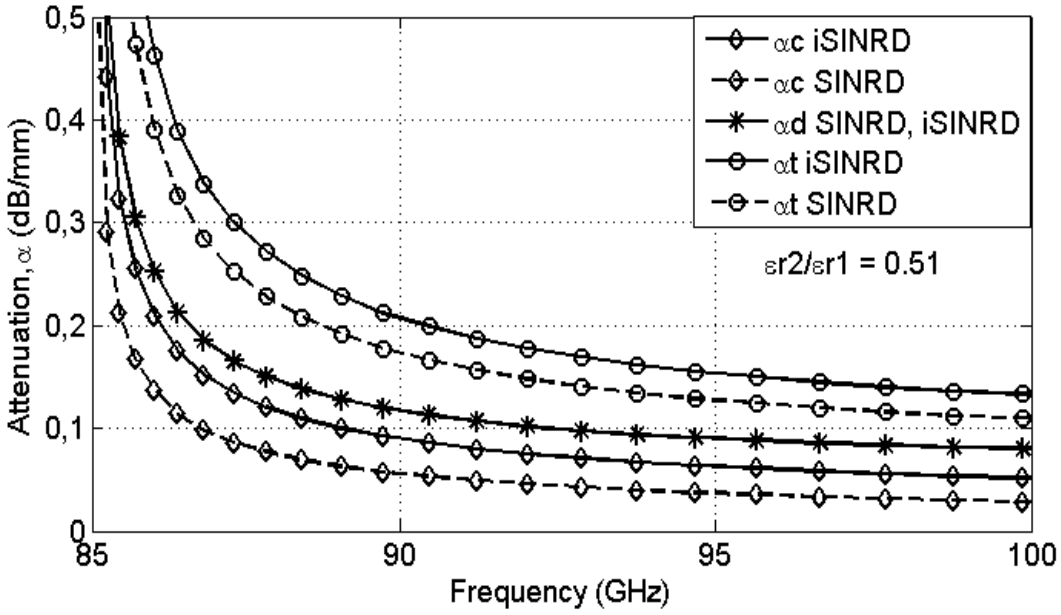

Figure 1-17: Attenuation factor due to conductor, dielectric and total losses of the iSINRD and SINRD guides.

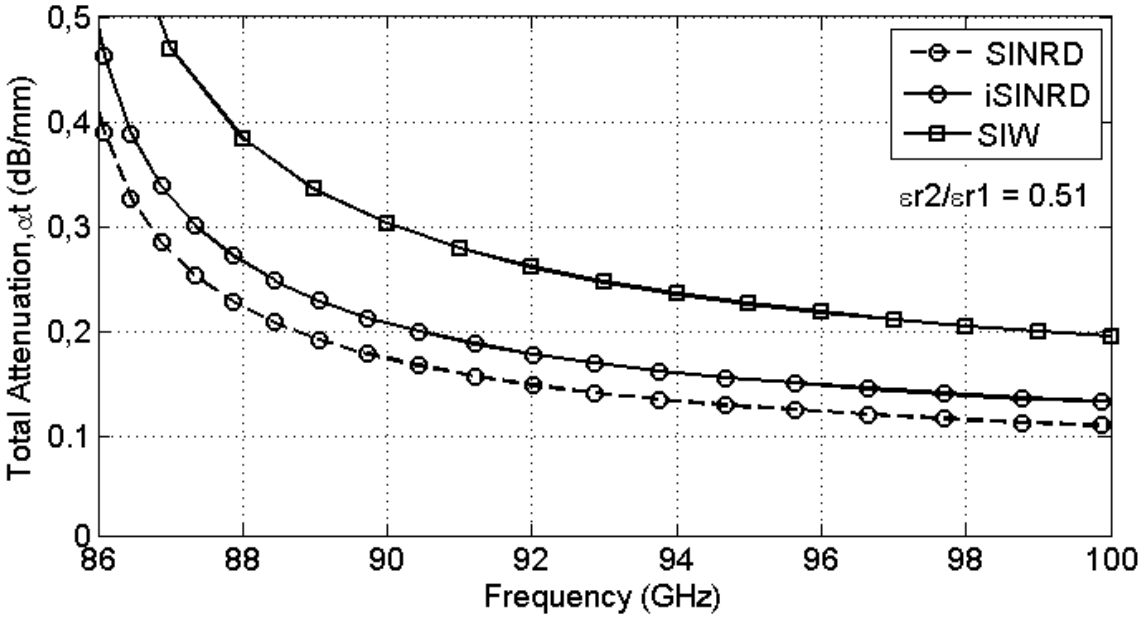

Figure 1-18: Total attenuation in the iSINRD and SINRD guides compared to the SIW.

Table 1.2: Comparison of dielectric losses in different waveguides at 94 GHz.

Wavguide	**Conductor Losses, α_c, (dB/mm)**	**Dielectric Losses, α_d, (dB/mm)**	**Ratio of $\alpha_c : \alpha_d$**	**Total Losses, α_t, (dB/mm)**
SIW	0.138	0.092	1.5:1	0.23
SINRD	0.04	0.095	0.42:1	0.13
iSINRD	0.06	0.095	0.63:1	0.16

1.6 Discussion

The image Substrate Integrated Dielectric (iSINRD) guide is introduced as an improvement to the SINRD guide. It is simply realised by dissecting the latter with a longitudinal metal wall. Thus, it offers 50% compactness, and suppresses the LSE_{10} mode. The latter is a nuisance for NRD circuits involving bends, and its suppression facilitates the use of the iSINRD guide in many novel applications. An alternative and simple methodology for designing general NRD-

class guide circuits was also devised and discussed. Specifically, it aids in accurately justifying the choice of dimensions for the guide, as well as the choice of the perforation profile. The advantage of this methodology is that a maximum of only two graphs (Figure 1-7 and a graph similar to Figure 1-14) is required to determine all the dimensions, even though the iSINRD involves *at least* three times the number of parameters of the original NRD guide. Furthermore, if a dielectric of effective permittivity is used instead of air, then only one graph (Figure 1-7) is needed.

An attenuation study of the SINRD and image SINRD (iSINRD) guides was also performed at the W-band frequency of 94 GHz using Alumina substrate. The two guides exhibit low attenuation (of less than 0.2 dB/mm); which is rather low at such high frequencies. Then the attenuation of the two guides was compared to that of the SIW. The attenuation of the latter is considerably higher than the iSINRD guide, which justifies the use of the iSINRD guide for W-Band applications. The simplified design methodology presented in this chapter is utilized in the next chapter in the design of different iSINRD guide transmission lines that are based on circular as well as square profiles.

Chapter 2 IMPLEMENTATIONS OF THE iSINRD GUIDE AT THE W-BAND FREQUENCIES

2.1 Introduction

The objective of this chapter is to investigate the possibility of designing the image NRD guide with the SICs technology. Towards this end, a number of image SINRD (iSINRD) guide circuits that operates at the W band, with center frequency of 94 GHz, are designed and tested. The design circuits include two iSINRD guides with continuous metal walls that correspond to the circular and square perforation profile, two iSINRD guides each with different gaps in the metal wall, and two iSINRD guide bends. These circuits are the building blocks of more sophisticated iSINRD guide circuits that are presented in Chapter 3 and Chapter 4. Therefore, it is worthwhile investigating the performance of those building blocks before incorporating them in larger designs.

2.2 Continuous and Discontinuous Walls

It is intriguing to investigate the effect of using a discontinuous metal wall instead of a continuous wall. Such a scenario can be realized with a row of periodic metalized slots. In this case, it is imperative to investigate the leakage loss due to the gaps between the slots, in order to determine the optimum number and spacing between gaps (*gs*). Indeed, Figure 2-1 depicts the effect, on the insertion loss, of varying the number and dimensions of the gaps; assuming lossless dielectric and conductors. It is interesting to note that the leakage loss due to 1 gap with gs/λ_g = 0.254 and 2 gaps with gs/λ_g = 0.127 are identical. If the objective is strictly designing an SINRD guide circuit, then a maximum of two gaps with gs/λ_g = 0.127 or one gap with gs/λ_g = 0.254 should be used so as to minimize the leakage loss. Conversely, in applications such as leaky wave antennae, more gaps with a larger value of *gs* might deliberately be used to enhance the radiation pattern. It must be noted that the introduction of gaps does not hinder the propagation of the LSM_{10} mode because the surface currents on the conducting walls depend mainly on the longitudinal component of the magnetic field (equation 1.1f, as shown in Figure 2-2 and Figure 2-3).

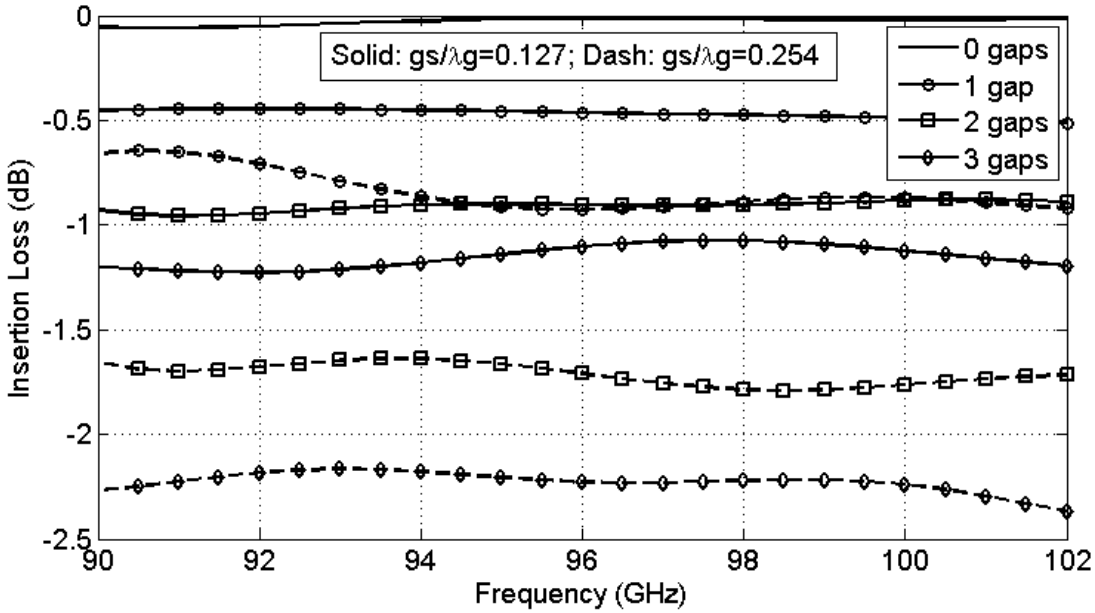

Figure 2-1: The leakage loss in discontinuous-iSINRD guide compared to continuous-iSINRD guide (0 gaps).

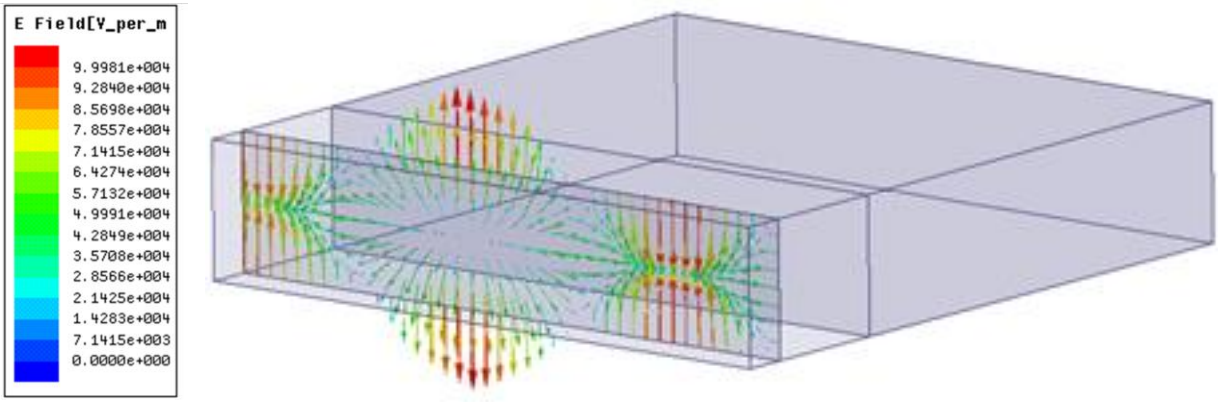

Figure 2-2: Current distribution of the E-field of the LSM_{10} mode in the continuous-wall iSINRD guide.

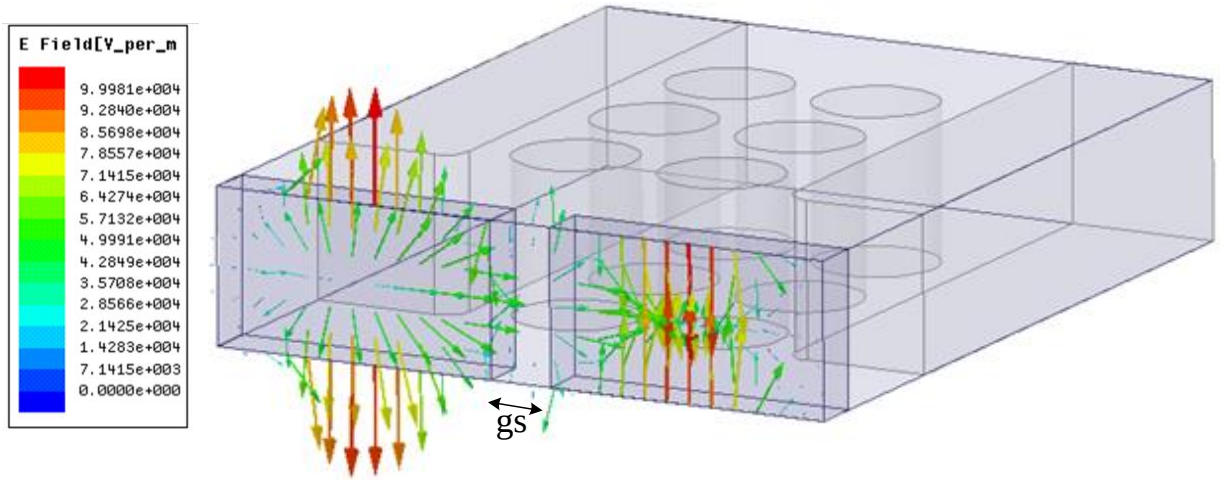

Figure 2-3: Current distribution of the E-field of the LSM_{10} mode in the discrete-wall iSINRD guide.

2.3 iSINRD Guide Bends

The design of iNRD guide bends is yet to be reported in the literature. It is intuitive to postulate that iNRD and iSINRD guide bends will substantially enhance the design of circuits in the NRD paradigm; thanks to the suppression of the LSE_{10} mode. In other words, unlike NRD and SINRD guide bends, the bends in iNRD and iSINRD guides do not involve from LSE_{10} - LSM_{10} mode conversion. Coupled with the fact that the iSINRD guide is immune to radiation at bends, this opens the door to the design of a myriad of novel iSINRD guide single-mode circuits; as shall be demonstrated in subsequent chapters.

Figure 2-4 illustrates two possible geometries of the iSINRD guide bends; magnetic wall corresponds to the air region of the iSINRD guide. The choice of the bend variant (Case I or Case II) is application-specific.

This bend geometry was chosen as its S-matrix, shown in equation (2.1) and (2.2) for Case I and Case II respectively, can easily be derived using the even-odd analysis that is detailed in Chapter 4.

$$[S_I] = \begin{bmatrix} \tau & \chi \\ \chi & \tau \end{bmatrix} \qquad (2.1) \qquad [S_{II}] = \begin{bmatrix} \kappa & \zeta \\ \zeta & \kappa \end{bmatrix} \qquad (2.2)$$

This is based on the fact that either bend can be decomposed along the line *m-n* into separate arms (A, B and C), with the relevant boundary condition. Then the S-parameters can be obtained according to:

$$\tau = \frac{1}{4}(R_A + R_B) \qquad \chi = \frac{1}{4}(R_A - R_B) \qquad (2.3)$$

$$\kappa = \frac{1}{4}(R_B - R_C) \qquad \zeta = \frac{1}{4}(R_B + R_C) \qquad (2.4)$$

The variables τ, χ, κ and ζ are the entries of the S-matrix of each bend, while R_A, R_B and R_C are the reflection coefficients the arms A, B, and C that result from the decomposition. In fact, with the optimum dimensions from section 1.4, two iSINRD bends (one for each variant) were designed and simulated using [51]. For simplicity, the side region is treated as a substrate with a lower effective permittivity. The simulation results, together with the S-parameters calculated using (2.3) and (2.4) for each bend are shown in Figure 2-5 and Figure 2-6, respectively. Excellent agreement between the simulated and calculated results is observed. The field plots for each bend are shown in Figure 2-7 and Figure 2-8 respectively. The response of the Case I bend is narrow band compared to the broadband response of the Case II bend. This is attributed to the fact that, for Case I, the width of the guide in the bend section is smaller when compared to the arms. While this width variation applies to the Case II as well, the LSM_{10} mode is not significantly affected because the affected area corresponds to the air region; i.e. where the field exponentially decays. These bends are indispensable for the designs in the subsequent chapter, as they will be used to facilitate the excitations of the couplers in Chapter 3, in addition to being involved in the design of iSINRD cruciform hybrids in Chapter 4.

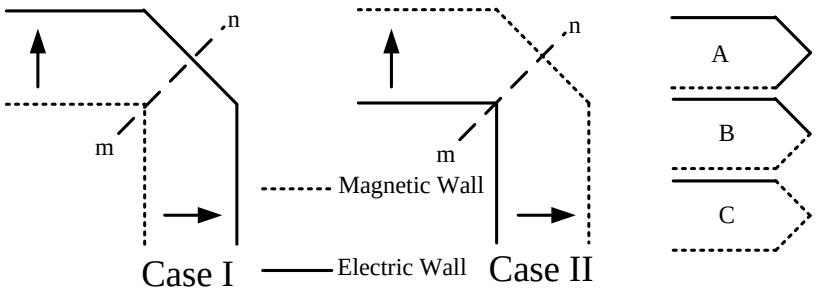

Figure 2-4: Top view of two possible geometries of the iSINRD guide bends (left and center). Right: the arms that result as a consequence of decomposing the bends I or II along the symmetry line m-n and thereafter applying PEC and PMC boundary conditions.

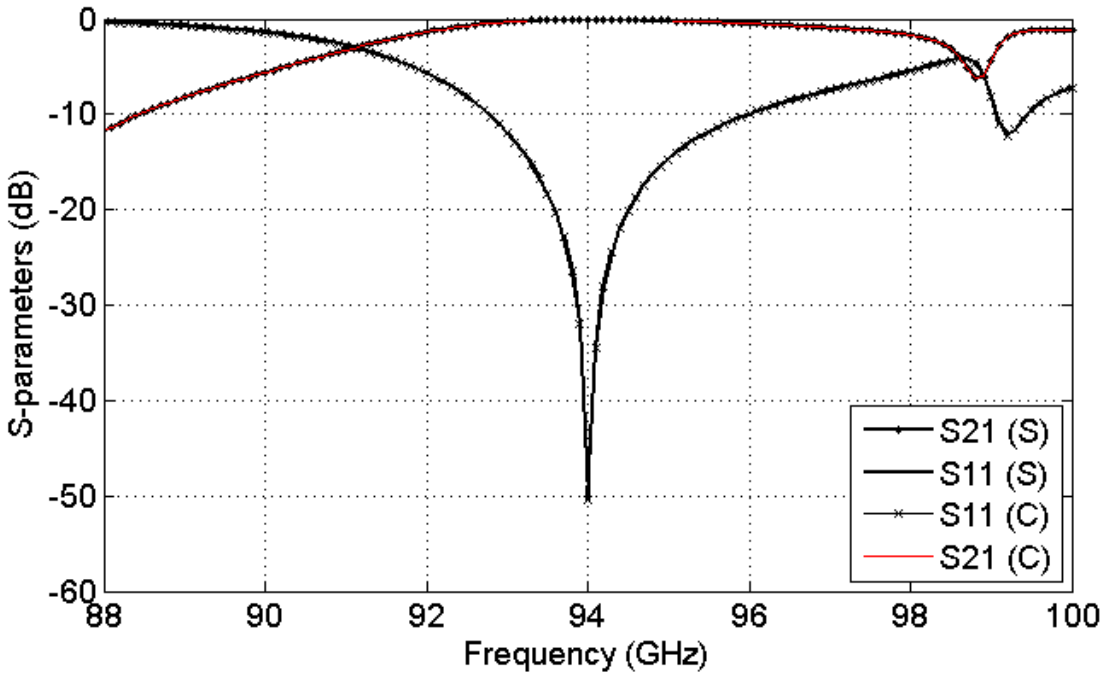

Figure 2-5: The simulated (S) and calculated (C) S-Parameters of the Case I iSINRD guide bend.

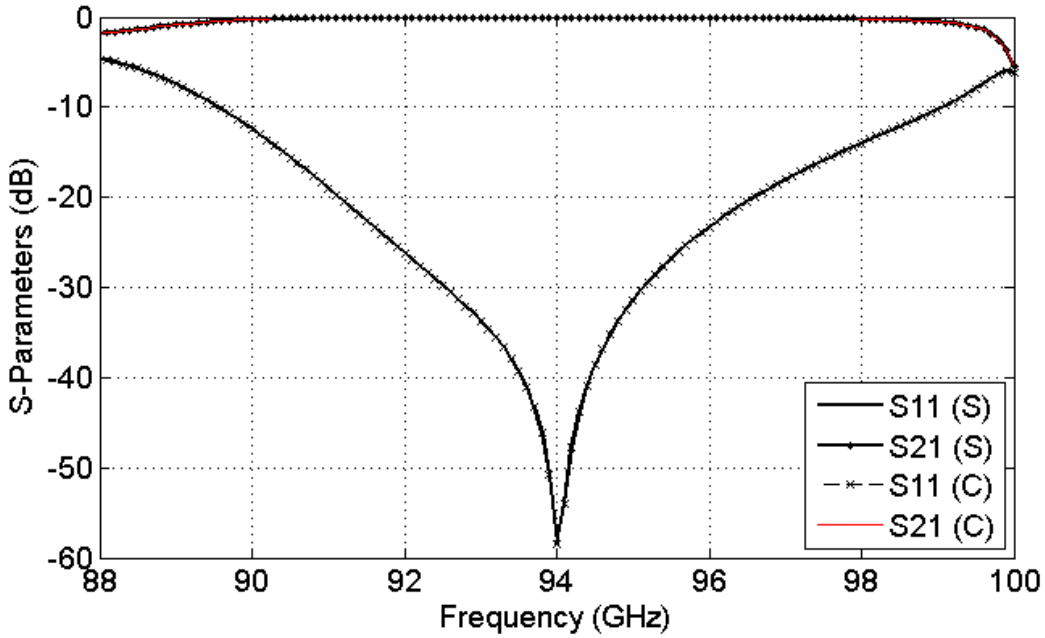

Figure 2-6: The simulated (S) and calculated (C) S-Parameters of the Case II iSINRD guide bend.

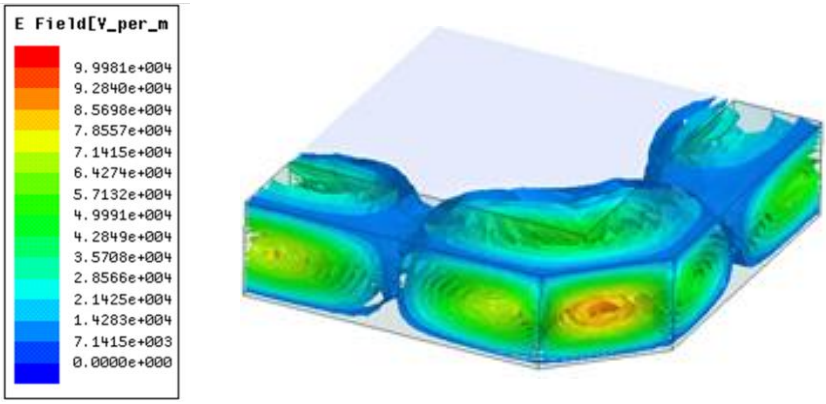

Figure 2-7: A 3-D plot of the electric field of the LSM_{10} mode in the Case I iSINRD guide bend.

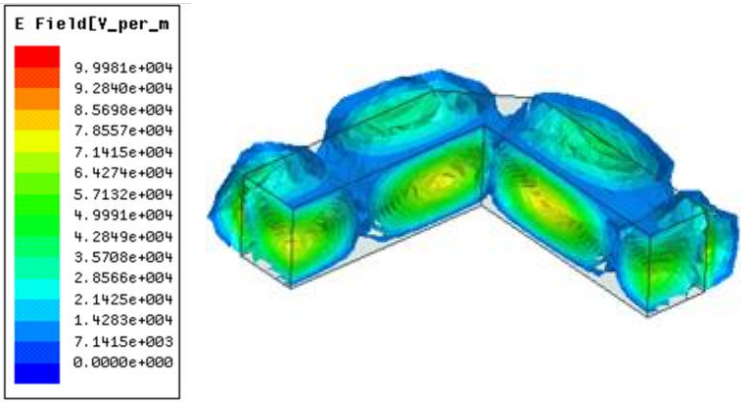

Figure 2-8: A 3-D plot of the electric field of the LSM_{10} mode in the Case II iSINRD guide bend.

Bends other than the 90^o bends discussed above are also possible, where the angle variation correspondingly varies the S-parameters. This is schematically illustrated in Figure 2-9. The effect of angle variation on the reflection each bend (cases I and II) are shown in Figure 2-10 and Figure 2-11, respectively, which also include the response due to the 90^o bend. It is clear that the reflection of the 90^o bend is better compared to the other bends at the resonant frequency. The results are tabulated in Table 2.1.

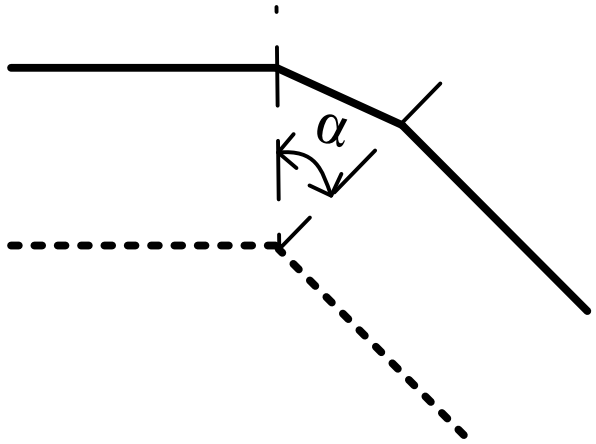

Figure 2-9: Varying the bend angle α.

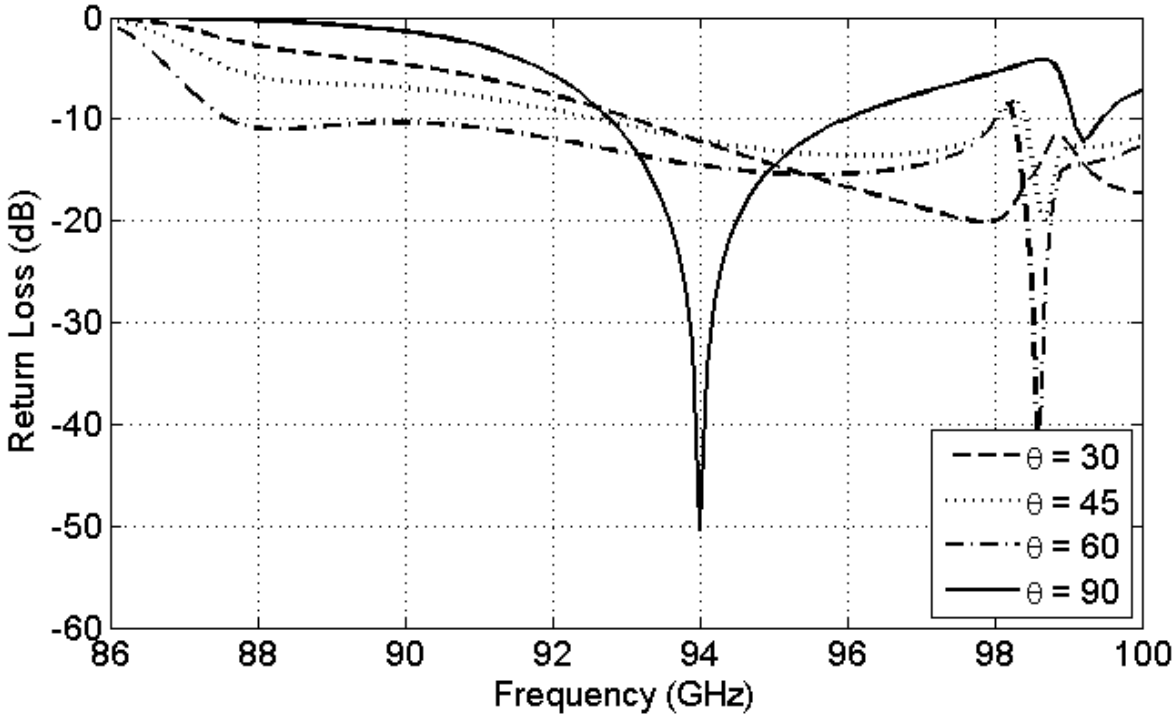

Figure 2-10: Variation of the return loss with respect to the bend angle (Case I).

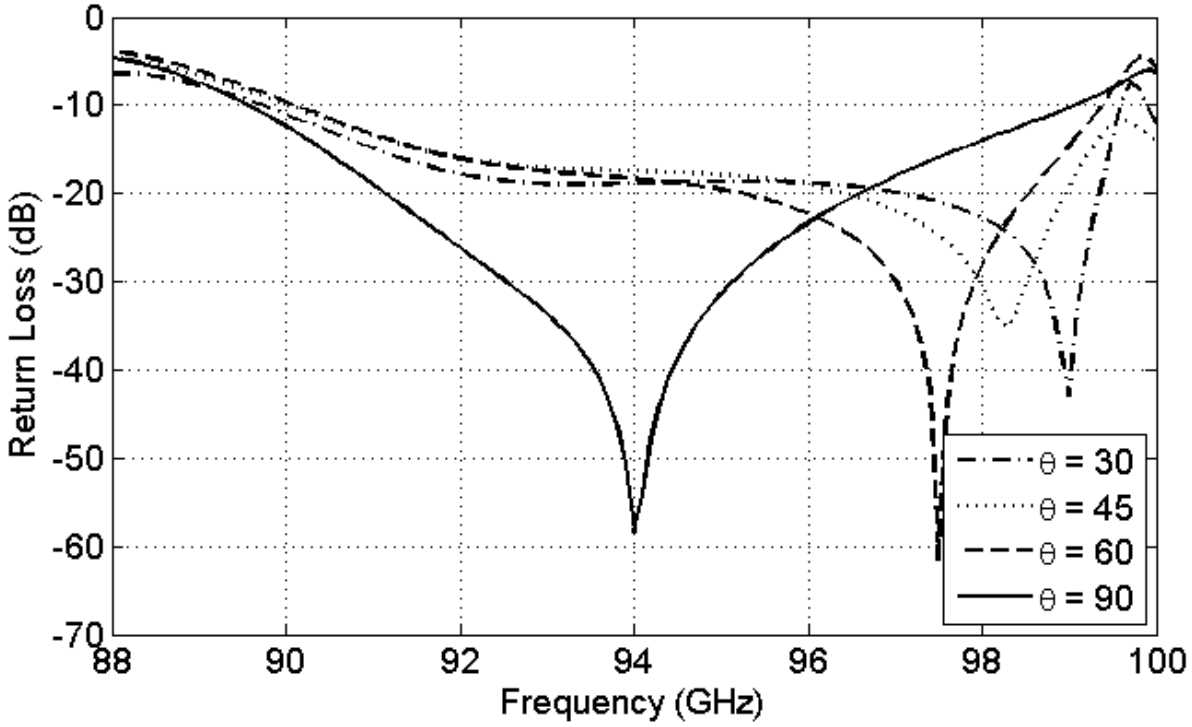

Figure 2-11: Variation of the return loss with respect to the bend angle (Case II).

Table 2.1: Correlation between the bend angle theta and the return loss at 94 GHz

α (degrees)	**CASE I: S11 (dB)**	**CASE II: S11 (dB)**
30	-17	-11
45	-18	-13
60	-19	-15
90	-58	-50

2.4 Experimental Results and Discussion

2.4.1 iSINRD Transmission Lines

With the optimum dimensions of Chapter 1, continuous wall iSINRD guides (corresponding to the circular-via and square-via profiles, as well as the lossy RO6010 substrate), shown in Figure 2-13 to Figure 2-15, were fabricated and measured. Feeding of the LSM_{10} mode is done using a tapered transition to WR10 waveguide, as detailed in [66]. Due to fabrication limits at our lab, the total length of all transmission lines in this chapter is 5.25 mm, excluding the tapered section of the line, which has a length of 0.6 mm each.

The theory from section IV predicts that there is no difference between the circular and square profiles (assuming that appropriate dimensions, pertinent to each profile and corresponding to the same ε_2, were selected). This is reflected in the almost identical simulated S-parameters of the two profiles, shown in Figure 2-16. This is further validated by comparing their simulated responses with their respective measured S-parameters, shown in Figure 2-17 and Figure 2-18. In both cases, an insertion loss of around 1dB and a reflection better than 15 dB was obtained. The slight frequency shift is attributed to the fact that for this particular prototype, the 2-mil oversize fabrication rule mentioned in [63] was not respected, which led to larger via diameters (i.e. smaller $\varepsilon_2/\varepsilon_1$ ratio) and smaller width. The 2-mil oversize is caused by the fact that the laser with which the substrate is cut has a diameter of 2-mil. This is schematically illustrated in Figure 2-12. Consequently, the operating frequency is slightly shifted upwards as expected from Figure 1-12 and Figure 1-14 in Chapter 1. In all subsequent design, this effect is taken into consideration during the design and fabrication process. The measured S-parameters of the circular via RO6010 iSINRD guide, shown in Figure 2-19, are self-explanatory; Alumina is the choice for iSINRD guide design at the W-band frequencies.

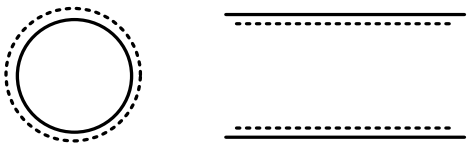

Figure 2-12: Intended dimensions (solid) and fabricated dimensions (dashed).

The ripples in the return loss are attributed to the periodicity of the perforation profiles, which causes multiple reflections that, depending on the frequency, results in destructive or constructive interference. The ripples are more pronounced with the square vias compared to the circular ones because of the sharp corners. The square vias, however, are easier to design and fabricate since they closely resemble the original NRD guide. A design trade-off is therefore required. In the rest of this work, the square vias are chosen. Finally, the operation of all measured prototypes ends at around 102 GHz, which is the f_x limit predicted in Chapter 1.

Figure 2-13: Top view of a fabricated iSINRD guide (continuous metal wall, circular profile).

Figure 2-14: Top view of a fabricated iSINRD guide (continuous metal wall, square profile).

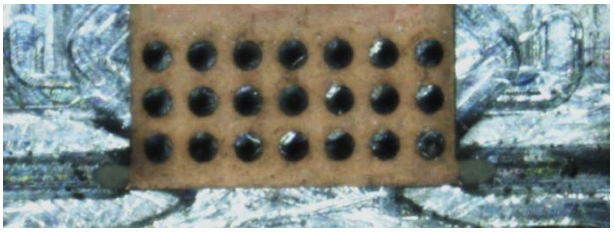

Figure 2-15: Top view of the fabricated iSINRD guide prototype (continuous metal wall, Rogers RO6010 substrate).

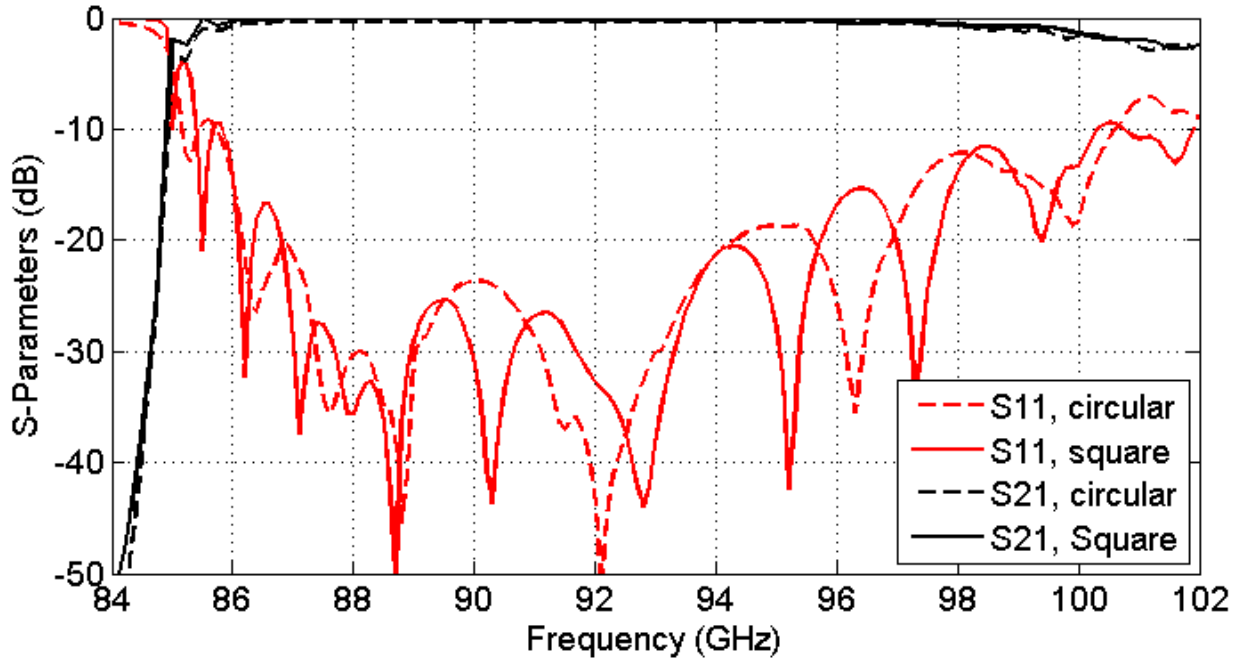

Figure 2-16: The simulated S-parameters of the circular via and square via profiles.

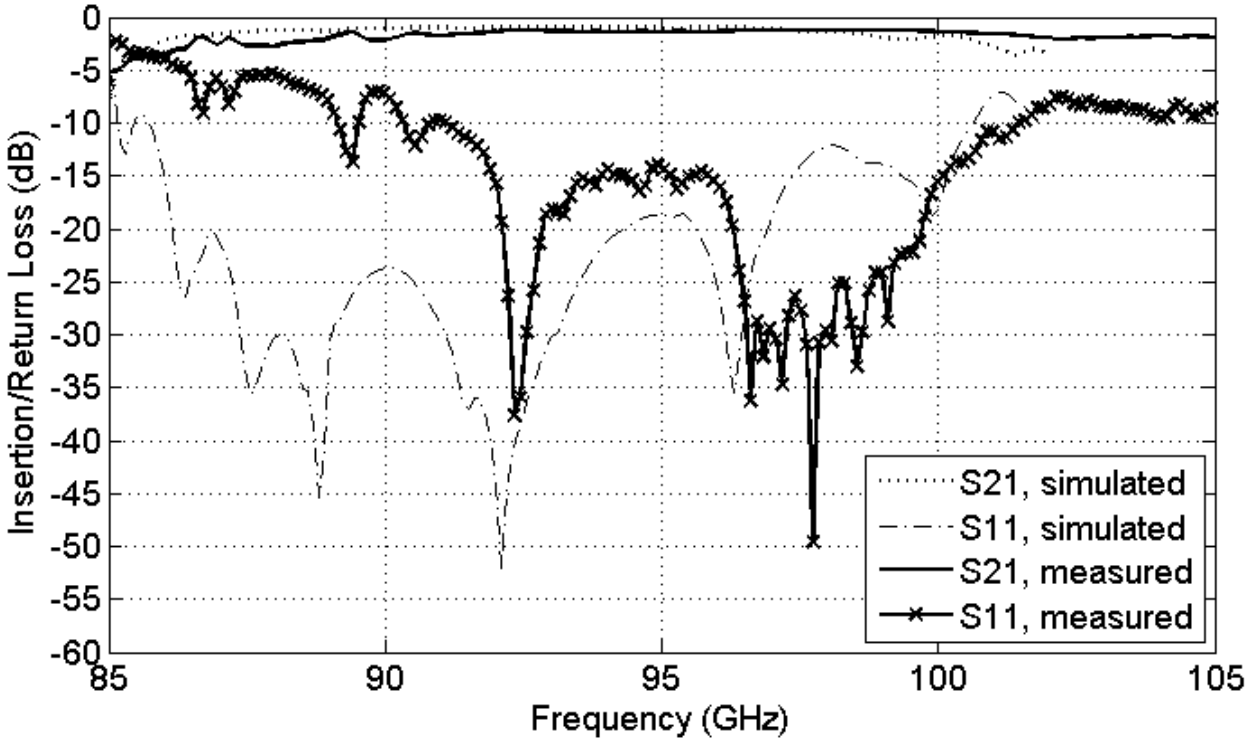

Figure 2-17: The simulated and measured S-parameters for the circular via iSINRD guide.

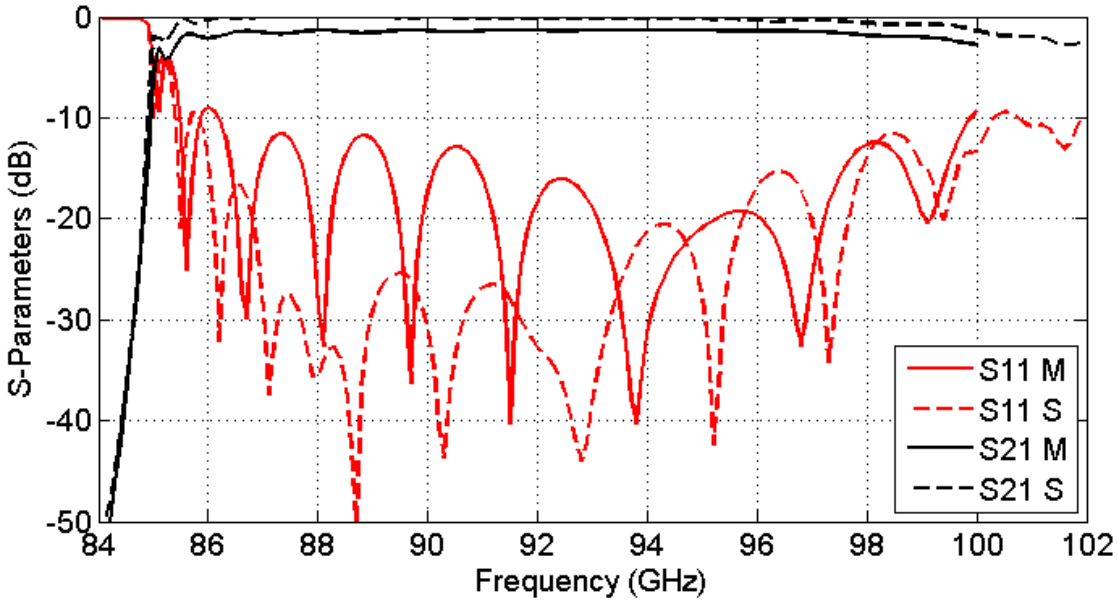

Figure 2-18: Simulated (S) and measured (M) S-parameters for the square via iSINRD guide.

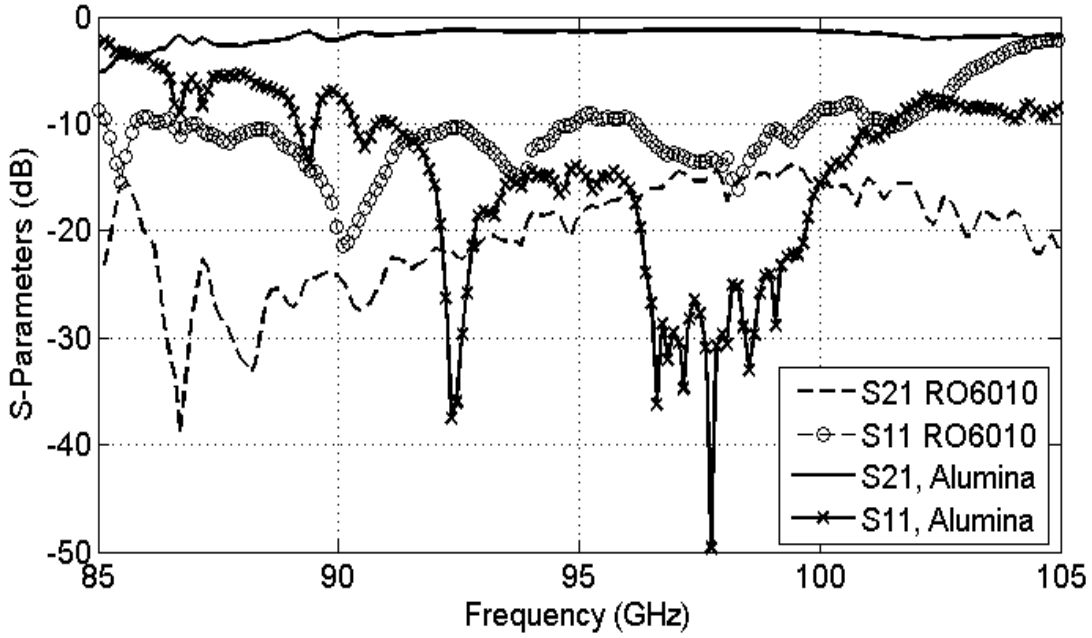

Figure 2-19: Measured S-parameters for the circular via Alumina and RO6010 iSINRD guides.

2.4.2 iSINRD Guide with Gaps in the Metal Image Wall

Two iSINRD guides with 1 and 3 gaps were also fabricated and measured. As stated above, the length of the transmission lines is 5.25 mm. The size of the gap, measured along the length of transmission line, is gs = $0.254\lambda_g$. The lateral dimension of the gap, which is orthogonal to the longitudinal length of the line, is approximately 0.5 mm. Again this dimension was chosen to respect fabrication guidelines, which also dictate a minimum distance of 0.1 mm between the edge of the substrate and the first air via.

The fabricated prototypes are shown in Figure 2-20. The measured return and insertion losses are shown in Figure 2-21 and Figure 2-22; respectively. For comparison, the curves for the continuous-wall iSINRD guide were also included. In the case of the iSINRD guide with one gap, the measured insertion loss is around 1.3 dB at 94 GHz. On the other hand, the insertion loss for the guide with three gaps is around 2.5 at 94 GHz. As is apparent, those measurements are in close agreement with the analysis conducted in Section 1.6, and it confirms that the introduction of gaps in the image has a significant effect on the insertion loss. The larger measured loss, however, is attributed to the fact that the fabricated gaps have a lateral dimension which was assumed to be null during simulation. This lateral dimension, albeit small relative to the longitudinal dimension, augments the conductor (and thus the total) losses. Contrary to that, the return loss is mildly affected, being 18 dB (at 94 GHz) or better for both the 1-gap and 3-gap prototypes. This is expected since the only difference between those waveguides and the continuous wall case is the gap which mainly results in leakage into the substrate.

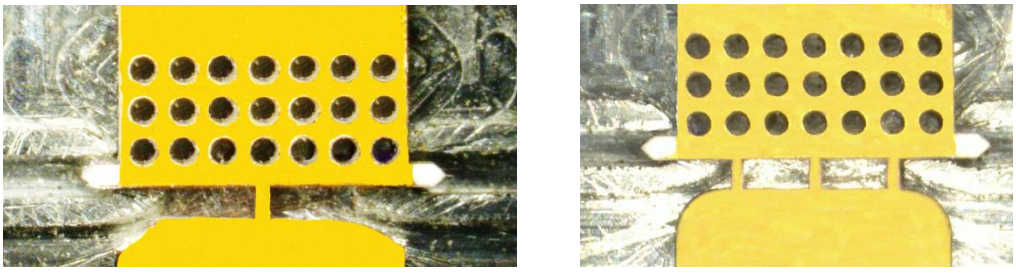

Figure 2-20: Top view of an iSINRD guide with one gap (left) and three gaps (right).

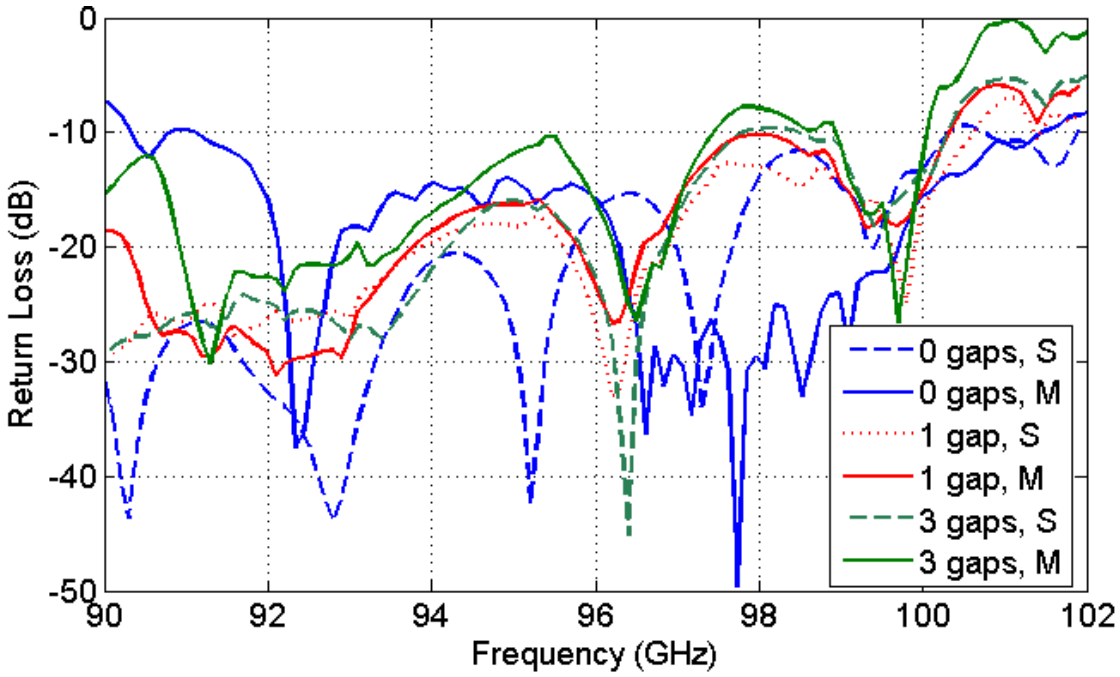

Figure 2-21: The simulated (S) and measured (M) return losses for different gaps.

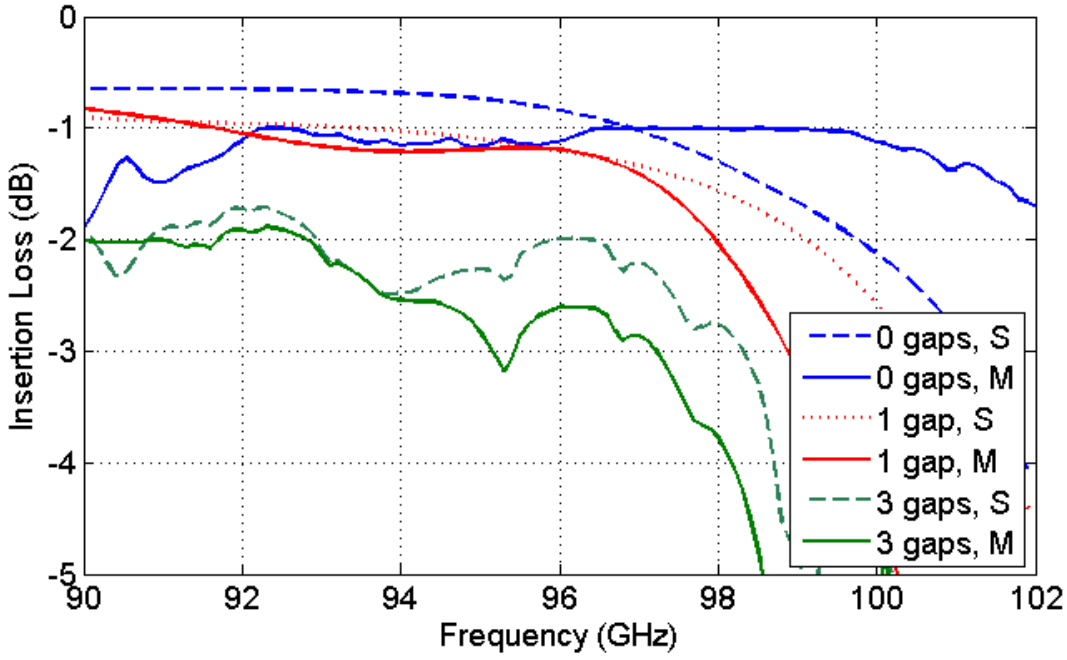

Figure 2-22: The simulated (S) and (M) measured insertion losses for different gaps.

2.4.3 iSINRD Guide Bends

To validate the operability of bends discussed in Section 2.3, a square-via prototype for each case, shown in Figure 2-23 and Figure 2-24 was fabricated and measured using Alumina with the dimension from section 1.4. The image wall is simply provided by manually filling each gap with silver epoxy, which substantially saves fabrication time and overhead. The total size of each bend is 4×4 mm^2. The total length of each taper is 0.6 mm. The measurement results for each bend variant are plotted together with the corresponding simulated ones in Figure 2-25 and Figure 2-26. The simulated responses in those figures include the effect of the air vias which was not considered in the analysis conducted in Section 2.3. This explains the ripples in the return loss which are not observed in the analysis conducted in Section 2.3. Furthermore, the ripples in the measurements are more pronounced compared to the simulations. This is mainly attributed to the small gap (0.1 mm) between substrate edge and the metal image wall, which was not accounted for in the simulation. Otherwise, the measured and simulated results are in satisfactory agreement.

Figure 2-23: Top view of a fabricated Case I iSINRD guide bend.

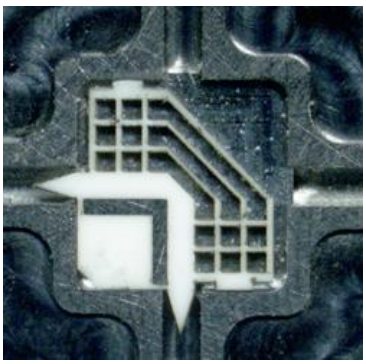

Figure 2-24: Top view of a fabricated Case II iSINRD guide bend.

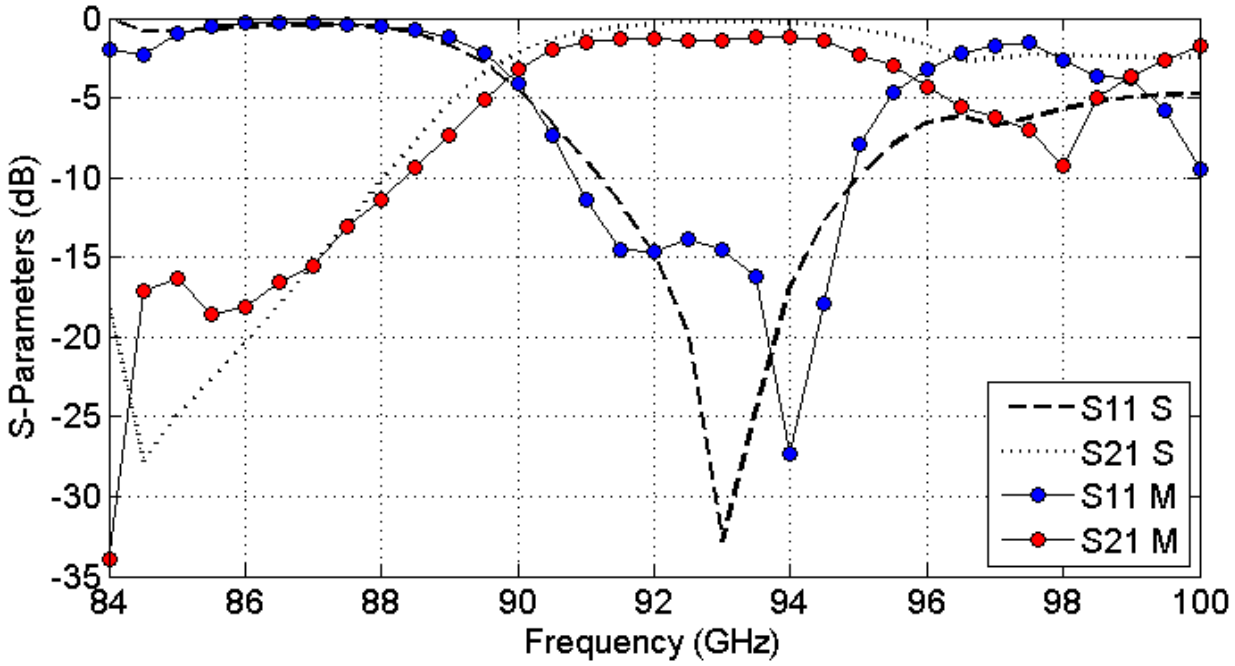

Figure 2-25: The simulated (S) and measured (M) results of the Case I iSINRD bend.

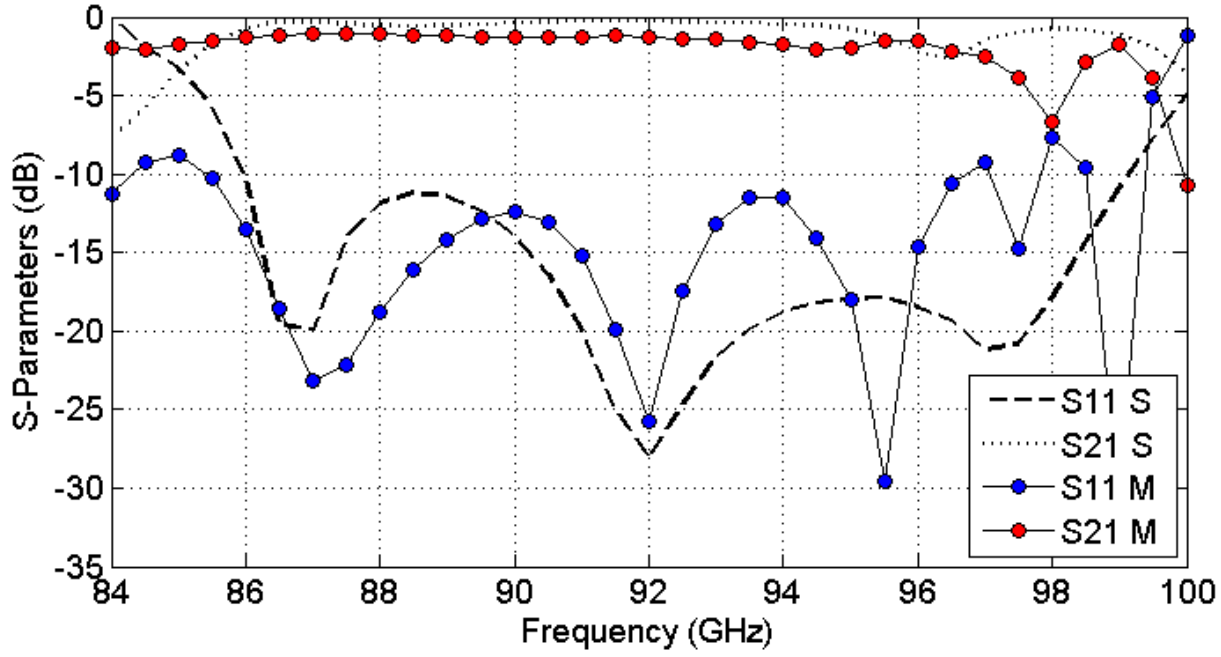

Figure 2-26: The simulated (S) and measured (M) results of the case II iSINRD bend.

Chapter 3 THE iSINRD GUIDE IN THE CONTEXT OF DIRECTIONAL FORWARD COUPLERS

3.1 Introduction

In this section/chapter, the versatility of the iSINRD guide and the symmetry of its dominant LSM_{10} mode, in addition to its orthogonality to the TE_{10} mode, are further highlighted by investigating its potential for the design of symmetric and asymmetric directional couplers. In those couplers, the power is periodically exchanged over the length of the coupling section, and different coupling levels can be attained by adjusting the length of the coupling section [67–69]. The cornerstone in the design of symmetric directional couplers is cascading two identical waveguides in a parallel fashion [67]. Asymmetric coupling is realized in a similar way, except for the fact that the parallel couplers are not identical; that is, they differ in their lateral dimensions or other parameters [67]. Coupling between the parallel waveguides then takes place in two ways; continuously over the length of the coupling section; as illustrated in Figure 3-1, or through discrete number of apertures between them; as in Figure 3-2 [67]. Each coupling mechanism entails a distinct design approach. In the continuous length case, the ratio of power transfer is strongly dependent on the value of the length. In the discrete case, the power transfer ratio depends on the dimension of and spacing between the coupling apertures, as well as the number of apertures. Relating the coupling level to the dimensions of the coupling section and apertures is primarily done using a set of parametric design curves [67]. In the SICs paradigm, the discrete coupling mechanism is more befitting, and is applied in the following sections to design a set of iSINRD directional couplers. The discussion spans both symmetric and asymmetric discontinuous iSINRD directional couplers, focusing on 3-dB and 0-dB coupling levels. In addition, the focus of this analysis is the forward directional couplers, where the coupled signal propagates in the same direction as the incident signal.

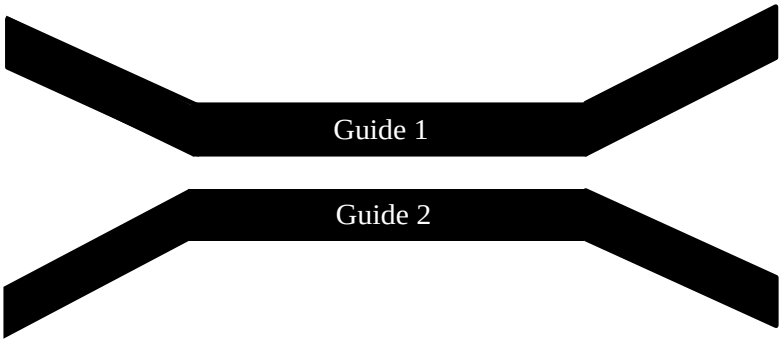

Figure 3-1: Continuous coupling between two parallel waveguides/lines.

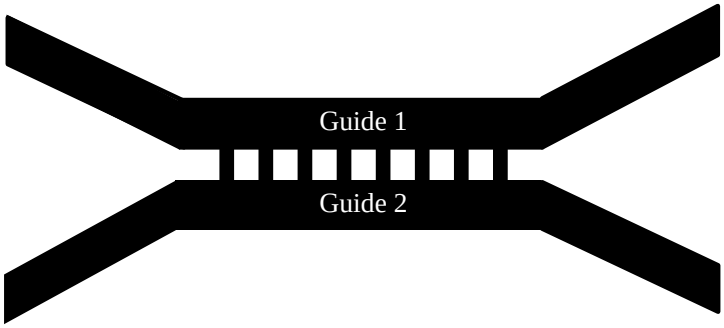

Figure 3-2: Discrete coupling between two parallel waveguides/lines.

3.2 Symmetric Directional Couplers based on the iSINRD Guide

3.2.1 Type A Coupler

Consider the structure in Figure 3-3. Depending on the excitation method and the mode that is being excited, the structure can be interpreted in various ways. If it is a two-port structure, then it can be viewed as a conventional SINRD guide with a central metal suppressor (that suppresses modes other than the LSM_{10} mode). Alternatively, it can also be viewed as a four-port circuit, in which case it strictly represents two parallel iSINRD guides that share their (discontinuous) metal side walls. In the latter case, the gaps between the metal vias simply allow the LSM_{10} mode to "leak" into the adjacent iSINRD guide; as per the discussion in Chapter 2. However, since the boundary conditions are identical in both guides, the LSM_{10} mode continues to propagate in the other guide as well, resulting in directional coupling along the length of the coupling section

(length *l*). The coupling level is then a complex function of the various via parameters; namely its width (*x*) and length *w*, the spacing (*g*) between consecutive vias, and the number of coupling elements or vias (*nvia*). As per the theory in [67], however, the losses due to the coupling apertures are proportional to their number, as well as their size. Furthermore, the analysis in Chapter 1 revealed that conductor losses are more dominant than dielectric losses in the iSINRD guide. Therefore, as a first step towards loss reduction, the smallest conceivable size of the vias is considered, that is $x/\lambda_g = w/\lambda_g = 0.254$. This reduces the complexity of the design as only two variables, *g* and *nvia*, need to be investigated. The way in which *g* and *nvia* affect the coupling level is such that more tight coupling can be achieved by increasing *g* and reducing *nvia* and vice versa; in line with the observation in Figure 2-1 in Chapter 2. The objective should then be to choose less number of vias with larger separation *g* so as to further reduce the conductor losses.

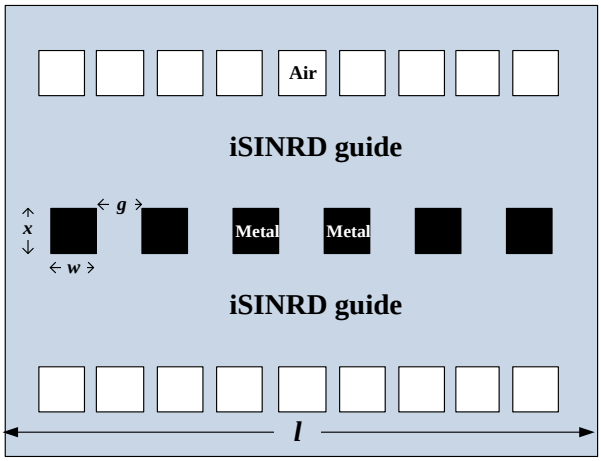

Figure 3-3: A schematic top-view of the Type A iSINRD directional coupler.

To better visualize this relationship, a set of parametric curves of the insertion loss and coupling level as a function of the number of vias are shown in Figure 3-4 for the specific frequency of 94 GHz. The periodic fluctuation of the coupling level as a function of *nvia* is evident, especially for larger values of *g*; as expected. For 3-dB coupling, five combinations of *g* and *nvia* are possible. In addition to the criteria set in the previous paragraph, the value of *nvia* must of course be an integer number. The optimum choice is thus $g/\lambda_g = 0.254$ and *nvia* = 6. Together with the values of *x* and *w* size mentioned above and the lateral dimension of the

iSINRD guide from Chapter 1, the coupler is simulated using [51]. The simulation results are shown in Figure 3-5, while the phase diagram is shown in Figure 3-6. The field plots are shown in Figure 3-7. The coupler dimensions are tabulated in Table 3.1.

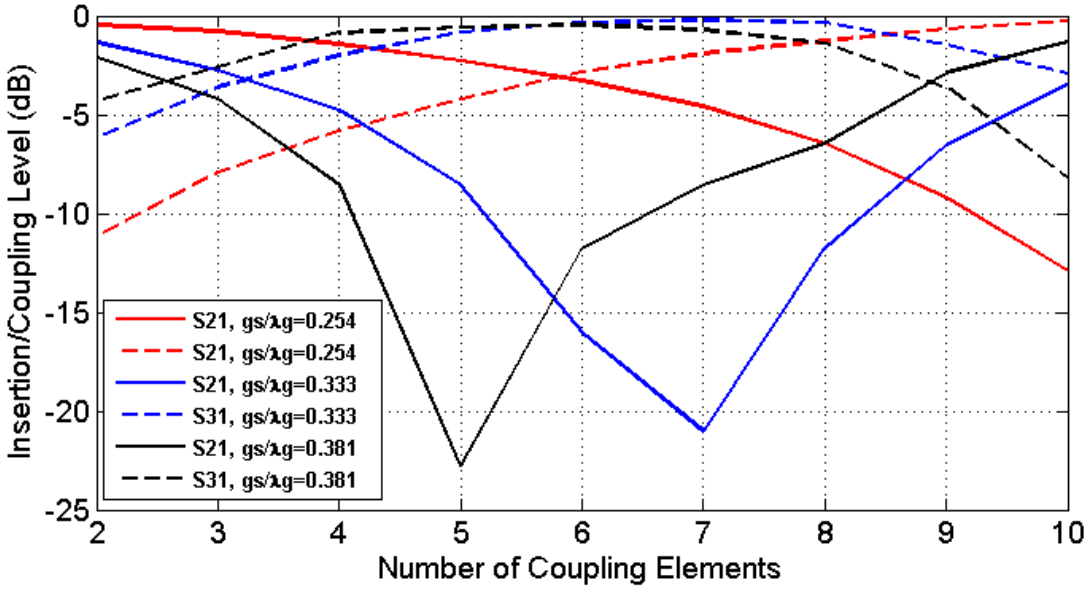

Figure 3-4: Coupling level, in dB, as a function of the number of coupling vias.

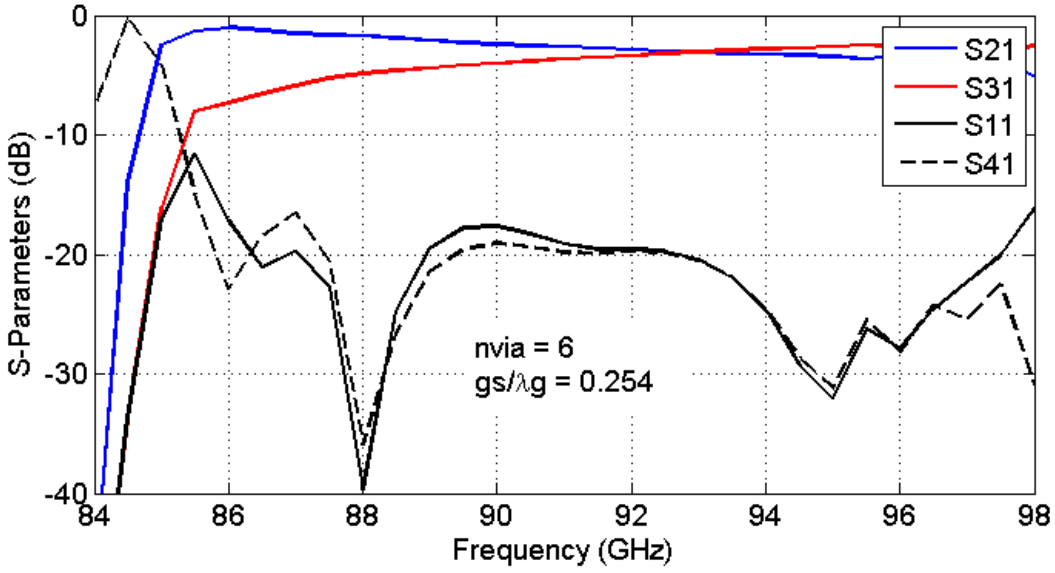

Figure 3-5: Simulated S-Parameters of the Type A iSINRD directional.

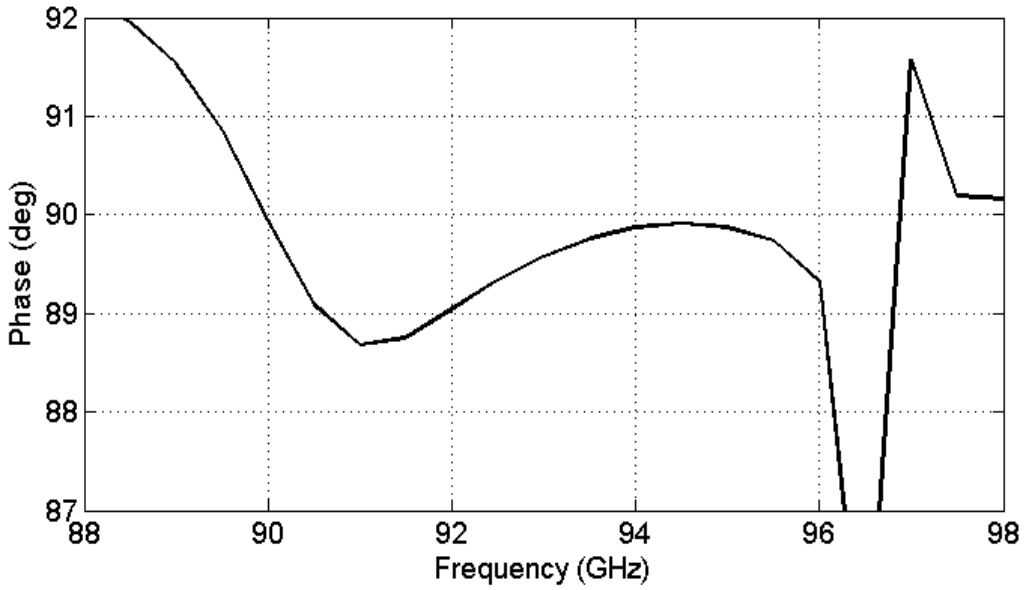

Figure 3-6: The phase imbalance with respect to frequency of the Type A iSINRD directional coupler.

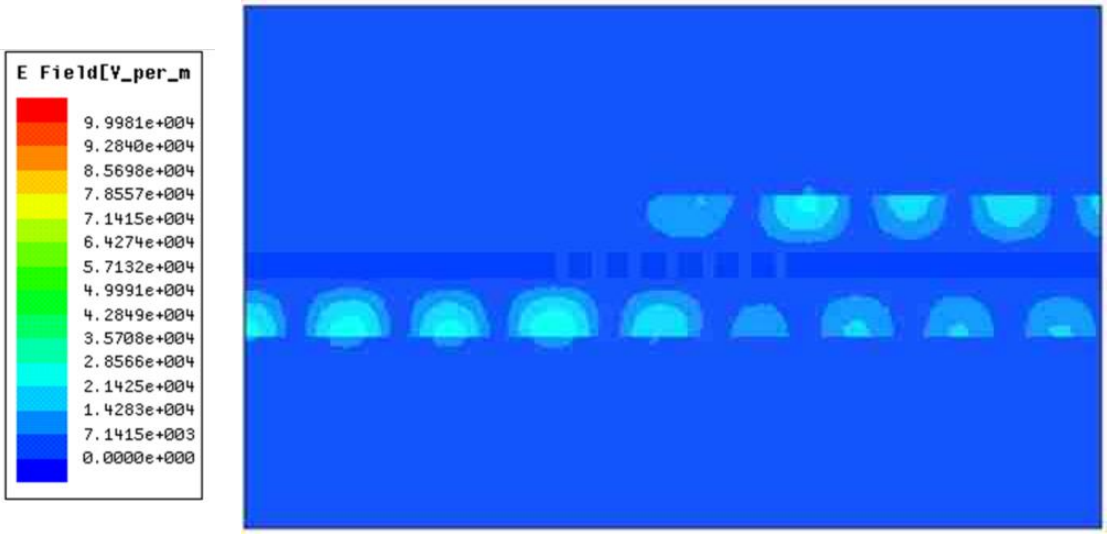

Figure 3-7: A top view plot of the E-field of the LSM_{10} mode in a Type A iSINRD directional coupler.

Table 3.1: Key dimensions of the iSINRD directional forward couplers

Symbol	Quantity	Value
a	Thickness of the iSINRD guide	0.635 λ_g
b_i	Width of the iSINRD guide	0.413 λ_g
x	Width of the coupling section	0.254 λ_g
w	Longitudinal dimension of metal via	0.254 λ_g
$nvia$	Number of coupling vias	6
g	Space between air vias	0.254 λ_g
ε_r	Permittivity of Alumina	9.8

3.2.2 Type B Coupler

3.2.2.1 Operation with the LSM_{10} Mode

In the conventional iSINRD guide design, the air side is typically realized by at least two rows of air vias, with the gaps between the vias kept to a minimum to prevent mode leakage into the air side region. Conversely, if only one row of air vias is used, and the gaps between the vias are increased, leakage into the air region occurs. While this is typically unwelcome, it can be positively utilized in numerous fashions, one of which is discussed in this subsection. Specifically, if an iSINRD guide is mirrored about the air-vias row, one obtains the structure shown in Figure 3-8, which is simply two parallel iSINRD guides that share their (discontinuous) air regions. Mode leakage is thus expected into the other guide. The identical boundary conditions would then duplicate the mode in guide 2; similar in fashion to type A. It is important to note, however, that, while the Type A structure collectively resembles an SINRD guide, the Type 2 structure does not. Rather, it resembles a rectangular waveguide that supports the TE_{21} mode. This explains the duplication of the LSM_{10} guide into the other guide, since the TE_{11} is

identical to two iSINRD LSM_{10} modes "connected" from their exponentially decaying end, as shown in Figure 3-9.

While the air vias are not responsible for conductor losses, deviating from the dimensional criteria of the Type A coupler consequently leads to a longer coupling section, corresponding to more metallic contact with the side as well as top and bottom ground planes. Therefore, the size of the air vias is again chosen to be $x/\lambda_g = w\ \lambda_g = 0.254$. The optimum values for g and $nvia$ are then 0.254 and 6, respectively; obtained from Figure 3-10. The simulated S-Parameters and phase diagram are shown in Figure 3-11 and Figure 3-12 respectively. The field plots plot of this coupler is shown in Figure 3-13.

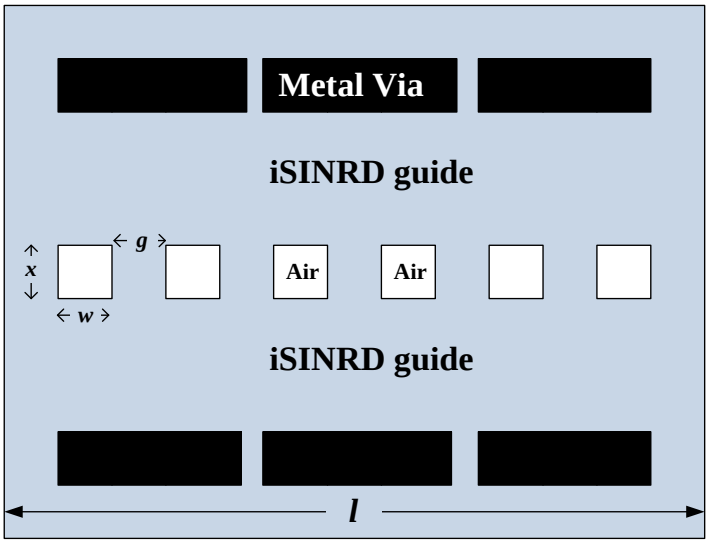

Figure 3-8: A schematic top-view of the Type B iSINRD directional coupler.

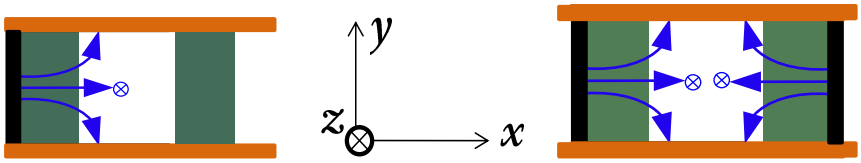

Figure 3-9: The E-fields of the LSM_{10} (left) and the TE_{11} (right) modes.

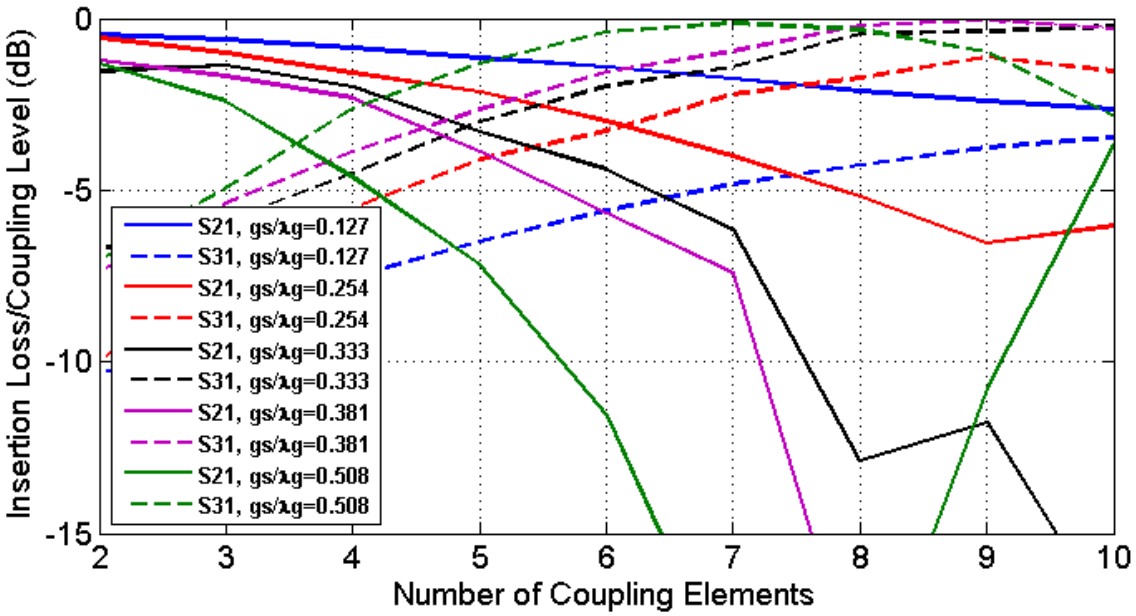

Figure 3-10: Coupling level, in dB, as a function of the number of coupling vias at 94 GHz.

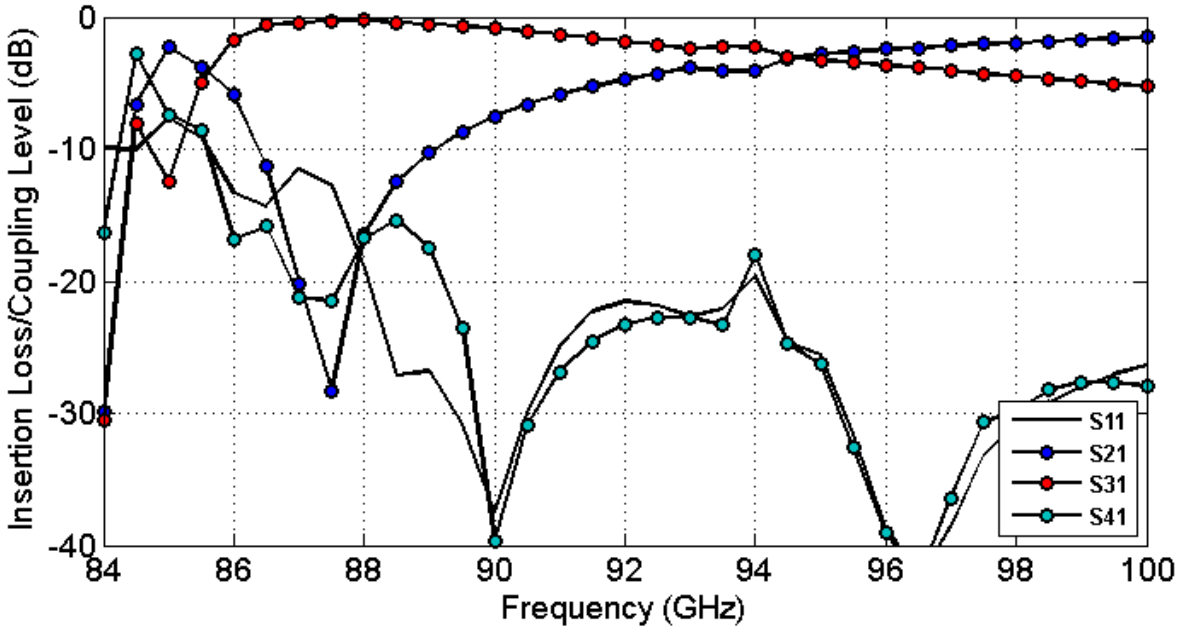

Figure 3-11: The simulated S-Parameters of the Type B iSINRD directional (LSM_{10} operation).

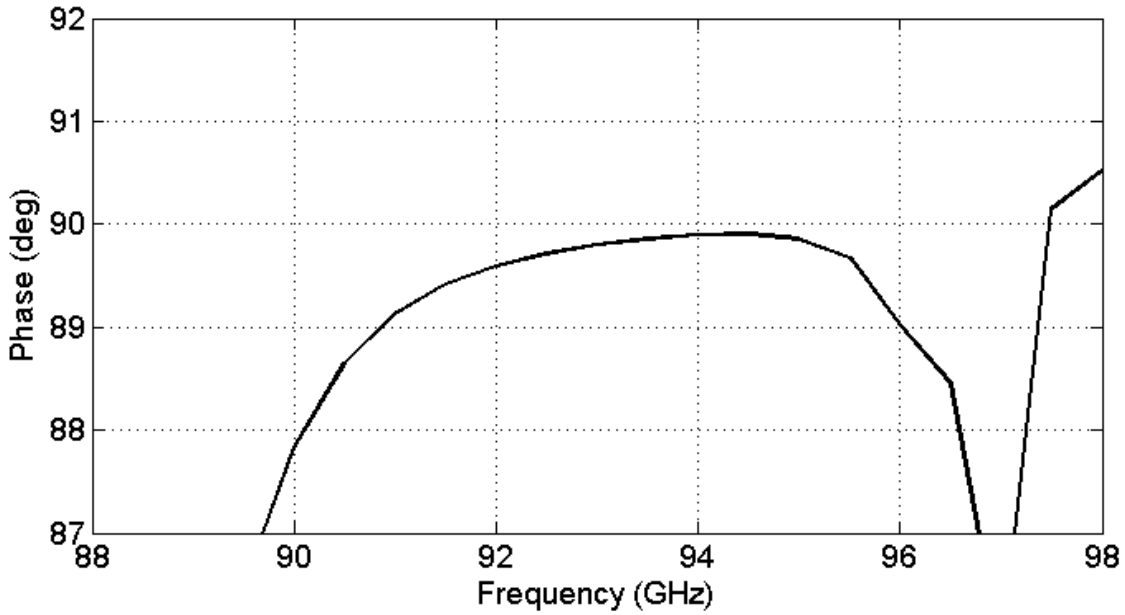

Figure 3-12: The phase variation with respect to frequency of the LSM_{10} Type B iSINRD directional coupler.

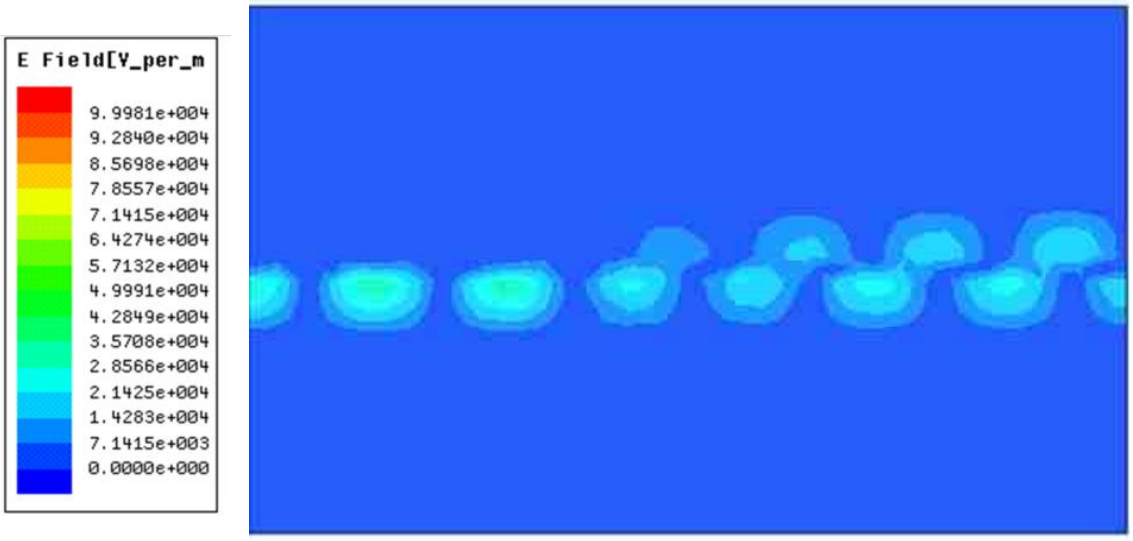

Figure 3-13: A top view plot of the E-field of the LSM_{10} mode in a Type B iSINRD directional coupler.

3.2.2.2 Operation with the TE_{10} Mode

The Type B coupler can also be operated with the TE_{20} mode at 94 GHz. This is confirmed by the parametric curves in Figure 3-14 obtained for the TE_{20} mode. The simulated response and phase difference between the output ports are shown in Figure 3-15 and Figure 3-16, respectively.

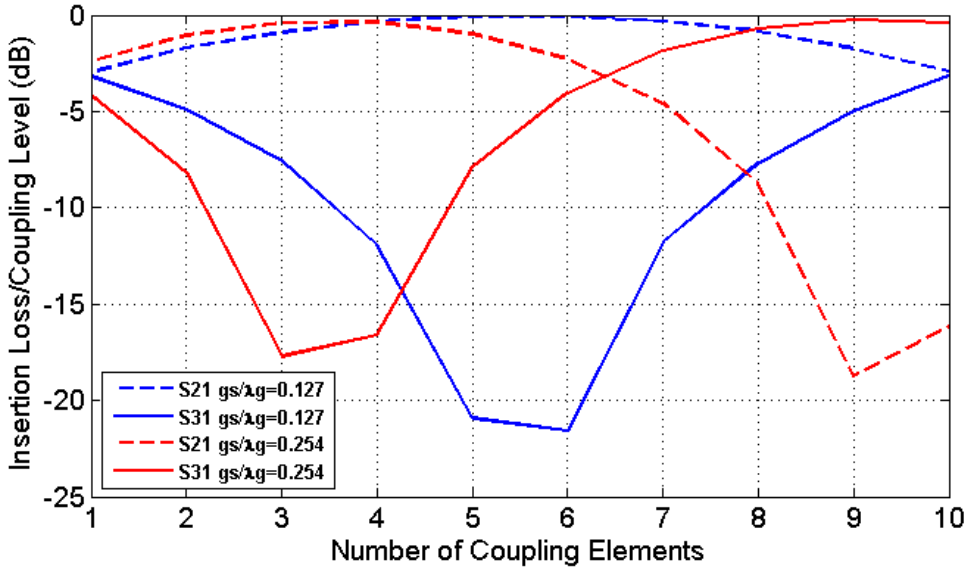

Figure 3-14: Coupling level, in dB, as a function of the number of coupling vias at 94 GHz (TE_{20} operation).

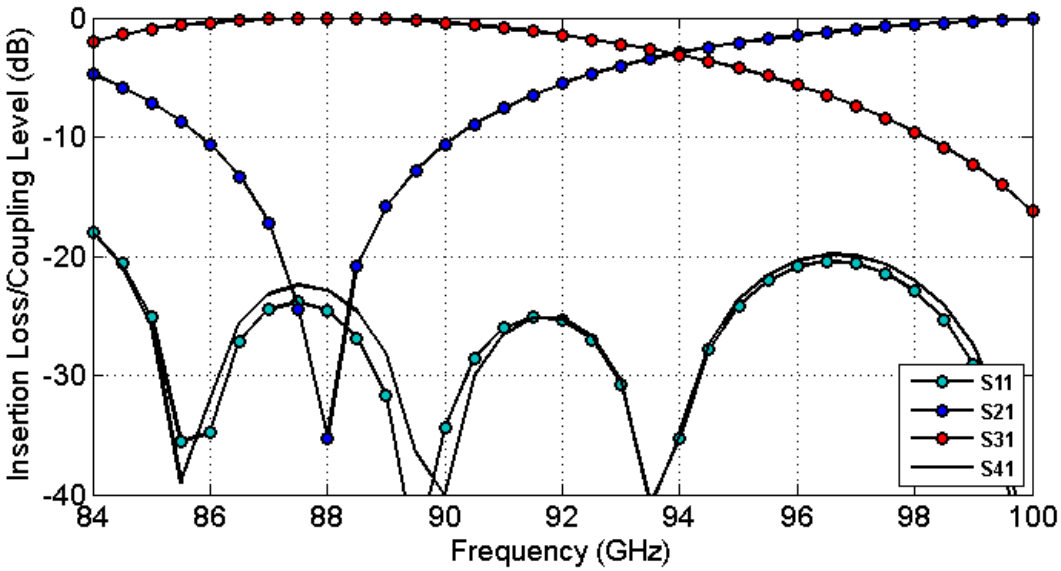

Figure 3-15: The simulated S-Parameters of the Type B iSINRD directional (TE_{20} operation).

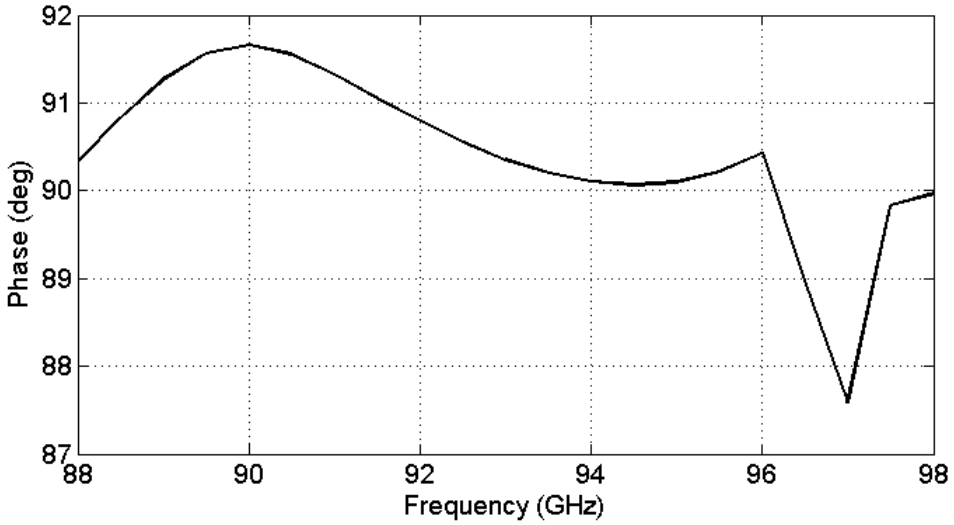

Figure 3-16: Phase variation with respect to frequency of the TE_{20} Type B iSINRD directional coupler.

3.2.3 Dual-mode iSINRD Cross-Over Structure

The LSM_{10} and TE_{20} S-parameter curves for the Type B coupler reveal an interesting dual band property. That is, besides the 3-dB performance at 94 GHz, the same structure can likewise be operated as a 0-dB coupler at 88 GHz. Indeed, this fact is reflected in Figure 3-17, which depicts the relationship between the coupling level and the number of coupling.

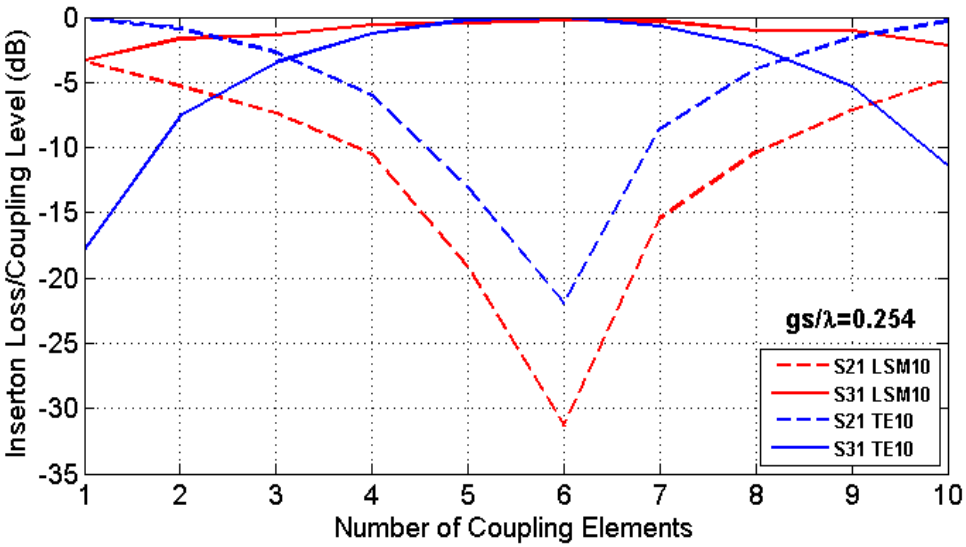

Figure 3-17: Coupling level, in dB, as a function of the number of coupling vias at 88 GHz.

The interesting fact about the latter structure is that it can be operated in dual mode configuration, with the LSM_{10} and TE_{20} modes being fed to the input ports (one mode for each port). The result is that each mode is collected at the diagonally opposite port; thus the name crossover. The simulation results for this structure are shown in Figure 3-11 and Figure 3-15 above, for the LSM_{10} and TE_{20} mode, respectively.

3.3 The iSINRD-iSIW Asymmetric Directional Coupler

Asymmetric directional coupling occurs between two parallel but different waveguides. Many such couplers have been reported in the literature [70–72], and in the context of the SICs technology, a continuous single layer CPW-SIW hybrid asymmetric coupler was investigated in [69]. To avoid the limitations at the W-band (see Chapter 1), an iSINRD alternative must be sought. In this section, the design of a discontinuous iSINRD-iSIW asymmetrical coupler is outlined. A top-view sketch of the proposed coupler is shown in Figure 3-18. The "i" prefix next to the SIW stands for "inverted", and the reason behind this nomenclature will be explained shortly.

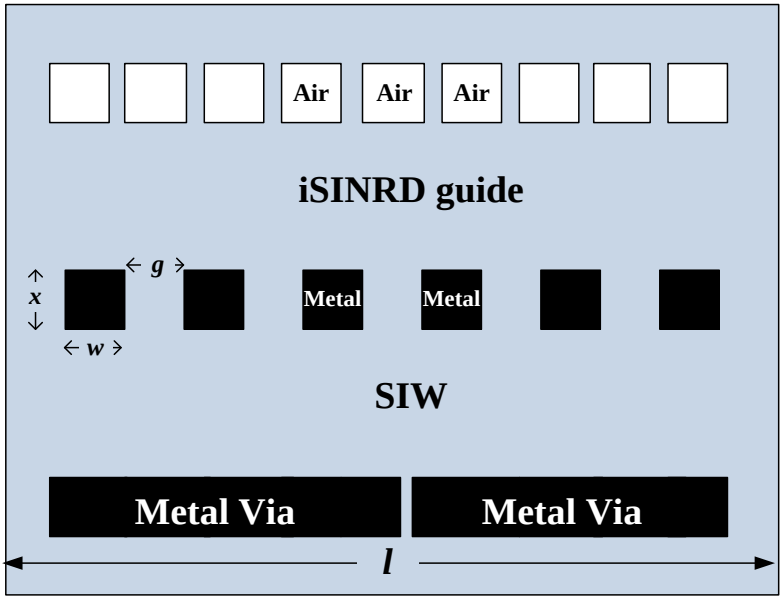

Figure 3-18: A schematic top-view of the iSINRD-iSIW directional coupler.

3.3.1 Principle of Operation

Although the conventional rectangular waveguide may be designed to operate in modes other than the TE_{10} mode, no SIW circuit is ever reported to operate in a mode other than the TE_{10} mode. In fact, as a matter of principle, the SIW channel width is required to be at least twice that of the height (substrate thickness), thus maximizing the bandwidth of the TE_{10} mode by shifting the cut-off frequencies of many higher order modes to higher values, as well as suppressing the degenerate TE_{01} mode [73], [74]. This design principle, however, need not be strictly obeyed, and deviating from it may lead to some interesting applications. One such application is the single-layer iSINRD-iSIW asymmetric directional coupler shown in Figure 3-18.

To have the two waveguides in the same layer, they ought to be of the same height, as the height of Alumina substrates cannot be tapered [63]. Two problems immediately arise. The first problem is the design principle of the SIW, which requires the height to be twice the width. If one is to obey this rule, the cut-off frequency of the SIW TE_{20} and TE_{01} modes would then be well below that of the LSM_{10} mode. In other words, susceptibility to mode conversion is very high. The second problem is achieving the desired LSM_{10}-TE_{10} mode conversion in the first place. If the iSINRD guide is fed with the LSM_{10} mode, leakage would occur from the gaps in the metal-via row. Since the LSM_{10} mode has a dominantly horizontal sense in the vicinity of the metal wall region, it cannot simply convert to the vertical TE_{10} mode in the SIW; unless some discontinuity is introduced in the SIW, which is not feasible with the Alumina ceramic substrate [63]. Even if it were, it would complicate the design substantially, given the minute dimensions of such discontinuities at W-band frequencies.

To mitigate these short-comings, a deviation from the standard SIW design is proposed, in which the lateral dimensions of the SIW are interchanged. Specifically, the width of the SIW is made smaller than its height. In other words, the SIW is "inverted"; and thus the abbreviation "iSIW" proposed at the beginning of this section. Consequently, the TE_{01} mode is rendered the fundamental mode, while the TE_{10} mode becomes a higher order mode. Hence, instead of seeking to convert the horizontal LSM_{10} mode to the vertical TE_{10} mode, it will naturally convert to the horizontal TE_{01} mode since it also possesses horizontal polarization. One must note, however, that such mode designation is relative to the way one defines the vertical and horizontal axes. Otherwise, the TE_{10} and TE_{01} modes are identical. This argument is illustrated in Figure 3-19.

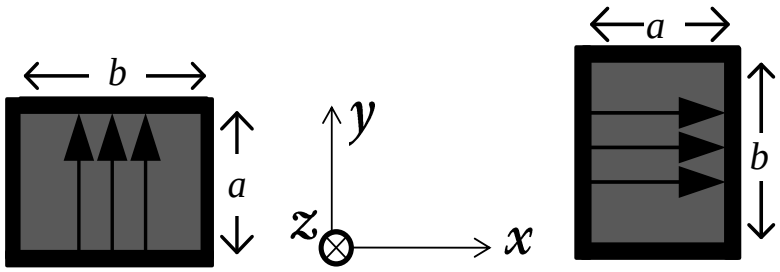

Figure 3-19: A cross-sectional front-view of the electric field lines of the TE_{10} (left) and TE_{01} (right) modes in the SIW.

3.3.2 Parametric Study

Following the same argument for the symmetric iSINRD directional couplers, via size in this iSINRD-iSIW coupler is again chosen to be $0.254\lambda_g \times 0.254\lambda_g$. The other parameters are then chosen with the aid of a set of parametric curves that were obtained using [51] and are shown in Figure 3-20. In addition to being smaller in value than the height, the width of the iSIW guide is chosen to be identical to the width of the iSINRD guide. This saves fabrication time and effort as then only one WR10 transitional cavity needs to be manufactured and thus it can be used for all the directional couplers discussed in this chapter. The corresponding S-parameters and phase diagram are shown in Figure 3-21 and Figure 3-22 respectively. The field plots are shown in Figure 3-23.

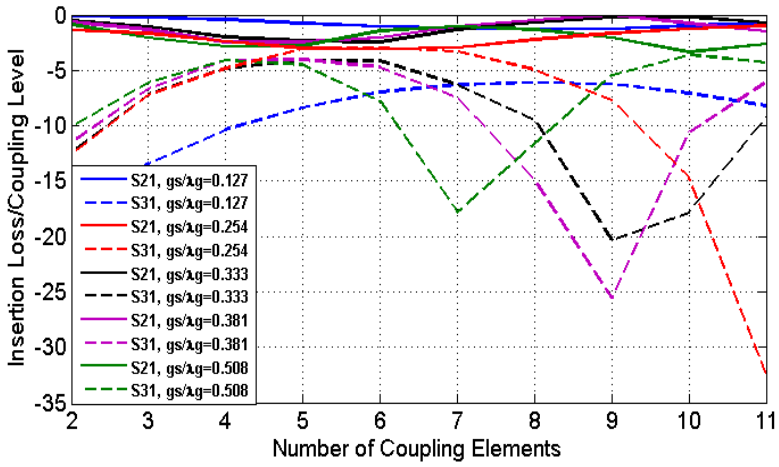

Figure 3-20: Coupling level, in dB, as a function of the number of coupling vias for the asymmetrical iSINRD-iSIW directional coupler.

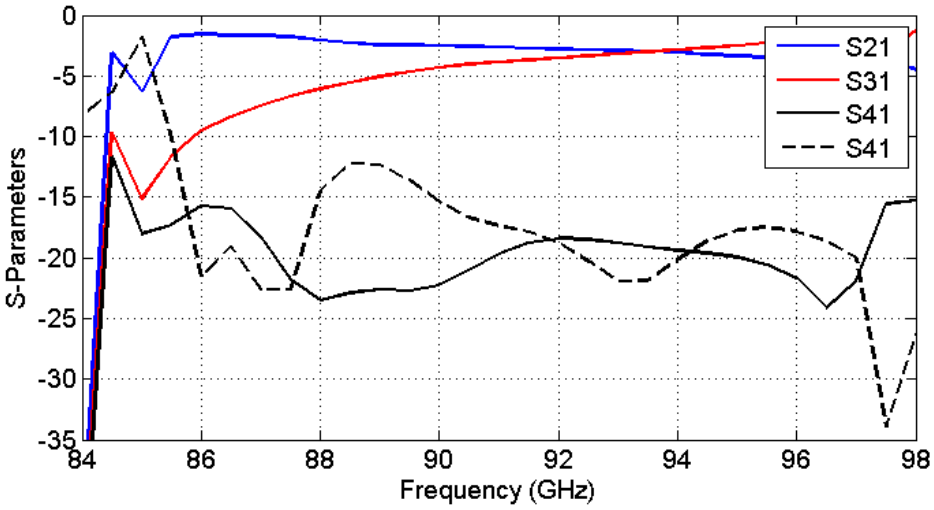

Figure 3-21: The simulated S-Parameters of the iSINRD-iSIW directional coupler.

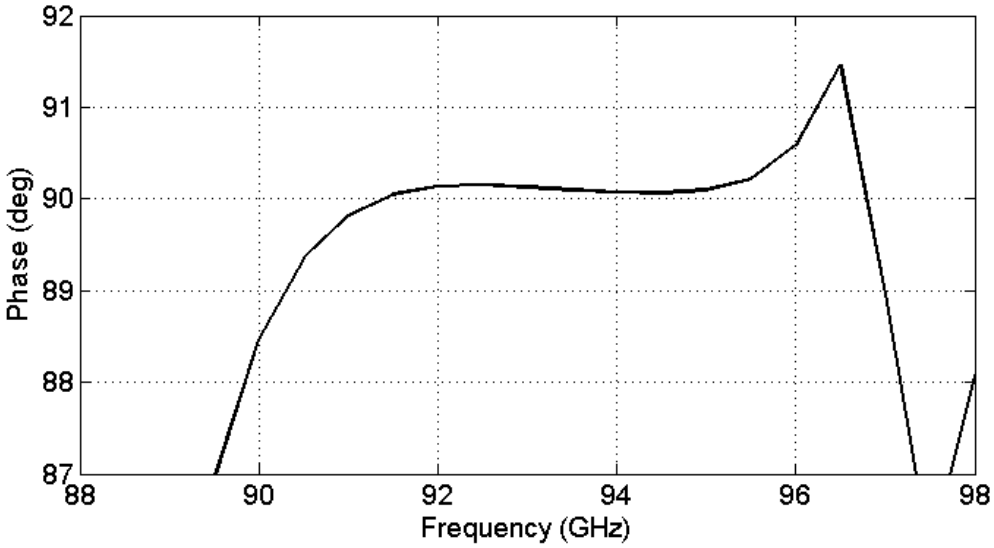

Figure 3-22: Phase variation with respect to frequency of the asymmetrical iSINRD-iSIW directional coupler.

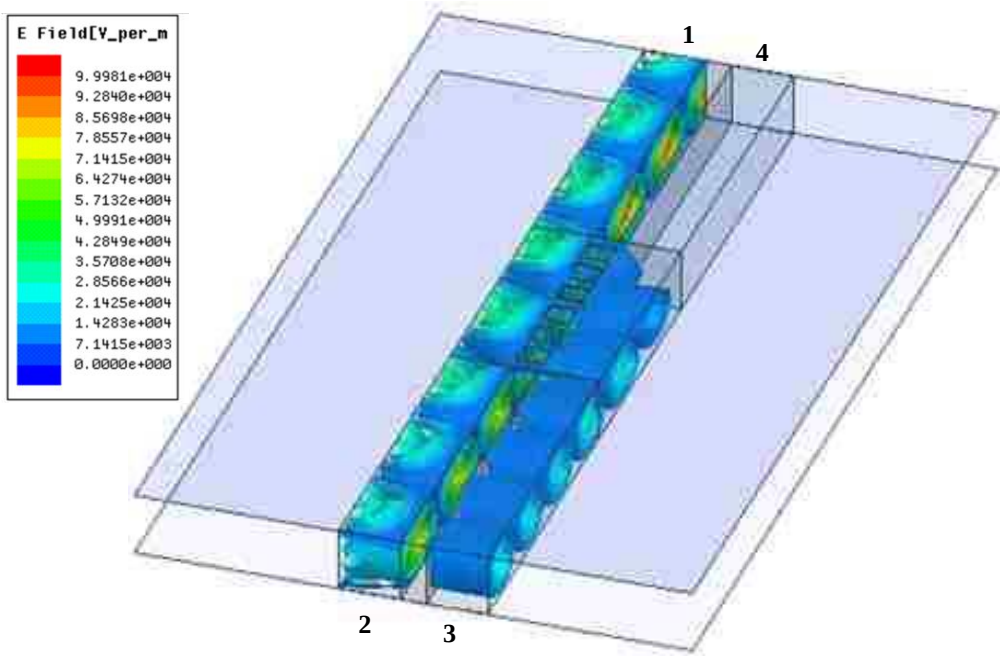

Figure 3-23: A 3-D filed plot of the LSM_{10} mode in an asymmetrical iSINRD-iSIW directional coupler.

3.4 A 180^o Hybrid Based on the iSINRD Directional Coupler

Central to the design of many microwave circuits, especially mixers and six-port networks, is the 180^o hybrid. The 180^o hybrid is simply a 90^o hybrid with the two outputs being of different lengths (or characteristics) to enforce an 180^o between them. Thus a length difference of quarter wavelength is considered.

The directional couplers discussed thus far provide an excellent means to realizing a W-band iSINRD 180^o hybrid. To avoid redundancy, only Type B 180^o hybrid is considered here. Extending the length of one of the outputs of the coupler, by a quarter wavelength, yields an 180^o (or 0^o) phase difference between the output ports relative to port 1 (or port 4); and thus an 180^o hybrid. The principle of operation is otherwise identical to the 90^o directional hybrid. A sketch of the proposed 180^o hybrid, based on the Type B geometry is shown in Figure 2-17. With the dimensions from subsection 2.1.2, and with $\Delta l = \lambda_g/4$, the simulated results for the in-phase and out-of-phase S-parameters are identical to those in Figure 3-11. The phase imbalance is shown in Figure 3-25.

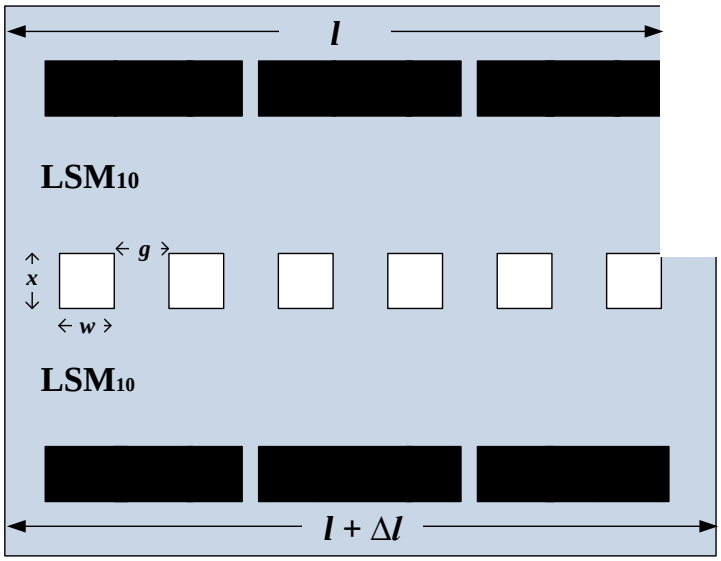

Figure 3-24: Top view of a Type B 180^{o} hybrid based on the iSINRD guide Type B directional coupler.

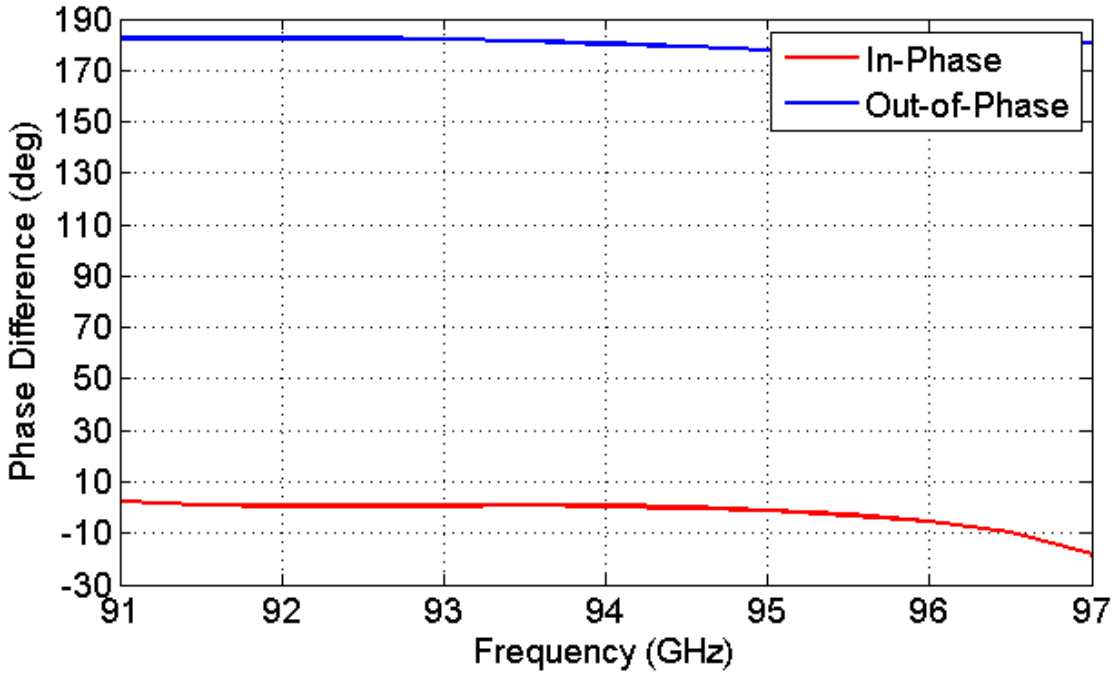

Figure 3-25: Phase variation with respect to frequency of an iSINRD guide 3-dB 180^{o} hybrid.

3.5 Experimental Results and Discussion

All the circuits discussed in the previous sections were fabricated using a polished Alumina ceramic substrate. The couplers are excited using the tapered transition to WR10 mentioned in Chapter 2. The transitions include the 90^o bends (Case I and II) discussed in chapter 2. Therefore, a standard TRL de-embedding procedure was performed so that the measured response includes only the coupling section. The fabricated couplers are shown in Figure 3-26 to Figure 3-30 .The Type B iSINRD coupler had to be fabricated twice since the inputs of the LSM_{10} and TE_{20} modes are orthogonal. This means that the excitation of each mode requires the fabrication of a distinct aluminum cavity (notice the difference in width between the feeding aluminum cavity in Figure 3-27 for the LSM_{10} mode and that shown in Figure 3-28 for the TE_{20} mode). Measurements were made separately for the LSM_{10} and TE_{20} modes due to the VNA being limited to two ports only. That is, one input and one output ports were connected to the VNA at the same time. Thus, WR10 loads were used to match the other ports. In Figure 3-30, the difference between the top two arms is evident, which accounts for the the out-of-phase coupling.

The measured S-parameters for the above fabricated circuits are shown in Figure 3-31 through Figure 3-37 respectively; together with the simulation results. The simulation results shown in those figures include the dielectric and conductor losses. In all of the presented plots, return loss is measured to be higher than the simulated one, which is due to the reflections from air vias and the inevitable fabrication tolerance errors in dimensions of the coupling vias between the waveguides. In general, however, the measurement results are in satisfactory agreement with the simulation, with reflection and isolation being better than 15-dB at 94 GHz, for all the presented circuits. For the 3-dB couplers and 180^o hybrid, a coupling level better than 4-dB is obtained. As for the LSM_{10} mode cross-over coupling operation at 88 GHz, a coupling level of 1-dB is measured, while the reflection, isolation and insertion loss of more than 15 dB is obtained (Figure 3-32). For the TE_{20} mode cross-over coupling operation at 88 GHz, however, one observes a shift in the operating frequency, which is easier to see from the S21 curve (Figure 3-33). This shift is owed to the fact that the exact positioning inside the aluminum cavity of the Type B coupler for TE_{20} operation is more difficult given the larger width of the feeding WR10 transition. Consequently, the error margin for this transition is broader, which is manifested by the shift in frequency and stronger ripples. Finally, the phase diagrams of the 180o hybrid, shown in Figure 3-36 and Figure 3-37, indicate good agreement between measurement

and simulation, except that the phase is conserved over a smaller bandwidth compared to simulation. This is attributed to the fact that length of the tapered substrate section of the extended arm is longer inside the WR10 waveguide compared to the other arms which may lead to difference in phase behavior for certain frequencies.

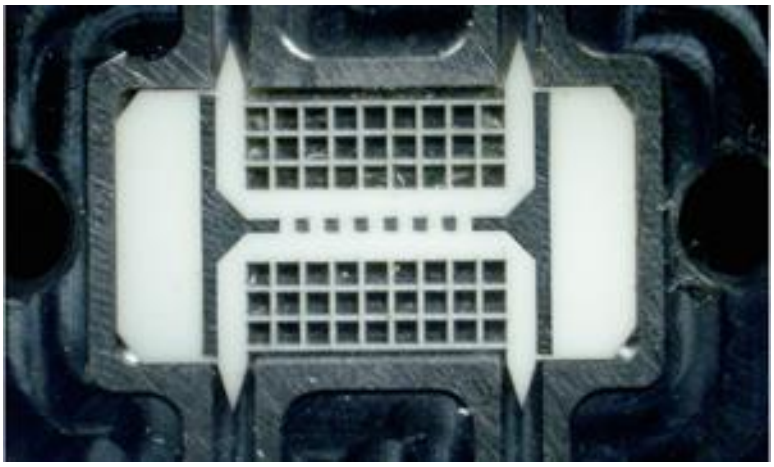

Figure 3-26: Top view of a fabricated Type A iSINRD directional coupler.

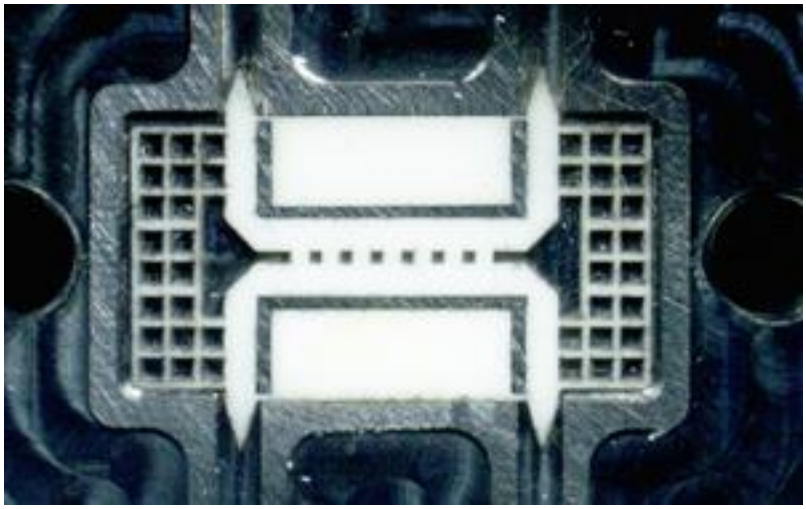

Figure 3-27: Top view of a fabricated Type B iSINRD coupler (LSM_{10} operation).

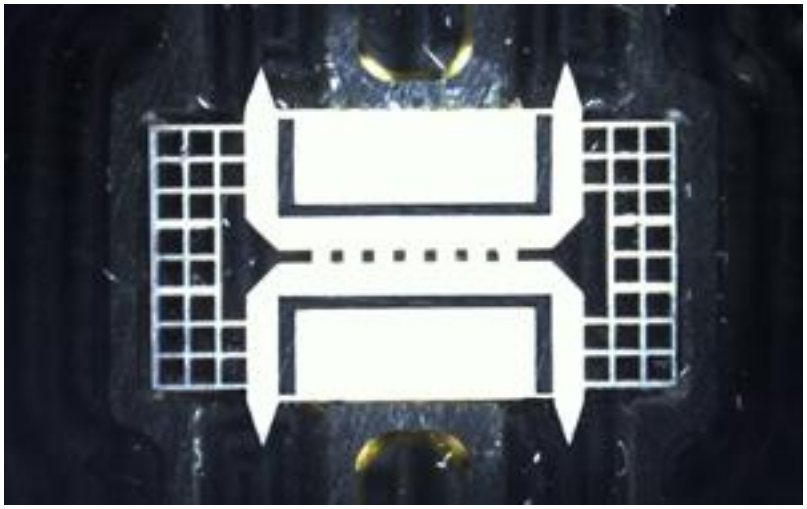

Figure 3-28: Top view of a fabricated Type B iSINRD coupler (TE_{20} operation).

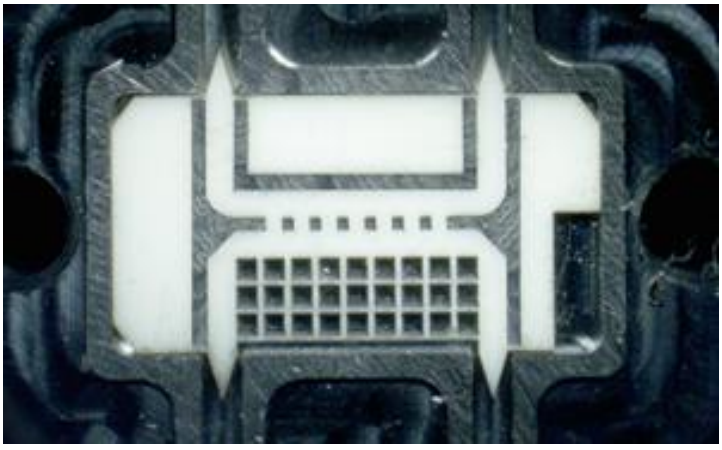

Figure 3-29: Top view of a fabricated iSINRD-iSIW asymmetrical directional coupler.

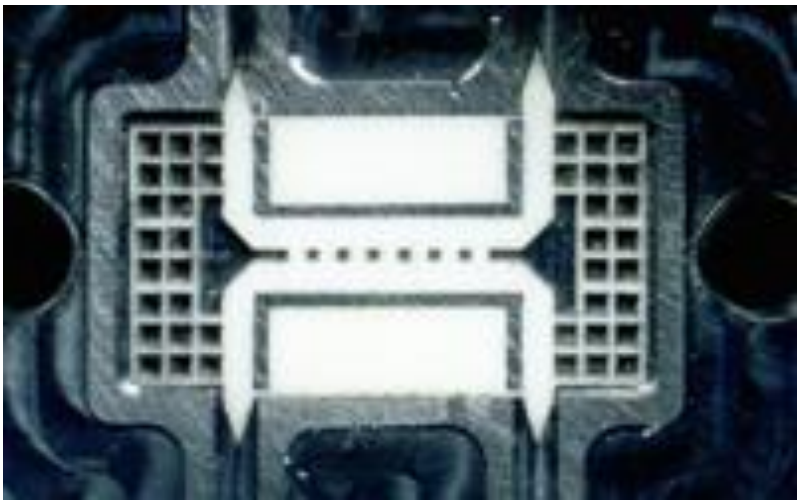

Figure 3-30: Top view of a fabricated iSINRD 180^{o} hybrid.

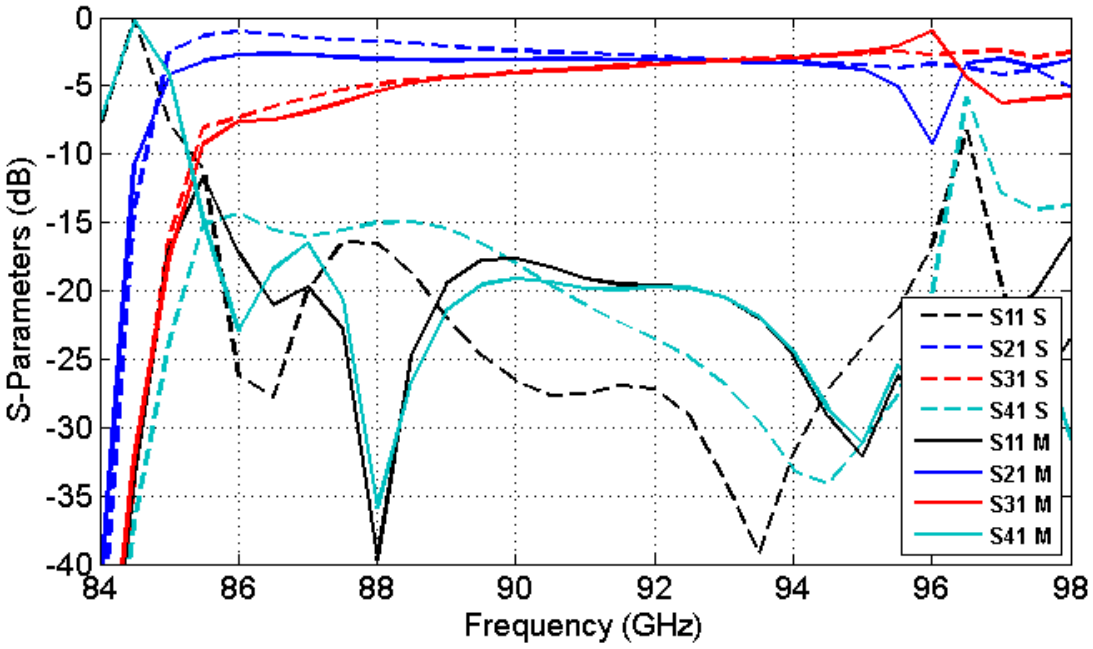

Figure 3-31: Simulated (S) and measured (M) S-parameters of the iSINRD Type A coupler (LSM_{10} operation).

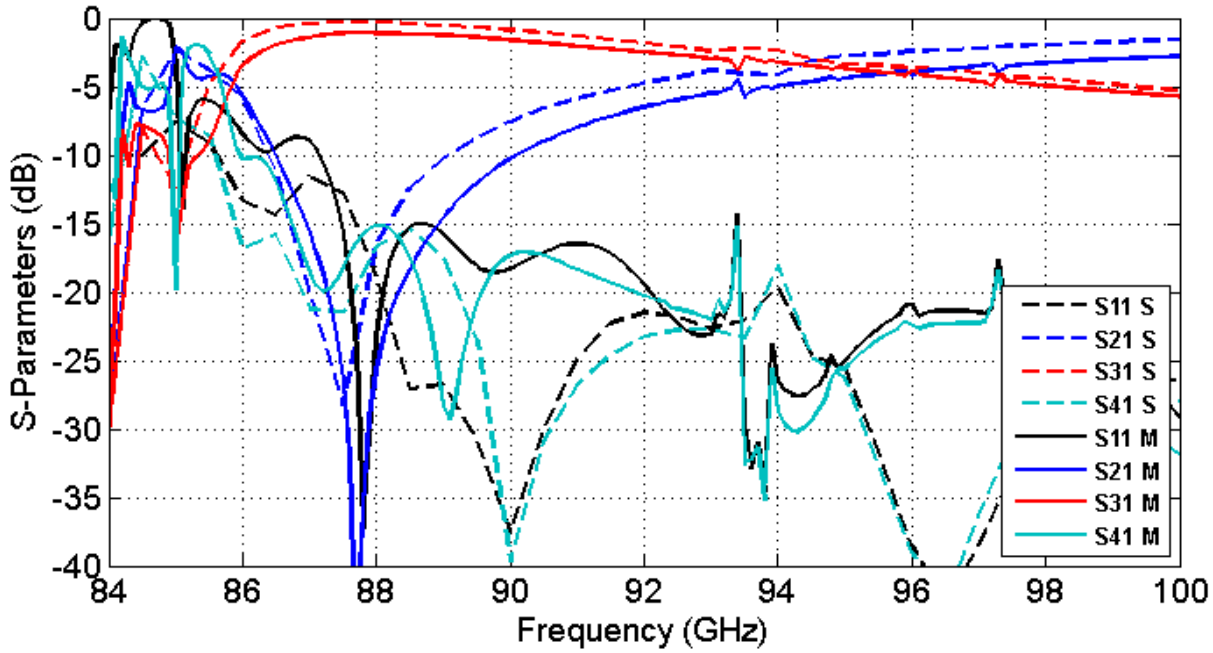

Figure 3-32: Simulated (S) and measured (M) S-parameters of the LSM_{10} mode Type B iSINRD coupler, including the 88 GHz cross-over coupler.

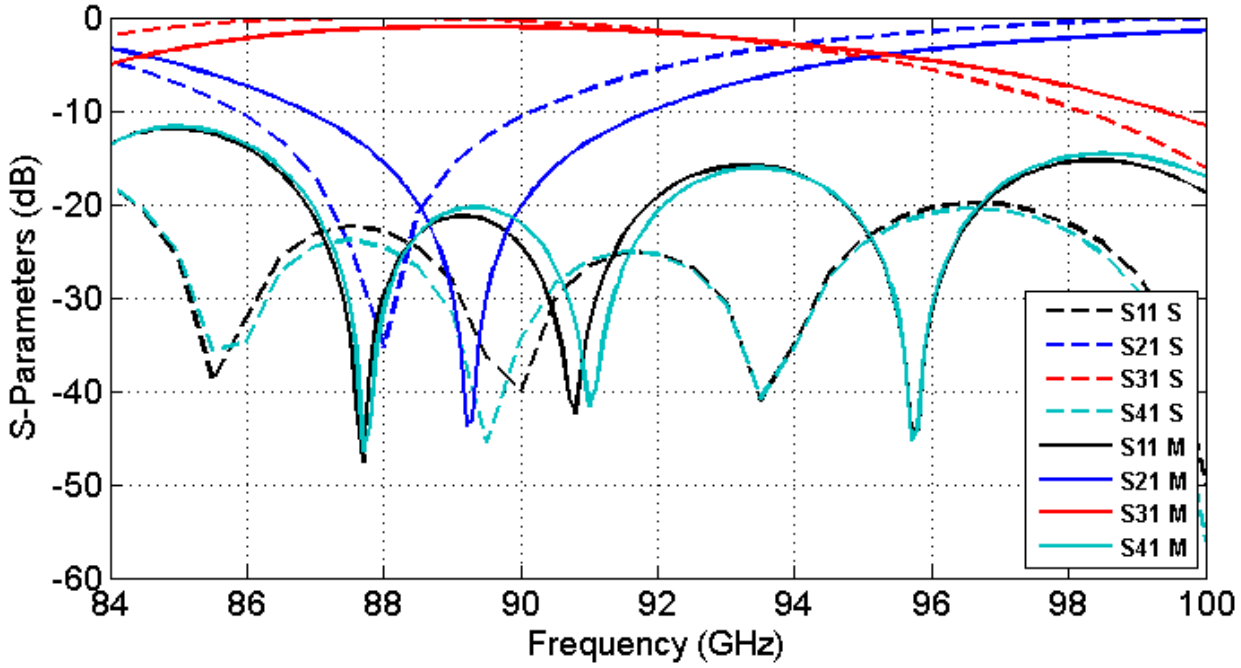

Figure 3-33: Simulated (S) and measured (M) S-parameters of the TE_{20} mode Type B iSINRD coupler, including the 88 GHz cross-over coupling.

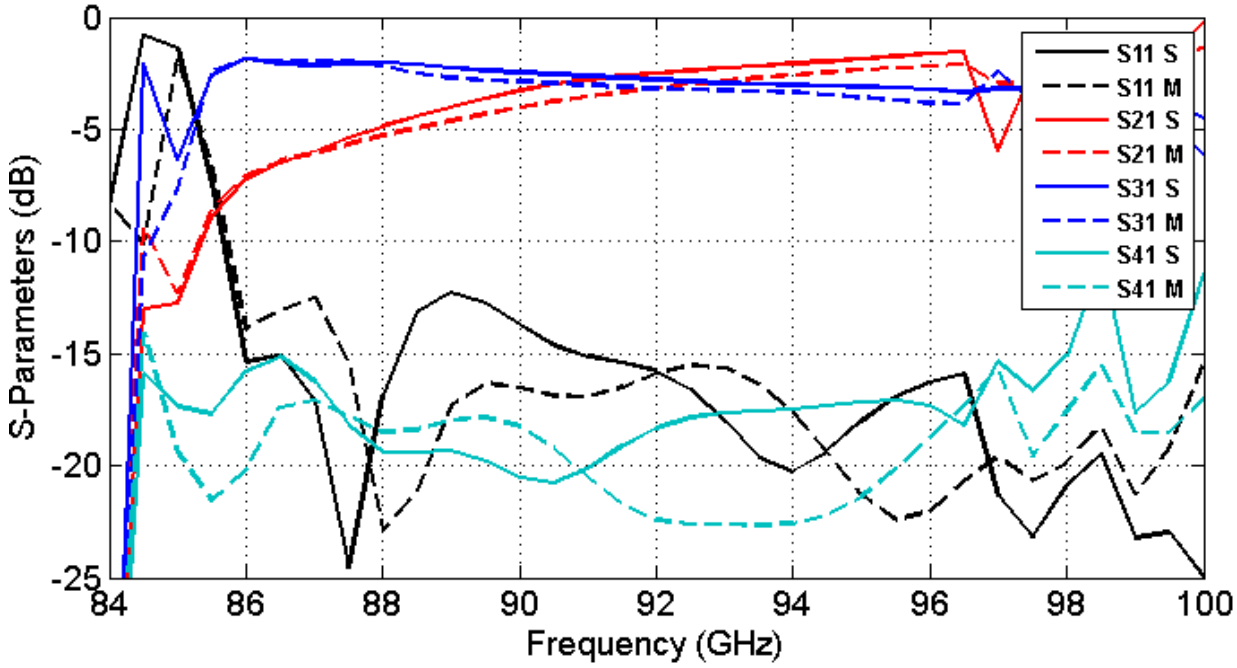

Figure 3-34: Simulated (S) and measured (M) S-parameters of the asymmetric iSINRD-iSIW coupler, including the cross-over coupler (TE_{20} operation).

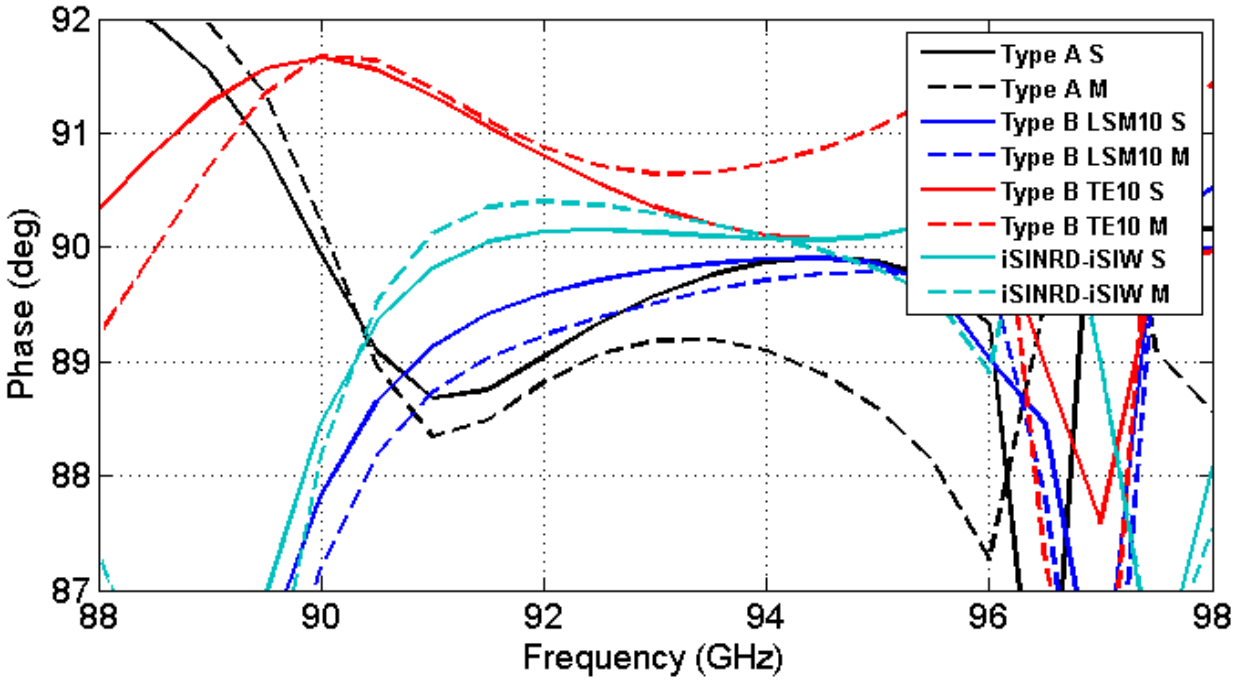

Figure 3-35: Simulated (S) and measured (M) phase imbalance of the four different iSINRD 3-dB directional couplers.

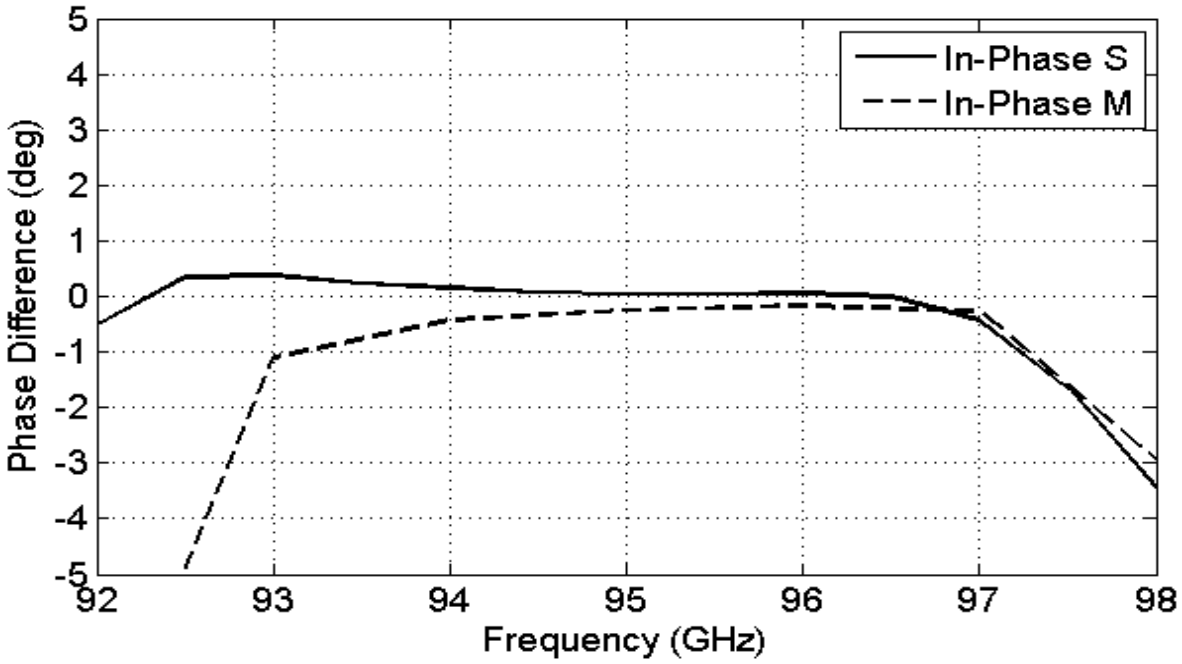

Figure 3-36: Simulated (S) and measured (M) phase imbalance of the in-phase operation of the iSINRD 3-dB 180^0 hybrid.

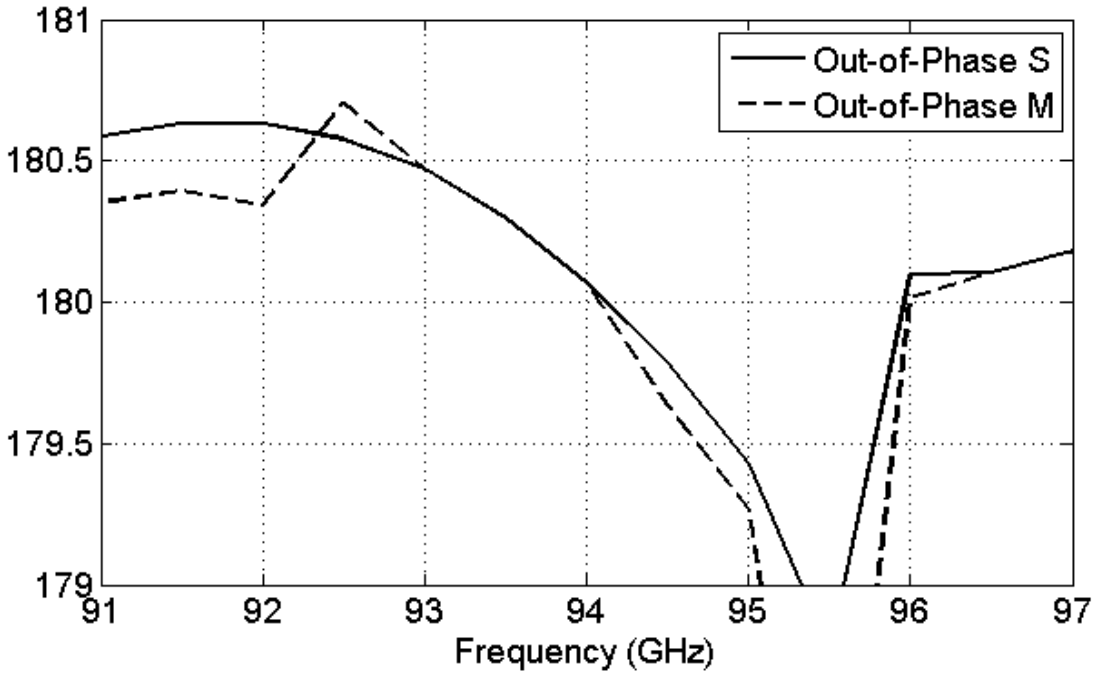

Figure 3-37: Simulated (S) and measured (M) phase imbalance of the out-of-phase operation of the iSINRD 3-dB 180^0 hybrid.

Chapter 4 THE iSINRD GUIDE IN THE CONTEXT OF CRUCIFORM CIRCUITS

4.1 Introduction

Although the directional couplers discussed in Chapter 3 lend themselves to many applications, their main drawback lies in their complicated design. This is manifested by the fact that the coupling sizes via holes as well as the spacing between them is in the order of the fabrication error.

In this chapter, a more feasible alternative to the directional couplers of Chapter 3 is analyzed and discussed. The basis of this alternative approach is the theory of quasi-optical cruciform couplers. Such circuits are conceived by knotting a number of individual waveguides to a common junction, thus forming a multiport junction or circuit, such as the filter reported in [75]. The S-matrix of such circuits is typically derived using even-odd analysis techniques, where the transmission and reflection coefficients of the individual arms (or guides) are superposed to obtain the scattering parameters of the junction [76], [77]. The cruciform couplers reported in literature are all based on the SIW, and require the incorporation of inductive posts or reflective mirrors to achieve the desired coupling with high isolation. As already established, this is a daunting task at 94 GHz, and work-around must be sought for a successful implementation of W-band iSINRD cruciform circuits.

In this chapter, a similar analysis of iSINRD arms is carried out with the ultimate aim of conceiving an iSINRD four-port cruciform coupler (Sections 4.2). In Section 4.3, an iSINRD magic-T is in turn derived from the iSINRD cruciform coupler. A modification of the iSINRD coupler to obtain an ortho-mode transducer (OMT) is also proposed in Section 4.4. In all cruciform circuits presented in this work, simplicity is the common denominator, since the central coupling junction (or branching region in the OMT) does not require any inductive posts, reflecting mirrors, septa, or height modification that is otherwise required in traditional design of such circuits. Rather, the desired function is achieved by exploiting the boundary conditions of the LSM_{10} and TE_{20} modes, together with a correct choice of geometry and dimensions, as shall be detailed in the subsequent sections. This further highlights the merits of the iSINRD guide.

4.2 The iSINRD Cruciform Coupler

4.2.1 Coupling Mechanism

The proposed iSINRD cruciform coupler is shown in Figure 4-1 (a). Its operation is based on the LSM_{10} mode. Isolation is guaranteed since the E_z component (depicted in Figure 4-1 (a) by the encircled × symbol) of the LSM_{10} mode must be null along the PEC image plane and maximum in the perforated/air region. This simply means that the wave entering, say, port 1 can never propagate into port 4. This also means that the wave will split equally between port 3 and port 2. For the former, where the perforated region continues, there will be no phase delay. For the latter, where perforation is interrupted in the junction, the wave will be slowed as it turns through the junction's denser dielectric. Therefore, the wave going to arm 3 leads the one heading into arm 2, which explains the 90^o offset between the two arms.

4.2.2 Even-Odd Mode Analysis

4.2.2.1 Construction of the iSINRD Arms

For faster and more accurate analysis, cruciform couplers are better investigated using even-off mode analysis technique. In this technique, the four port coupler/junction is decomposed into individual arms, whose number depends on the total input and output arms of the original junction. In the case of the proposed iSINRD cruciform coupler presented here, the coupler can be decomposed into four arms; as follows. By applying PEC and PMC boundary conditions along the symmetry line m-n, as shown in Figure 4-1 (b), one obtains the two bends discussed in Chapter 2. Each of these bends can in turn be sub-divided into two respective arms by again applying boundary conditions along the symmetry lines p-q and r-s; yielding a total of four arms (A to D). It is left to the reader to verify that rotating the diagonal line of the coupler by 90^o will yield the identical set of arms (A to D), except that the arms B and D are interchanged. Therefore, it suffices to apply the symmetry conditions across either of the coupler's diagonal lines; as the other would be redundant. For the perforation region, it can also be represented by a PMC boundary condition, as verified in the subsequent analysis.

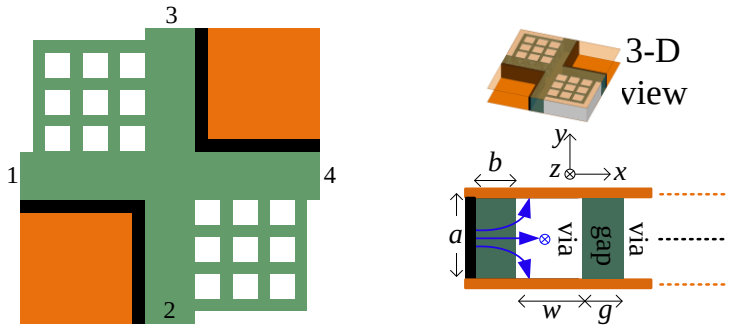

(a)

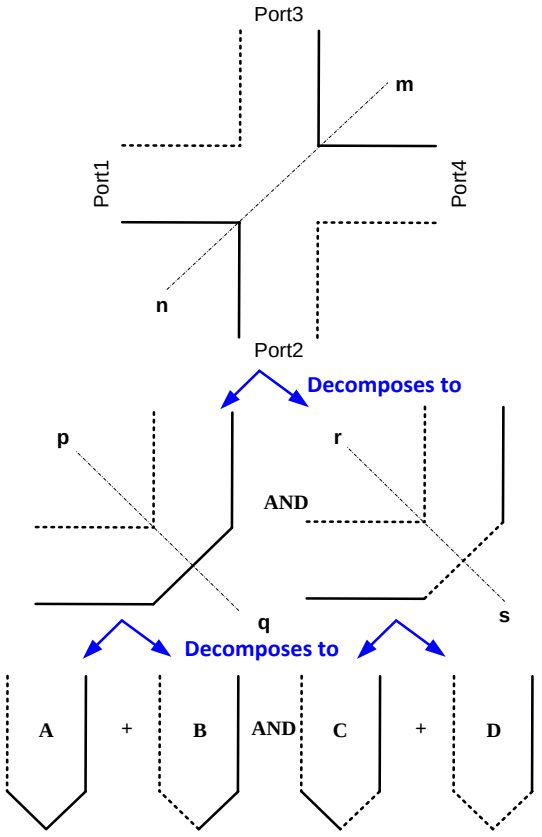

(b)

Figure 4-1: (a) Top view of the proposed iSINRD coupler (left), 3-D view of the proposed coupler (top, right) and the E-field of the LSM_{10} mode (front view, bottom right). Green: Substrate; white: air vias, black: PEC image plane; orange: metal covers. (b) Top view description of the proposed iSINRD coupler and its bend and arm decomposition. Solid: PEC; dashed: PMC.

4.2.2.2 Deriving the S-matrix

The general S-matrix of a symmetrical four port junction is given by

$$[S] = \begin{bmatrix} \tau & \chi & \kappa & \zeta \\ \chi & \tau & \zeta & \kappa \\ \kappa & \zeta & \tau & \chi \\ \zeta & \kappa & \chi & \tau \end{bmatrix} \tag{4.1}$$

The mode-matching analysis of rectangular waveguides in [76], [77] can simply be extended to the iSINRD guide to obtain the required S-matrix. The relevant reflection coefficients are thus given by:

$$\tau = \frac{1}{4}(R_A + R_B + R_C + R_D) \tag{4.2}$$

$$\chi = \frac{1}{4}(R_A - R_B - R_C + R_D) \tag{4.3}$$

$$\kappa = \frac{1}{4}(R_A + R_B - R_C - R_D) \tag{4.4}$$

$$\zeta = \frac{1}{4}(R_A - R_B + R_C - R_D) \tag{4.5}$$

The variables R_A, R_B, R_C and R_D are the reflection coefficients of the four distinct arms A, B, C and D; respectively. To obtain 3-dB symmetric coupling, the terms τ and ζ must both equal zero, while the terms χ and κ must equal $1/\sqrt{2}$ and $j/\sqrt{2}$, respectively. Consequently, for the above equations to be true, $R_A = -R_C$ and $R_B = -R_D$. This is an expected result for arms A and C since they respectively correspond to short and open circuits. This is an expected result for arms A and C since they respectively correspond to short and open circuits. This is graphically illustrated in Figure 4-2, in which the arm phase difference (A and C or B and D), at 94 GHz, is plotted as a function of the iSINRD width, *b*. In this case a phase difference of 180^o ensures the above condition. Furthermore, since $\kappa = j\chi$, $R_A + R_B = j(R_A - R_B)$, requiring that $R_A = e^{j\frac{\pi}{4}}$ and $R_B = e^{j\frac{3\pi}{4}}$; as per the phase diagram in Figure 4-3, which is a plot of the phase variation of arms A and B as a function of *b* at 94 GHz..

Care must be taken when applying the boundary conditions on the region II, illustrated in Figure 4-1 (b), of any arm. This is because, unlike the all-metal rectangular waveguide, the iSINRD guide has one side as an air region (or magnetic wall). Consequently, this (open) side is affected by all the boundary conditions in its vicinity. Therefore, applying the boundary conditions to only the geometric length of the region II, would lead to inaccuracy in the calculated scattering parameters. Similarly, the top and bottom ground planes merit a special attention. This argument is better illustrated by the substantial deviation between response in Figure 4-4 obtained with the wrong setup of Figure 4-5, and the response in Figure 4-6 obtained with the correct setup of

Figure 4-7. In both cases, the S-parameters are calculated using [62], and are compared with the ones simulated using [51]; the identical responses in Figure 4-6 validate the sanity of the above argument. The phase diagram of the coupler is shown in Figure 4-8. The field plots of the iSINRD cruciform coupler are shown in Figure 4-9.

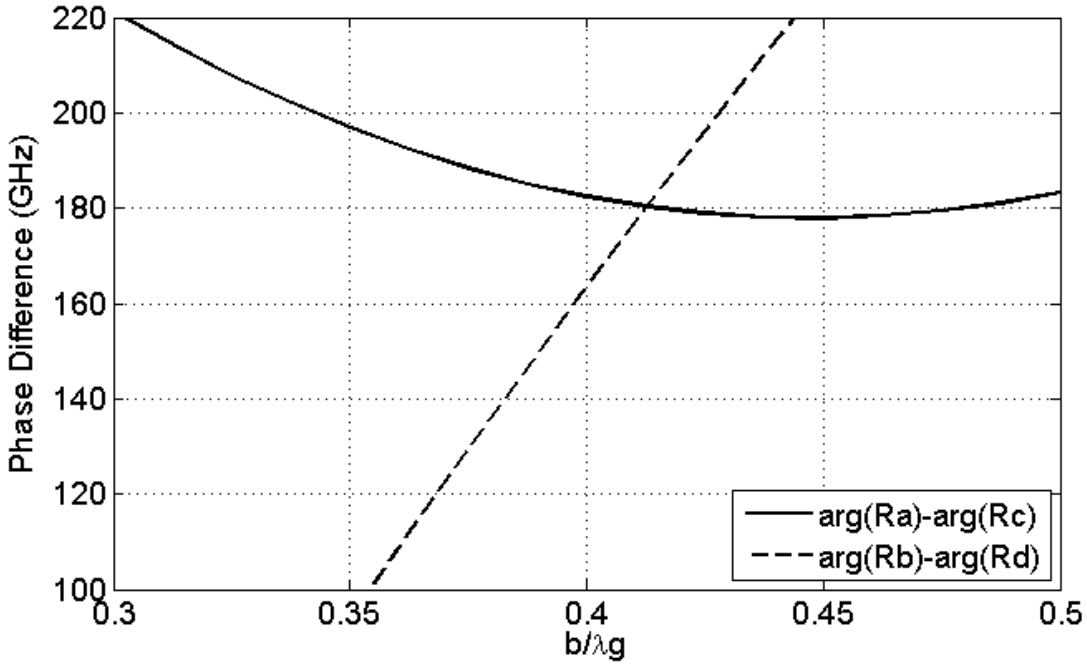

Figure 4-2: Phase difference between arms A and C, and arms B and D as a function of the iSINRD guide width, *b*, at 94 GHz.

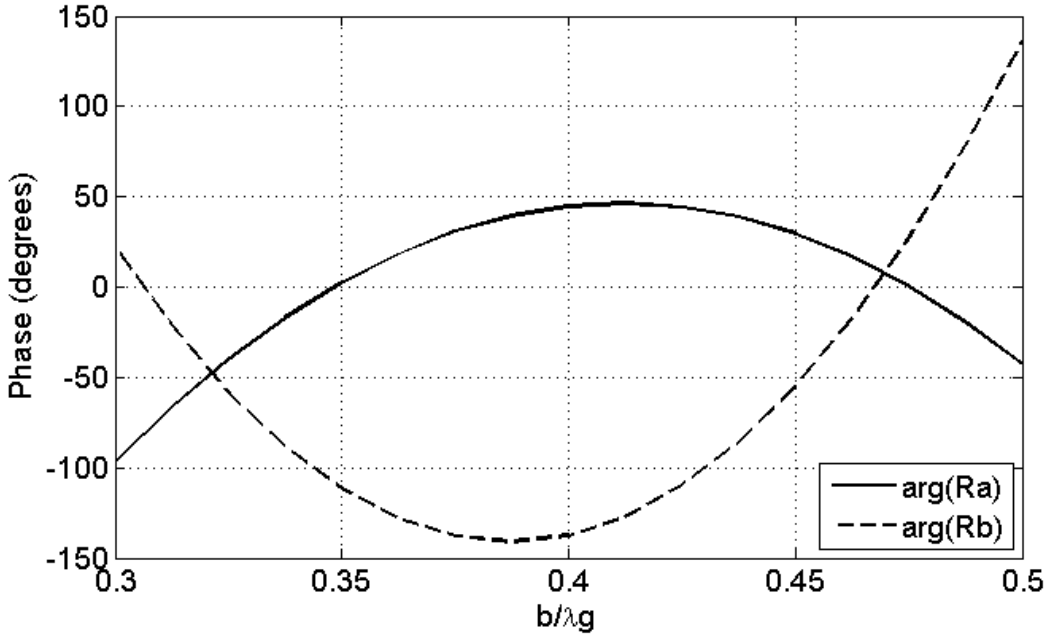

Figure 4-3: Phase diagram of arms A and B as a function of iSINRD guide width, *b*, at 94 GHz.

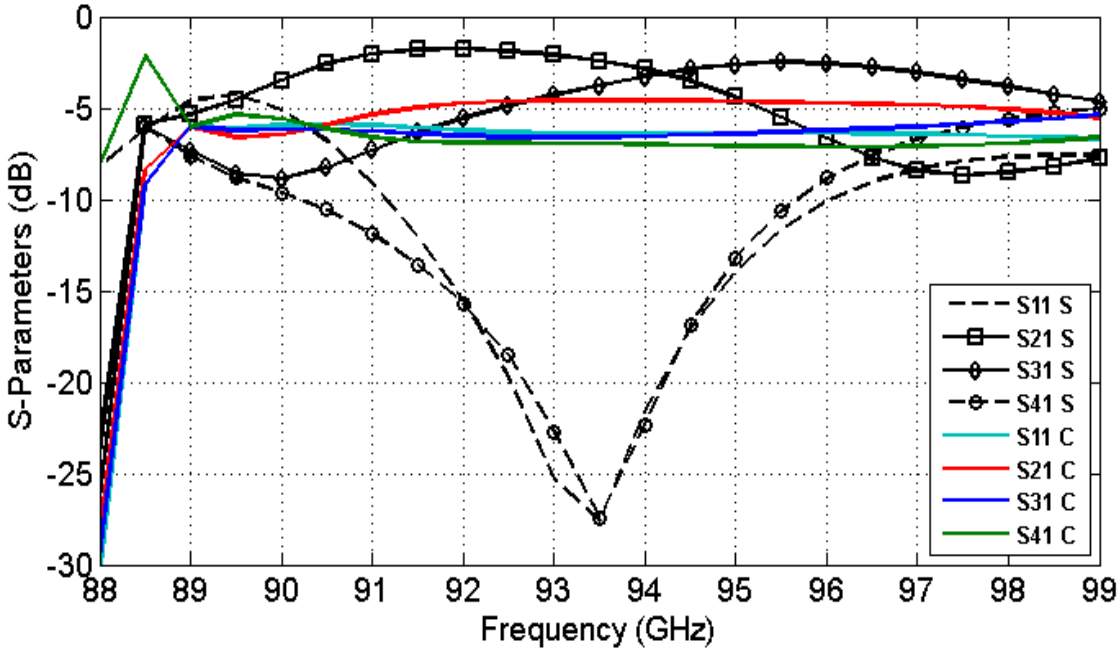

Figure 4-4: The simulated (S) and calculated (C) S-parameters of the iSINRD cruciform coupler obtained from the configurations in Figure 4-5 below.

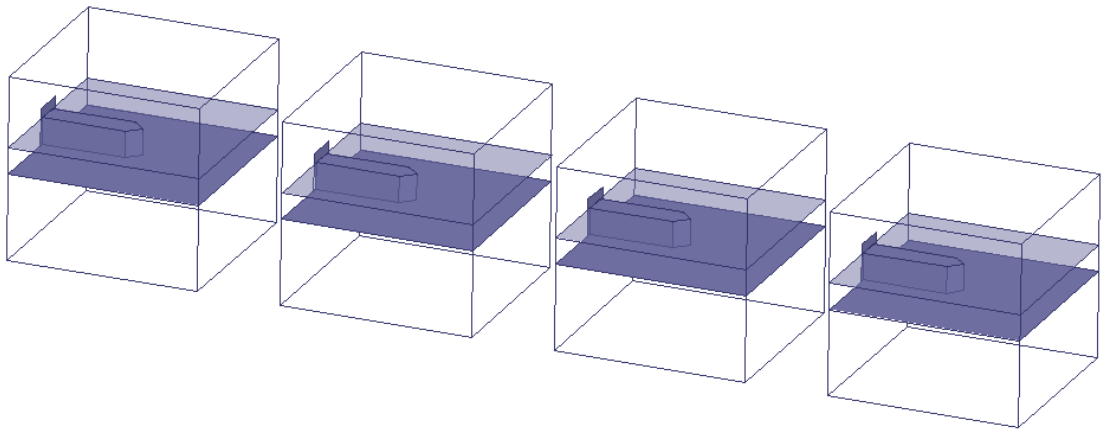

Figure 4-5: The incorrect setup of the arms in [51].

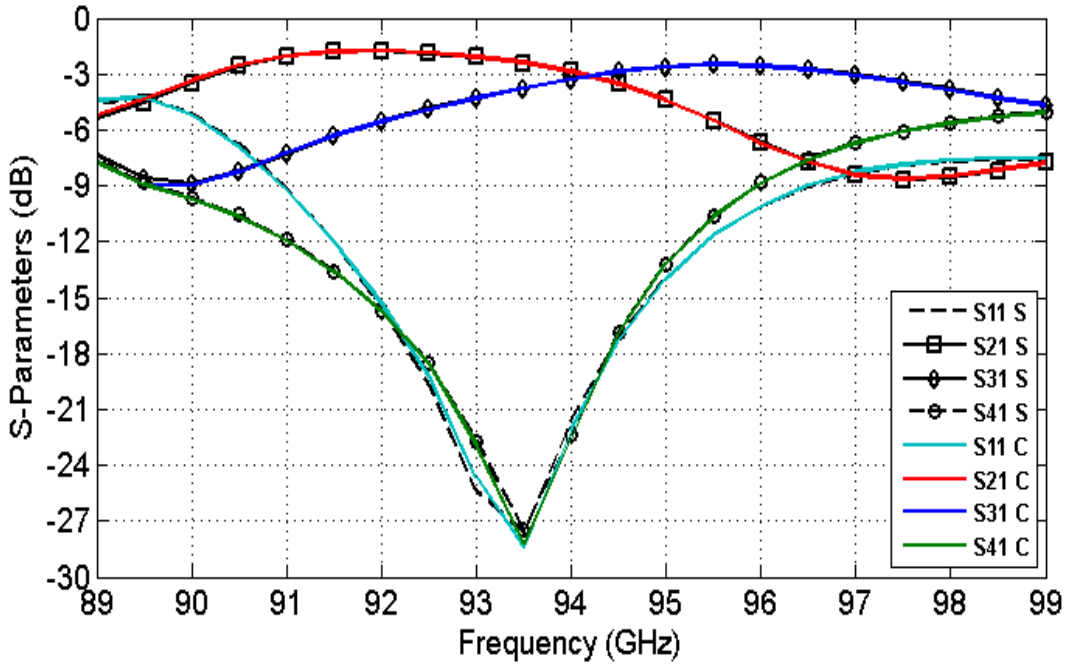

Figure 4-6: The simulated (S) and calculated (C) S-parameters of the iSINRD cruciform coupler obtained from the configurations in

Figure 4-7below.

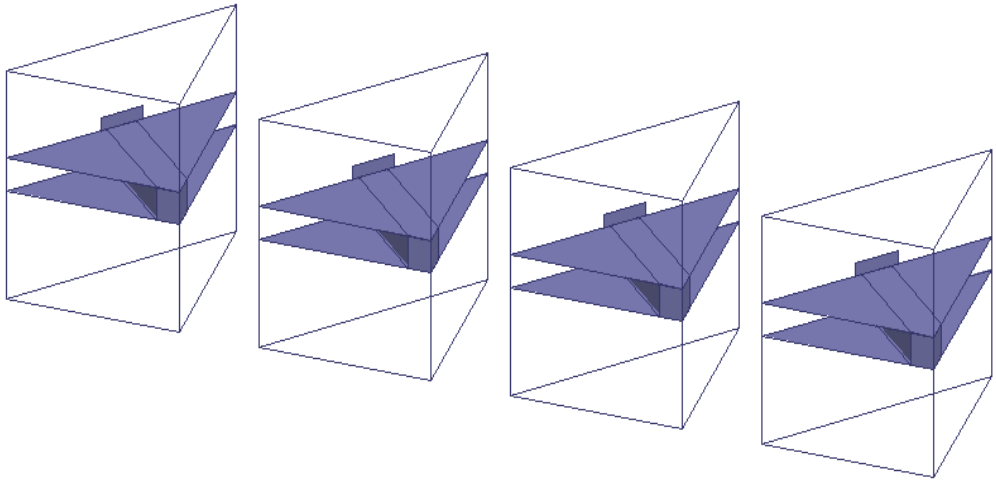

Figure 4-7: The correct setup of the arms in [51].

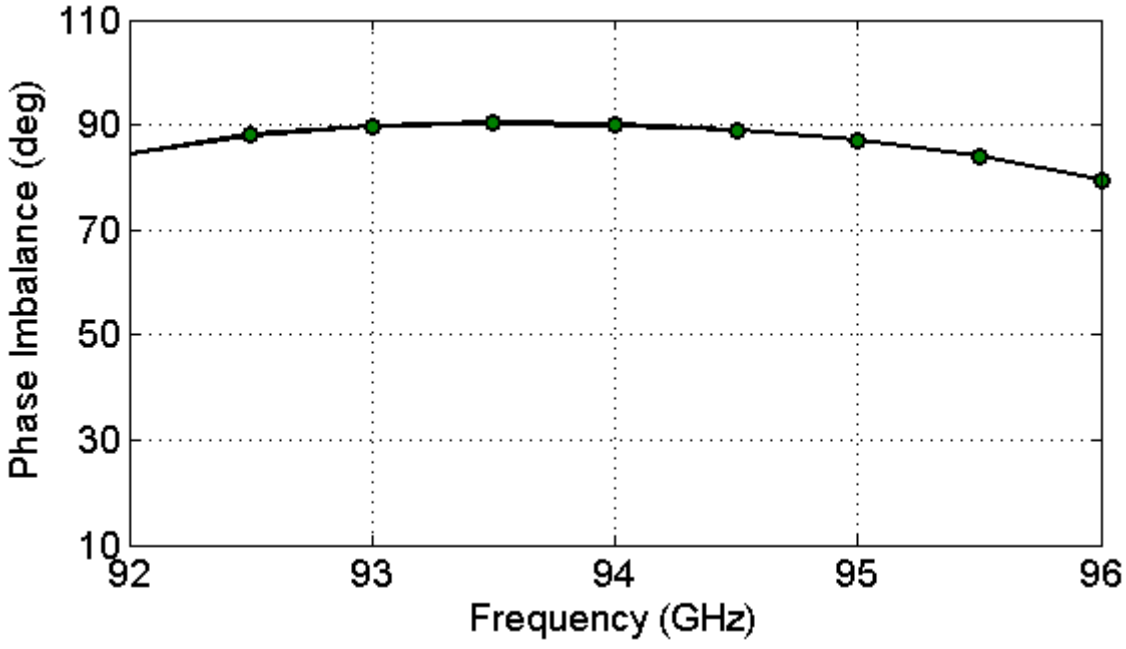

Figure 4-8: Phase variation of the iSINRD cruciform coupler with respect to frequency.

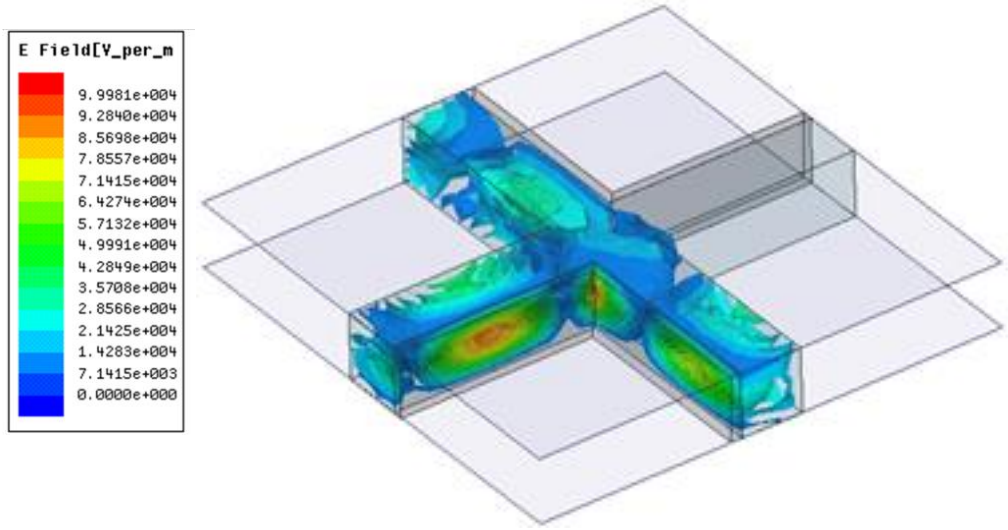

Figure 4-9: A 3-D plot of the electric field of the LSM_{10} mode in the iSINRD cruciform coupler.

4.3 An Asymmetric Planar iSINRD Cruciform Magic-T

The magic-T, originally developed in the WWII era [78], is indispensable for many microwave circuits (e.g. mixers [79]) that rely on power distribution. The classical approach in designing a rectangular waveguide magic-T is to combine E-plane and H-plane T-junctions, such that the two junctions share the same output ports. This configuration is illustrated in Figure 4-10. Consequently, the vertical input arm is called the E-arm while the horizontal counterpart is called the H-arm. Arms 2 and 3 are simply called the collinear ports. To better reflect the functionality of the magic-T, the two input ports (1 and 4) are also called the difference and sum ports, respectively. This is because simultaneous in-phase feeding of the collinear arms (that is, 0^o phase difference) results in the power being added constructively at the H-arm (thus the sum port), and destructively at the E-arm (thus the difference port) [48], [78]; and vice versa (for 180^o phase difference). The principle of operation of the E-arm T-junction is shown in Figure 4-11. The reverse is true when the signal is fed at the H or E arm; power is equally divided (between the collinear ports) in-phase or out-of-phase respectively. Furthermore, the two collinear ports are perfectly isolated; feeding either of the collinear ports results in the power being equally split between the E and H arms, while no power goes into the other collinear port. Hence, unlike the

standard E and H T-junction power dividers, one of the key features of the magic-T is the very high isolation between any pair of opposite input ports, while still maintaining the power division functionality. This is true for simultaneous feed of any two ports. The other key feature is the in-phase (0^o) and out-of-phase (180^o) outputs of the H and E arms. Consequently, the S-matrix of a magic-T circuit is given by [48]:

$$[S]=\frac{1}{\sqrt{2}}\begin{bmatrix}0 & 1 & 1 & 0\\ 1 & 0 & 0 & -1\\ 1 & 0 & 0 & 1\\ 0 & -1 & 1 & 0\end{bmatrix} \qquad (4.6)$$

\

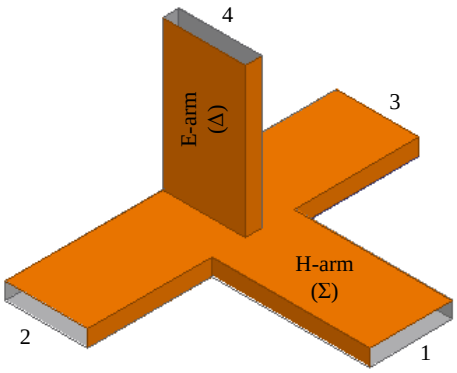

Figure 4-10: A 3-D view of a conventional rectangular waveguide magic-T power divider.

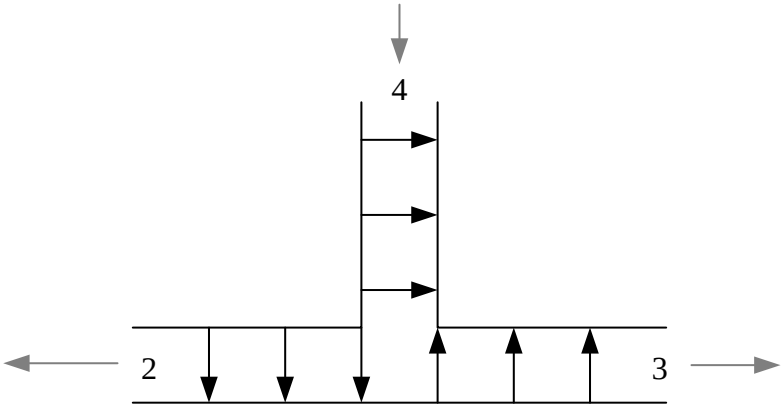

Figure 4-11: Out-of-phase power division of the E-plane T-junction; black arrows represent electric field lines. Grey arrows represent direction of power flow.

A lot of research has been directed at developing planar magic-T circuits [80–87]. Within the SICs paradigm, numerous planar magic-T circuits have been reported in the literature [88–94]. Those circuits, however, involve microstrip and slot-line transitions and are thus limited to the X band frequencies or lower-end of millimeter-wave frequencies. On the other hand, the K-band NRD-microstrip-based magic-T reported in [39] requires multi-layer fabrication, which is not feasible in the W-band. In this section, the power division mechanism of the iSINRD cruciform coupler in Section 4.2 is utilized to realize a completely planar W-band magic-T.

4.3.1 Principle of Operation

The top view of the proposed iSINRD magic-T is shown in Figure 4-12. In this setup, the arms of ports 1 and 3 are each extended by a multiple of quarter a wavelength, which corresponds to a phase shift of 90^o; in addition to the other 90^o phase shift that already exists in the central junction, as aforementioned in Section 4.2. Then, if two waves are simultaneously incident on ports 2 and 3 and are excited in-phase, they will add up in the H-arm, and subtract in the E-arm. This happens because the wave from port 3 is delayed by 90^o, relative to port 2, due to the $\lambda_g/4$ path difference, but is not delayed at the junction. On the other hand, the wave incident at port 2 is subjected to a 90^o phase shift at the junction, relative to port 3 (as explained in Section 4.2), but does not experience a phase shift before that since no $\lambda_g/4$ extension is applied to arm 2. Hence the two waves arrive in-phase, and add up, at the H-arm. Contrary to that, the two waves will subtract at the E-arm, since the wave from port 3 undergoes a total phase delay of 180 relative to port 2. Using the same, if the two waves incident at ports 2 and 3 are instead excited out-of-phase, they will add up in the E-arm and subtract in the H-arm. In addition, a single wave incident at port 2 or port 3 will arrive out-of-phase or in-phase at ports 1 and 4; respectively. Also, ports 1 and 4, as well as the ports 2 and 3, are perfectly isolated as explained in section 4.2. Finally, apart from the 90^o phase shift at the junction, the way in which the signal splits is identical to that shown in Figure 4-11 for an E-plane junction. Hence, a planar magic-T operation that very closely mimics the original one (the one in Figure 4-10), is achieved which avoids the complexity of integrating two separate T-junctions (as in traditional magic-T circuits), or multilayer configuration [39]. Due to the asymmetry of this magic-T, it is called an asymmetric iSINRD magic-T.

The dimensions of the proposed asymmetric iSINRD magic-T are identical to the iSINRD cruciform coupler of Section 4.2, except for the quarter wavelength length extension of arms 1 and 3. The simulated S-parameters are the same as those of the cruciform coupler shown in Figure 4-6. The simulated phase variation relative to the sum and difference ports (port 1 and port 4) is shown in Figure 4-13. The simulated field plots for the two inputs are shown in Figure 4-14, while the field plots for concurrent excitation (in-phase and out-of-phase) are shown in Figure 4-15, which validates the above discussion.

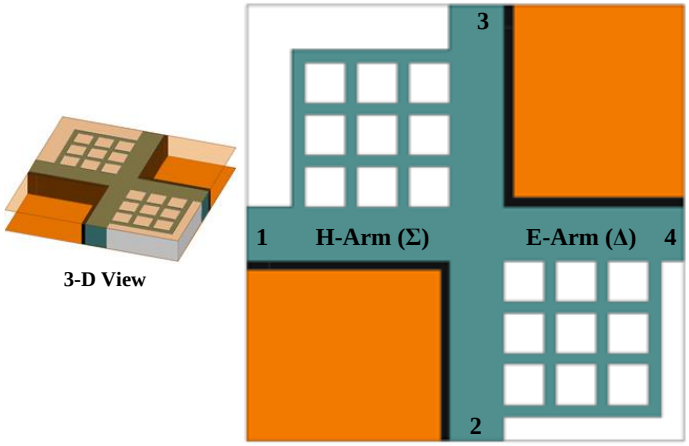

Figure 4-12: A 3-D view (left) and a top view of the asymmetric iSINRD cruciform magic-T.

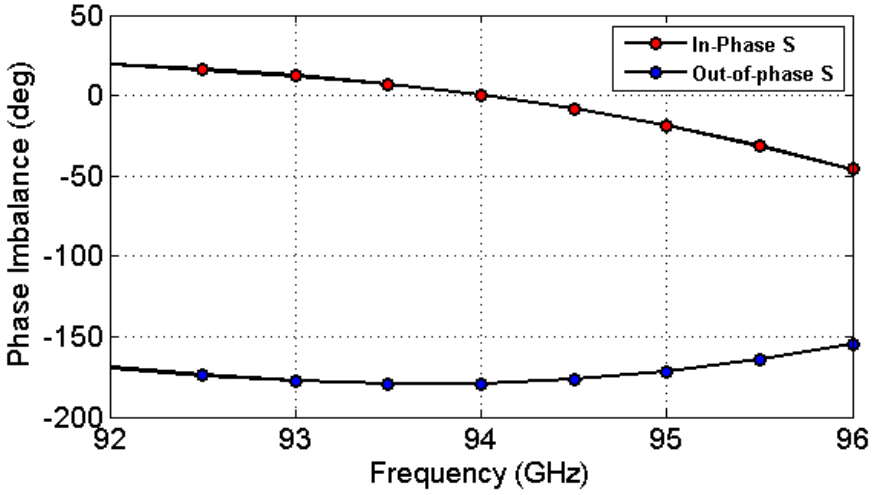

Figure 4-13: Phase difference relative to the ports 1 (in-phase) and 4 (out-of-phase).

Figure 4-14: Top view plot of the E-field of the LSM_{10} mode due to feeding at input 3 (left) and input 2 (right).

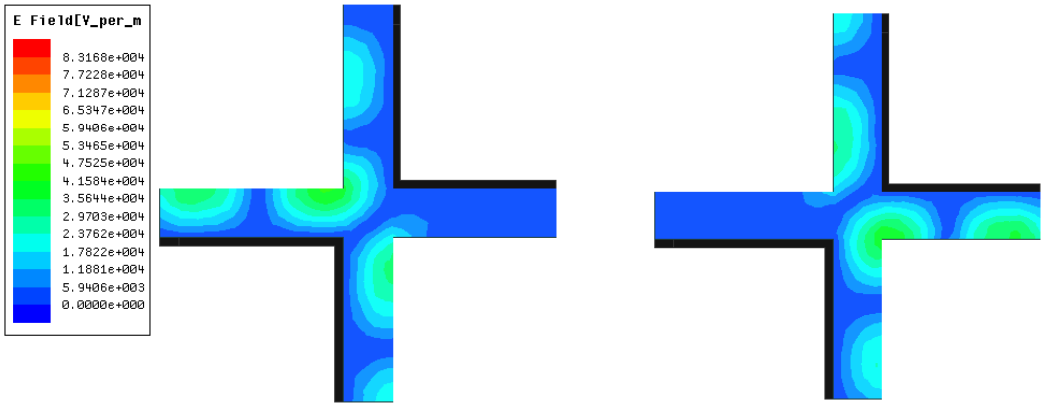

Figure 4-15: Top view plot of the E-field of the LSM_{10} mode due to in-phase (left) and out-of-phase (right) simultaneous excitation of ports 2 and 3, respectively.

4.4 A W-Band Ortho-mode Transducer Based on the Image SINRD (iSINRD) Guide

The recent years has witnessed an exponential growth in planar hybrid circuits like couplers, filters and ortho-mode transducers (OMTs). The latter is especially interesting for millimeter wave applications where two signals of opposite polarities can be transmitted or received using a single channel. Many types and classes of OMTs exist, as discussed in [95]. For the design of a planar OMT, the narrow band acute angle OMT is the most suitable choice [95]. Figure 4-16 shows a schematic view of a narrowband acute angle OMT, typically designed for operation with TE_{10} and TE_{01} modes [95]. The advantage of this OMT scheme is that no tapering of the thickness of the output arms is required, as is the case with the other OMT types [96–98]. However, in this OMT type, septa would need to be introduced in the branching arms in order for each arm to support only one of the two modes [95]. This is a daunting task at millimeter wave frequencies, given the minute lateral circuit dimensions that are in the order of less than one millimeter; not to mention the associated fabrication complexity and other limitations discussed in Chapter 1.

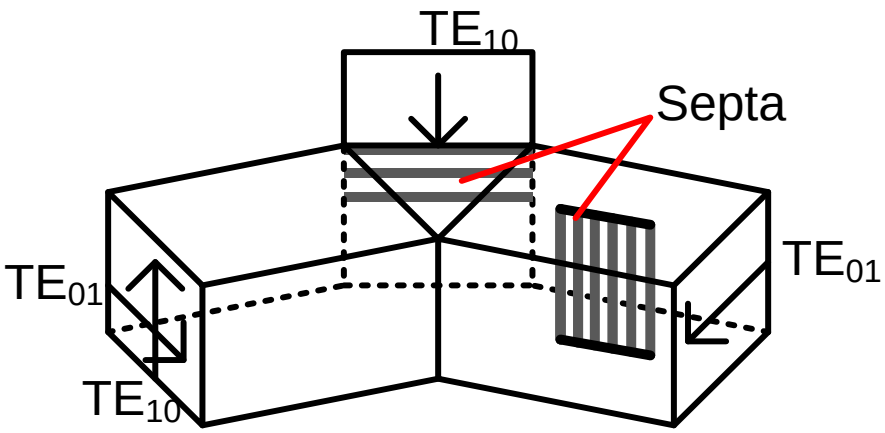

Figure 4-16: A 3-D view of a typical narrow-band, acute-angle OMT.

In this section, we investigate how the iSINRD guide provides a counter measure to these limitations. Specifically, the orthogonality of the LSM_{10} and TE_{20} modes in the image SINRD (iSINRD) guide and the SIW, respectively, is exploited to design a planar millimeter-wave

orthogonal-mode transducer (OMT). The two output arms are thus an iSINRD guide and an SIW. The proposed planar OMT belongs to the narrowband acute angle class. The top view of the proposed OMT is shown in Figure 4-17. The input port is port 1, and it supports the propagation of the LSM_{10} and TE_{20} mode, as discussed in Chapter 1. The output arms are port 2 and port 3, which separate the TE_{10} (not the TE_{20} mode) mode and the LSM_{10} modes; respectively. The width and height of all input and output arms are the same. More importantly, no septa or step changes in thickness are required, which makes it a novel OMT implementation, and thus the design complexity is reduced substantially; which augments the planar advantage of the narrow-band acute-angle OMT class. The orthogonal LSM_{10} and TE_{20} modes are shown again in Figure 4-18.

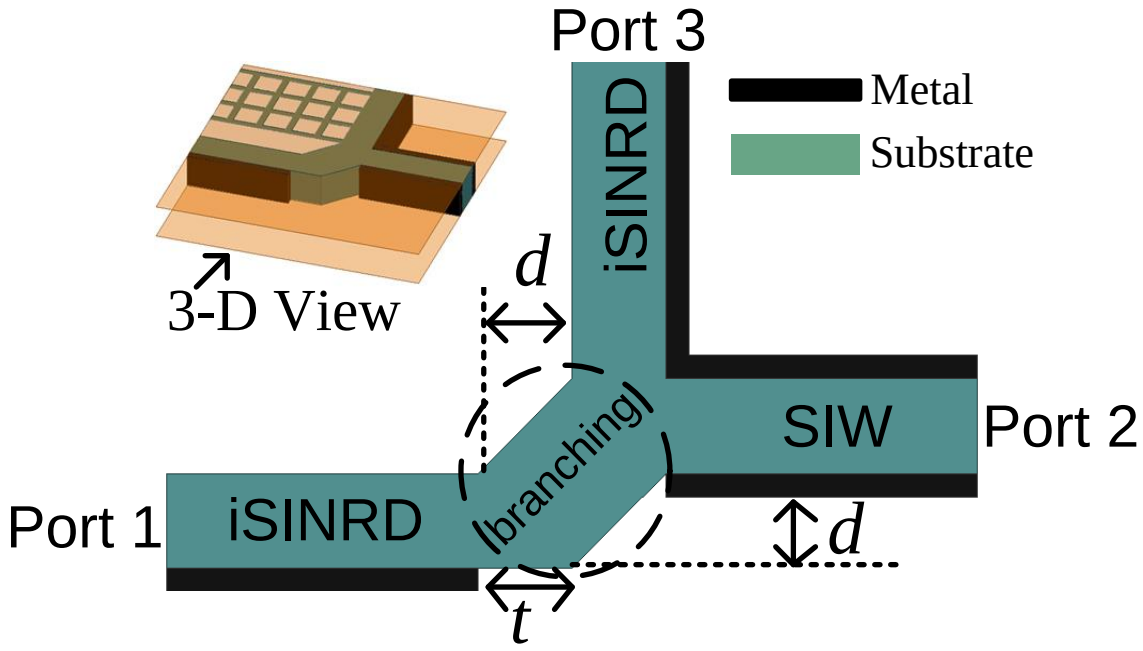

Figure 4-17: Top view of the proposed iSINRD-SIW OMT.

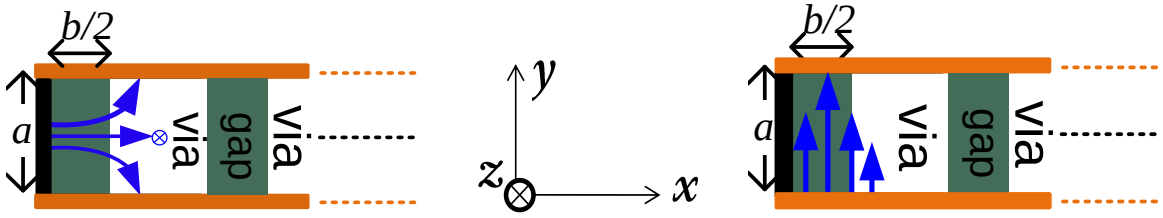

Figure 4-18: The LSM_{10} (left) and TE_{20} (right) modes in the iSINRD guide.

4.4.1 Mechanism of the Proposed OMT

The OMT then works as follows. For the LSM_{10} mode, since the E_z component must be null at the metal plane, the LSM_{10} mode cannot propagate into the SIW arm (port 2), and it will simply continue to the iSINRD arm (port 3). This is similar to the mechanism of the cruciform coupler described above, and in fact, for this mode, any value of d or t can be used, even $d = t = 0$.

For the TE_{20} mode, it must first be noted that while port 1 is fed with the TE_{20} mode, it propagates into the branching region and in the SIW arm as the TE_{10} mode. This is because the conditions that $E_y = 0$ at the metal plane and near the air-dielectric interface, and maximum in the center of the guide is required for both the TE_{20} and TE_{10} modes, and is met in both regions. Furthermore, the center of the guide will change for each region (for the iSINRD guide it is at the metal plane, for the branching region and SIW arm it is at the middle of the dielectric channel). In addition, in the SIW arm, the cut-off frequency of the TE_{20} mode is well beyond the f_x limit defined in Chapter 1, and so will not be excited at the intended operating frequency of 94 GHz.

The way in which the TE_{20} will propagate depends on the values of d and t. If both parameters are null, the TE_{20} mode will equally split between the iSINRD (as TE_{20} mode) and the SIW arm (as TE_{10} mode), since both have the same width and support both modes at 94 GHz. If d and t are tweaked, the division ratio changes depending on their values. Technically, what happens when d and t are changed is that the width of the feeding iSINRD arm is gradually tapered; increasing between the input and output iSINRD arms, and decreasing between the input iSINRD guide and output SIW. In the special case that $d = t = b/2$, the width of the branching region exactly half-way between the input iSINRD arm and the output SIW is twice the width of any of the input and output arms of the OMT. It then follows that the TE_{10} mode at that reference point cannot turn into the iSINRD output arm, since its metal image plane will then coincide exactly with the maximum of the E_y component of the TE_{10} mode in middle of the branching region. Hence, the TE_{10} mode will gradually taper into the SIW arm, and will be shorted at the iSINRD arm. As is apparent, excellent separation of the two modes can be achieve without introducing any septa, similar in fashion to the cruciform couplers presented above which do not require any modulation of the coupling junction.

4.4.2 Dimensions of the proposed OMT

As stated above, for optimum operation of the OMT junction, the lateral width of the branching junction must be twice the width of the iSINRD guide, which corresponds $d = t = 0.6\lambda_g$. These dimension can be verified by optimizing the structure using [51], and according to the curves in Figure 4-19 to Figure 4-22, the optimum dimensions for dual mode operation at 94 GHz indeed correspond to $d = 0.6$ mm. Note that this means that the width of the iSINRD or SIW arms is $0.6\lambda_g$; which is larger than the (optimum) width of $0.413\lambda_g$ of all previous circuits. The reason is purely related to fabrication limitation. The field plots for each mode, shown in Figure 4-23 and Figure 4-24, illustrate the principle of operation of the OMT.

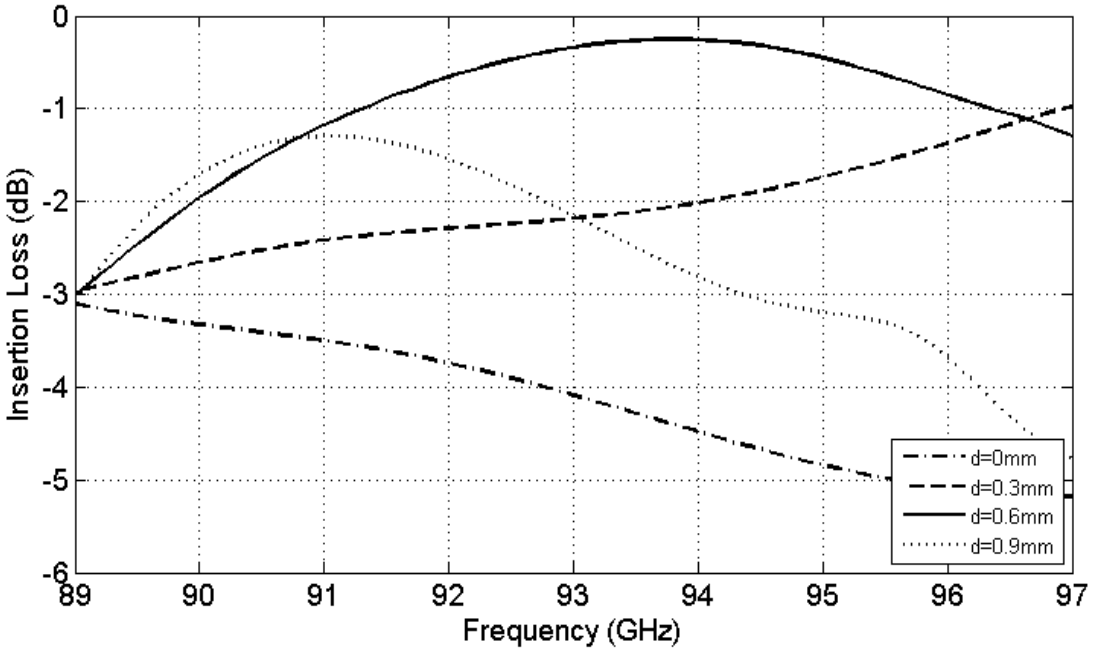

Figure 4-19: Insertion loss (S31) for different values of d (the LSM_{10} mode) as function of frequency.

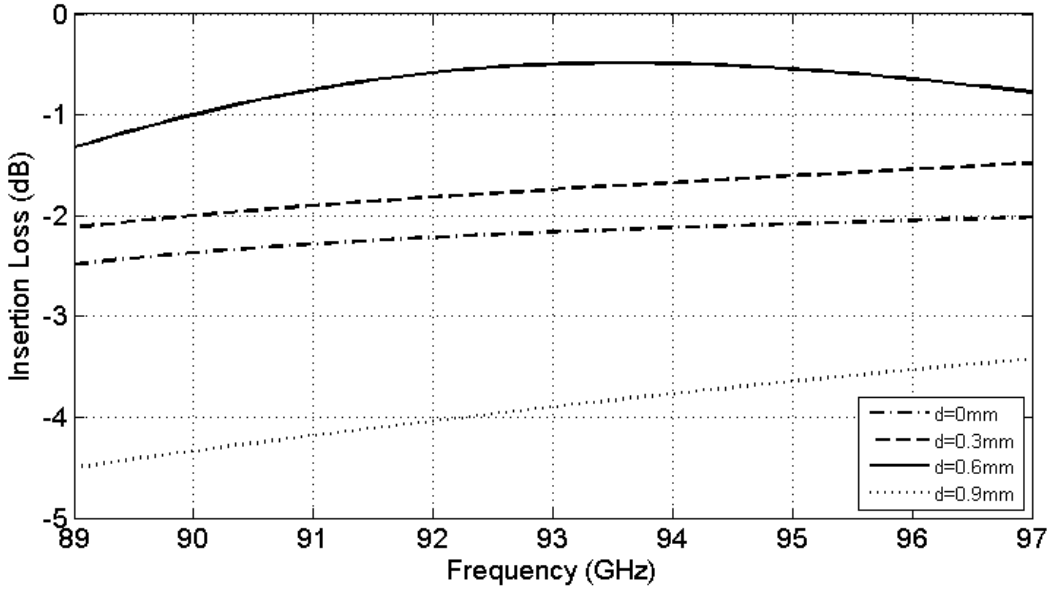

Figure 4-20: Insertion loss (S21) for different values of *d* (the TE_{20} mode), as a function of frequency.

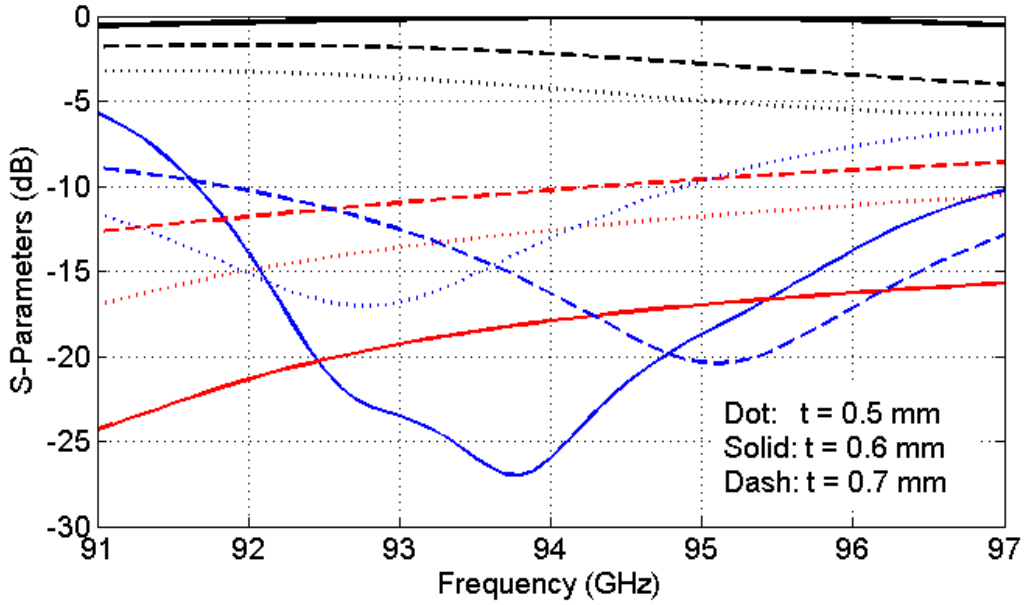

Figure 4-21: The effect of inset distance *t* on the S-parameters of the TE_{20} mode. Black: transmission; red: reflection; blue: isolation.

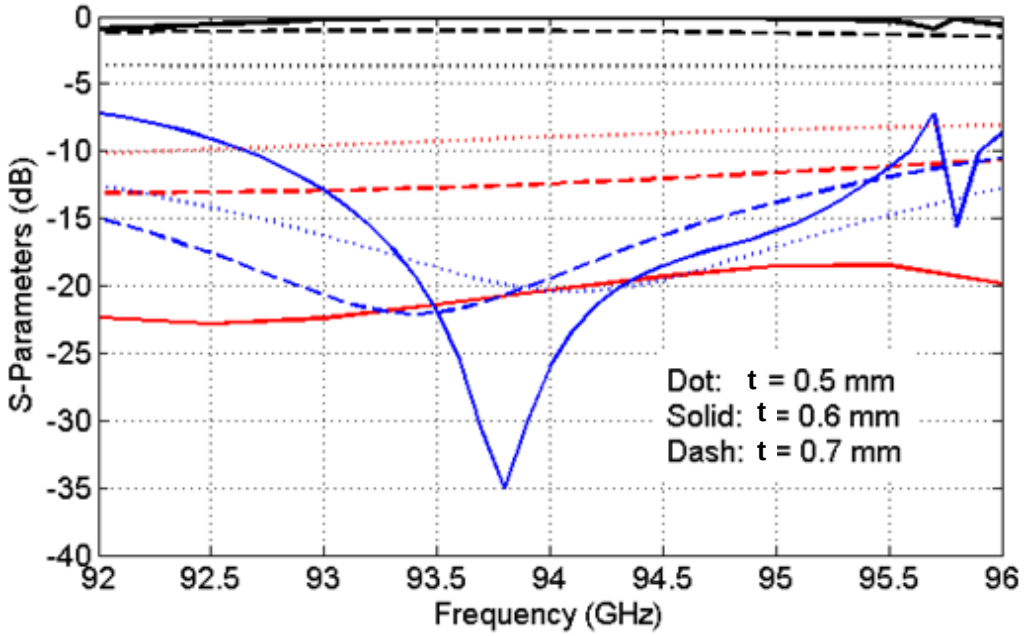

Figure 4-22: The effect of inset distance t on the S-parameters of the LSM_{10} mode. Black: transmission; red: reflection; blue: isolation.

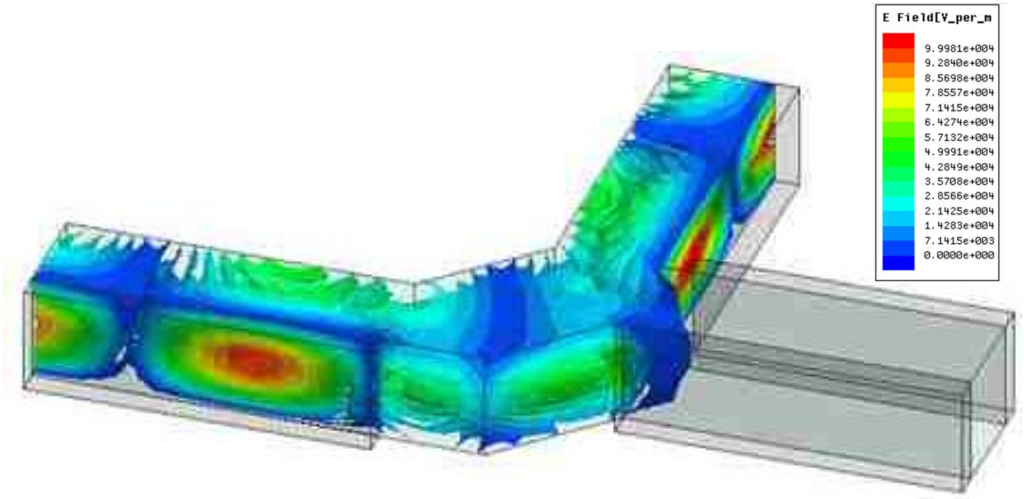

Figure 4-23: A 3-D plot of the E-field of the LSM_{10} mode in the iSINRD-SIW OMT.

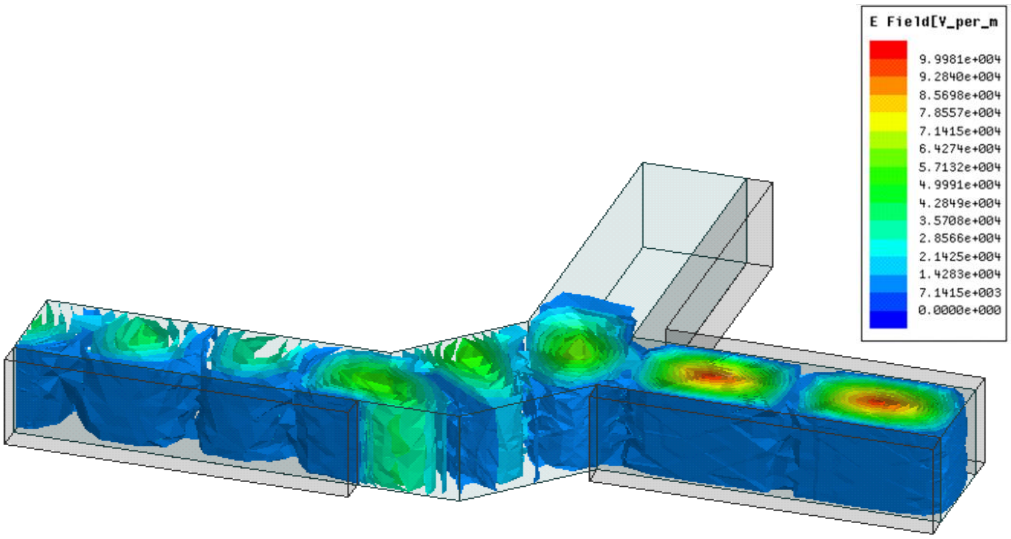

Figure 4-24: A 3-D plot of the E-field of the TE_{20} mode in the iSINRD-SIW OMT.

4.4.2.1 Exciting the Orthogonal Modes

As with all the other iSINRD circuits discussed thus far, the tapered transition to WR10 is used to excite the LSM_{10} mode. Similarly, the TE_{20} mode is excited using a tapered transition that uses the principle outlined in [66]. Since the two modes (and their WR10 feeding transitions) are orthogonal, the proposed iSINRD-SIW OMT cannot be fabricated as a three-port device. Instead, the OMT approach in [99], [100] is employed, where the 3-port OMT is fabricated back to back so that it has four ports; two of which act as feeding ports for the LSM_{10} and TE_{20} modes. Hence, conflict in mode excitation is avoided since each mode is being fed separately. The suggested four ports OMT, its simulation results and field plot of simultaneous feed, are shown in Figure 4-25 to Figure 4-28, respectively. The "common channel" is thus an iSINRD guide that supports both (superposed) modes. The feed to the iSINRD arms is realised by tapering the subtrate into the WR10 guide. On the other hand, the feed to the SIW arms is simply achieved by extending the substrate into the WR10 guide. Probe dimensions were optimized using [51]; lengths of iSINRD and SIW tapers are 1 mm and 0.6 mm, respectively.

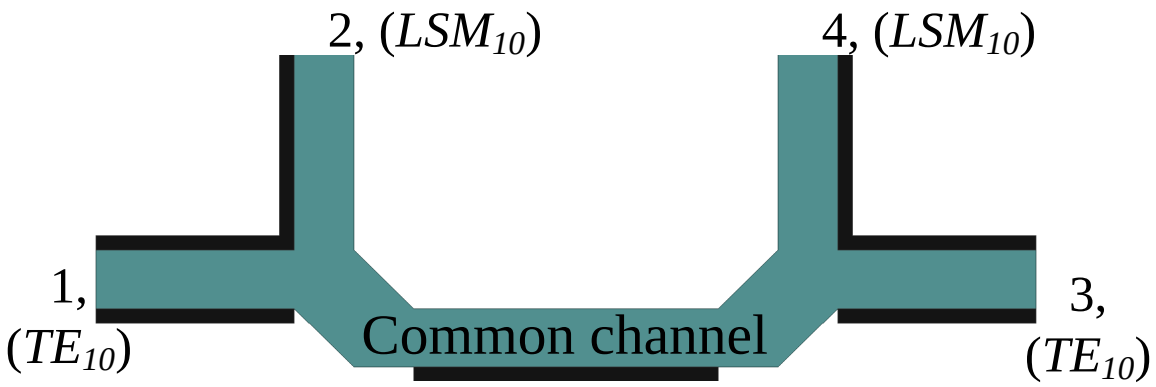

Figure 4-25: The top view of a back to back, four-port iSINRD-SIW OMT.

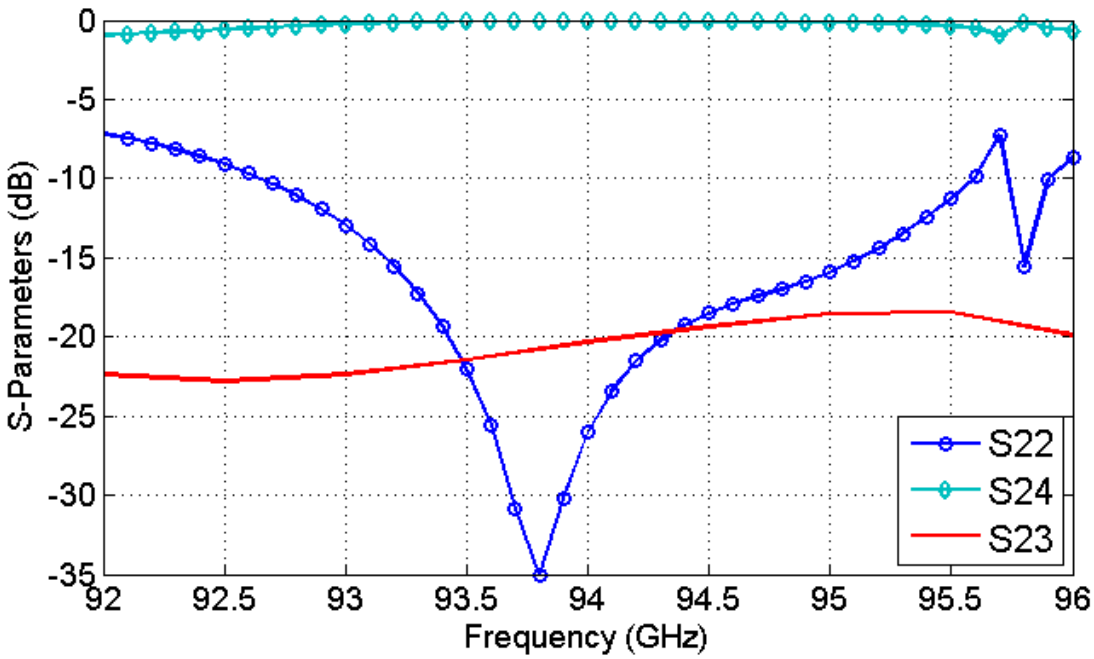

Figure 4-26: The simulated S-parameters for the LSM_{10} mode.

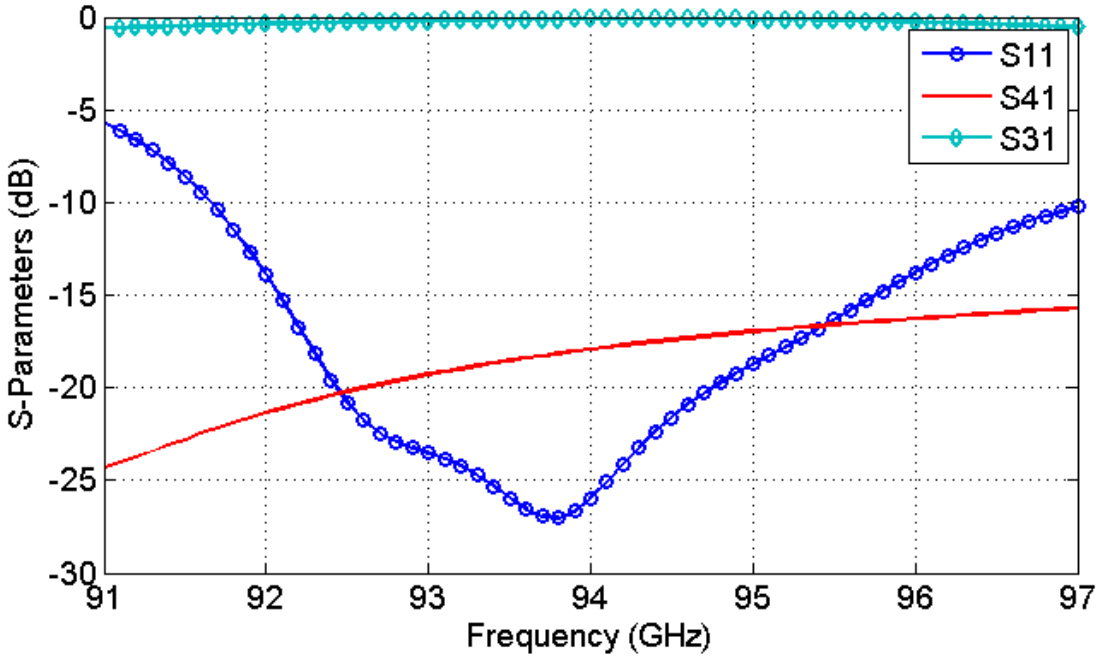

Figure 4-27: The simulated S-parameters for the TE_{20} mode.

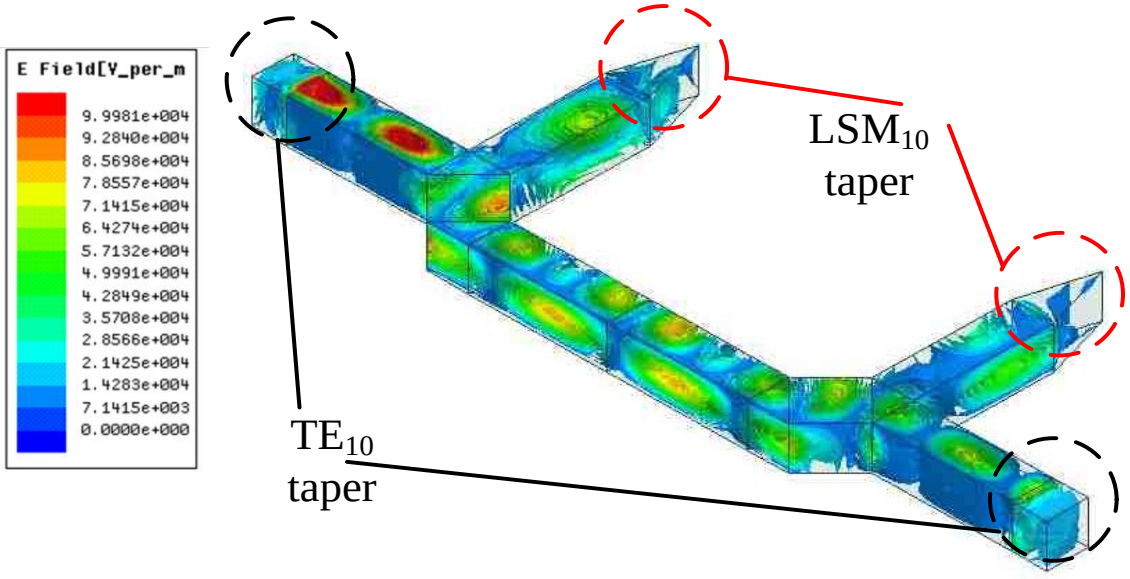

Figure 4-28: A 3-D E-field plot of the four-port OMT, with simultaneous LSM_{10} and TE_{20} feed (top left corner). Notice the excellent separation at the output branches.

Unlike the LSM_{10} mode, which can still be contained in the dielectric despite some substrate perforation, the TE_{20} mode requires an intense perforation that renders the iSINRD guide an iNRD guide. Otherwise, the TE_{20} mode easily leaks into the side region. Therefore, an iSINRD circuit that involves operation with the TE_{20} mode must have bends or arms that involve the TE_{20} mode as iNRD guide. The field plots in Figure 4-29 and Figure 4-30 illustrate this idea. It is clear from the two plots that the TE_{20} mode would leak if the substrate perforation is involved, such as the case in an iSINRD guide bend. Conversely, an iNRD guide bend would contain the TE_{20} mode well with no leakage.

The proposed iSINRD/SIW OMT is compared in Table 4.1 with other W-band OMT structures reported in the literature [96–97]. Evidently, the proposed OMT has the better edge in terms of size, planar structure and ease of fabrication (since no speta or tapering is required). This further demonstrates the suitability of iSINRD guides for millimeter-wave applications.

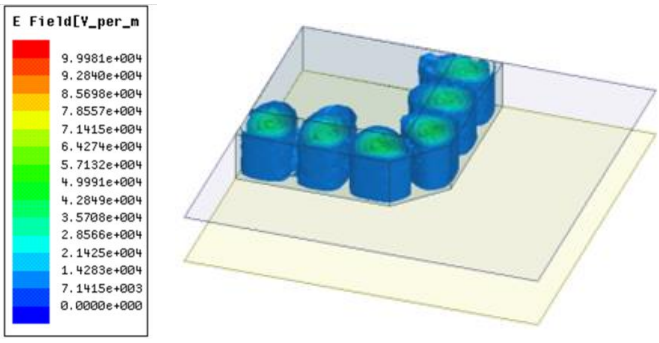

Figure 4-29: The TE_{20} mode is well contained in the guide when the side region is purely air.

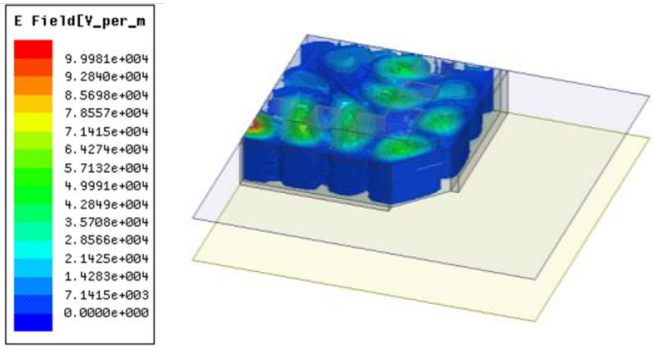

Figure 4-30: The TE_{20} mode easily leaks into the side region if it is perforated.

Table 4.1: Comparison between the proposed iSINRD/SIWOMT and other W-Band OMT's

Wavguide	Frequency (GHz)	Taper/Septum	Planar	Size (mm^3)	Reference
iSINRD/SIW	94	No/No	Yes	5.2 × 2.2 × 0.635	This work
Rectangular	100	Yes/No	No	19 × 30 × 33	[96]
Rectangular	96	Yes/Yes	No	2.03 × 2.03 × 3	[97]

4.5 Experimental Results and Discussion

4.5.1 The iSINRD Cruciform Coupler

The cruciform coupler discussed above, was optimized using [51] and fabricated using a polished Alumina substrate . The fabricated prototype is shown in Figure 4-31. As can be seen, no inductive posts or reflecting mirrors are required in the central junction. Feeding is done using a tapered transition to WR10 waveguide. The measured S-parameters and phase imbalance are shown in Figure 4-32 and Figure 4-33 respectively, together with the simulation results. Evidently, a good agreement between simulation and measurement is observed; thus validating the proposed novel iSINRD guide coupler.

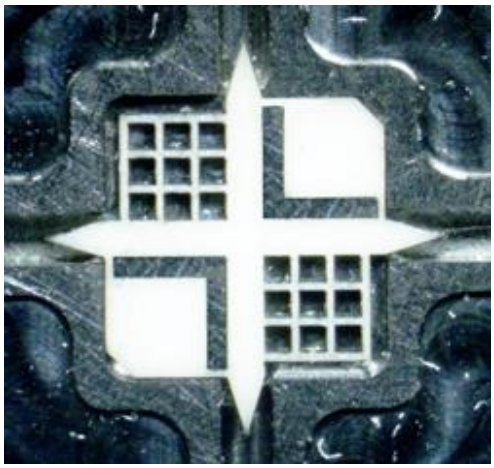

Figure 4-31: Top view of a fabricated iSINRD cruciform coupler.

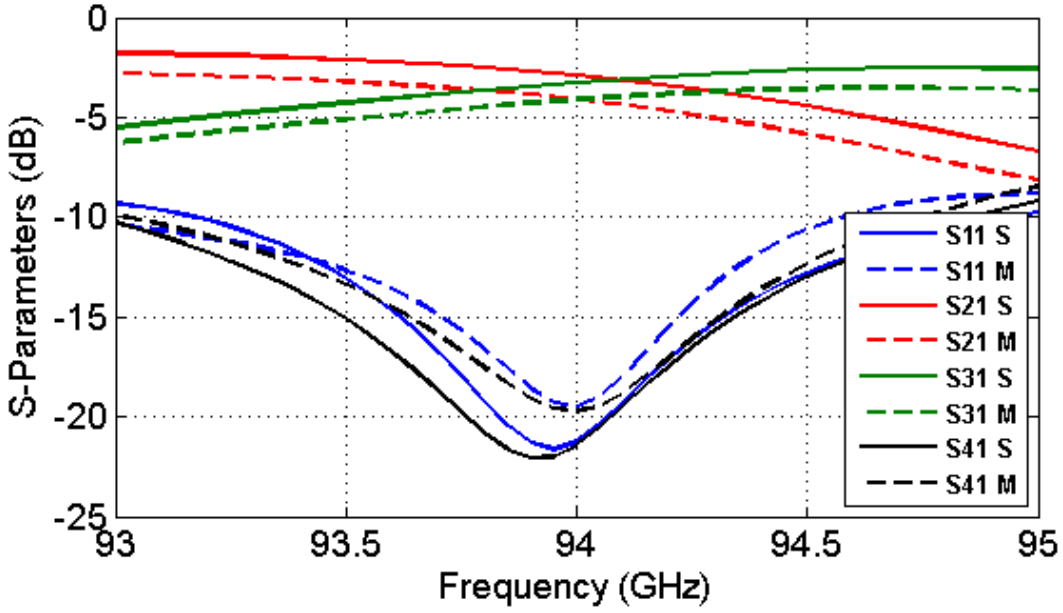

Figure 4-32: The simulated (S) and measured (M) results of the iSINRD cruciform coupler.

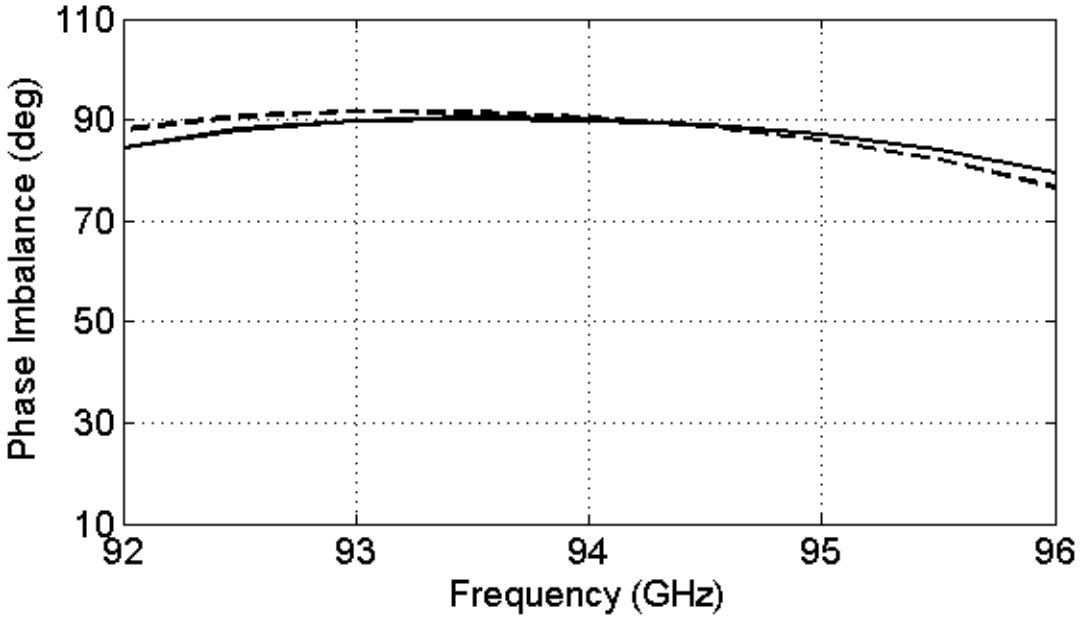

Figure 4-33: The simulated (S) and Measured (M) phase differences of the iSINRD cruciform coupler.

4.5.2 The iSINRD Cruciform Magic-T

The iSINRD magic-T was fabricated using a polished Alumina substrate. Figure 4-34 shows the top view of the fabricated prototype, together with the tapered transition to WR10 waveguide. Measured S-parameters and phase difference are shown in Figure 4-35 and Figure 4-36, together with the simulated one. The coupling level is around 4.75 dB, while the isolation and reflection are both better than 17 dB. The measured coupling level is less than what was measured for the iSINRD cruciform coupler. This is expected since the asymmetric iSINRD magic-T has two arms that are longer than their counterparts in the iSINRD cruciform coupler. Consequently, more loss will be measured in the magic-T compared to the coupler, which explains the observed difference in losses between the two. A small shift in frequency is also observed between the measured and simulated S-parameters and phase imbalance. This can be attributed to fabrication inaccuracies, especially in the width and the length of the tapers, which would then cause a shift in frequency. Such minute inaccuracies are difficult to avoid at W-band frequency..

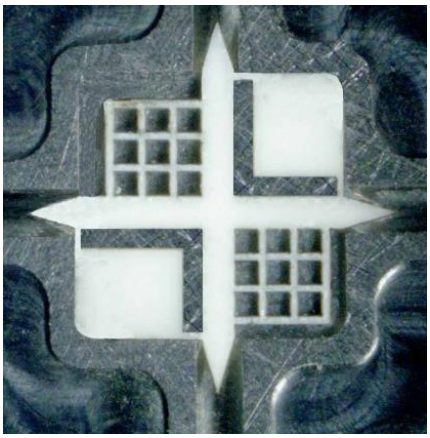

Figure 4-34: Top view of a fabricated asymmetric iSINRD cruciform magic-T.

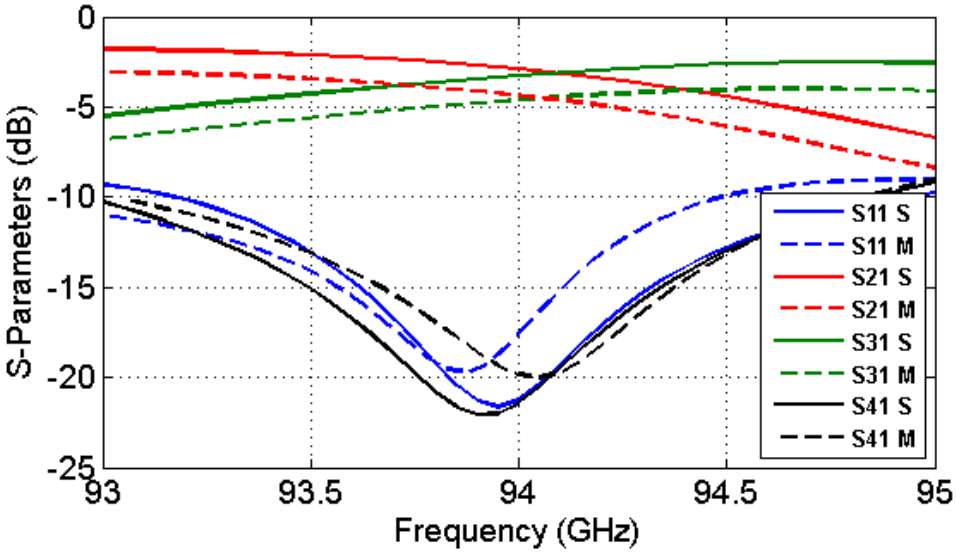

Figure 4-35: The Simulated (S) and measured (M) results of the iSINRD cruciform magic-T.

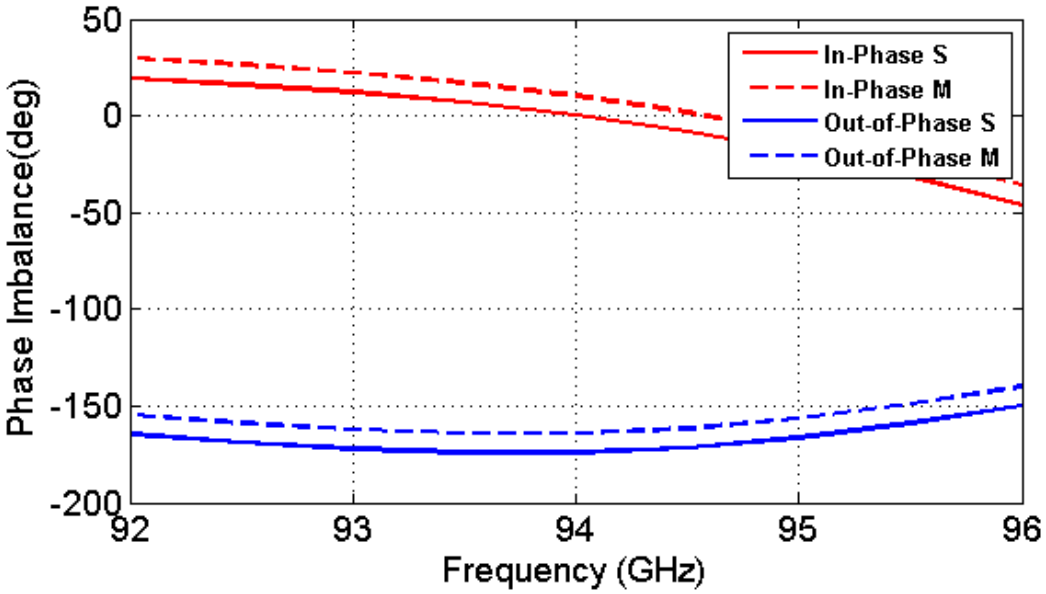

Figure 4-36: The simulated (S) and measured (M) phase difference of the asymmetric iSINRD cruciform magic-T, relative to the ports 1 (in-phase) and 4 (out-of-phase).

4.5.3 The iSINRD-SIW Ortho-Mode Transducer

As with all the preceding circuits, the four-port iSINRD OMT was fabricated using a polished Alumina substrate, and is shown in Figure 4-37, together with the tapered transition to WR10 waveguide. The measured response for the LSM_{10} and TE_{20} modes are shown respectively in Figure 4-38 and Figure 4-39, together with the simulated response. The insertion loss, for the two inputs, is better than 1 dB, while the isolation and reflection are both better than -17 dB.

Figure 4-37: Top view of a fabricated iSINRD-SIW planar OMT.

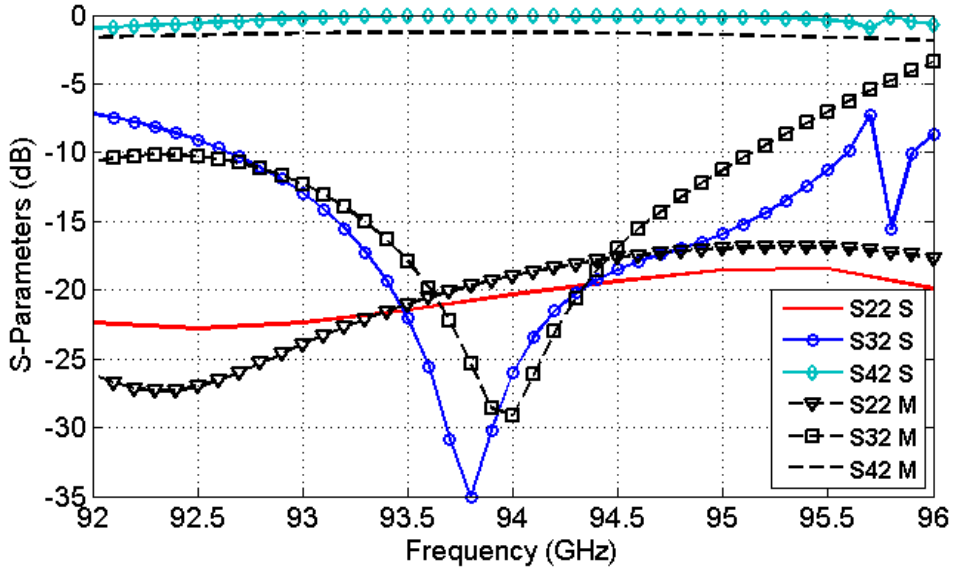

Figure 4-38: The simulated (S) and measured (M) S-parameters for the LSM_{10} mode.

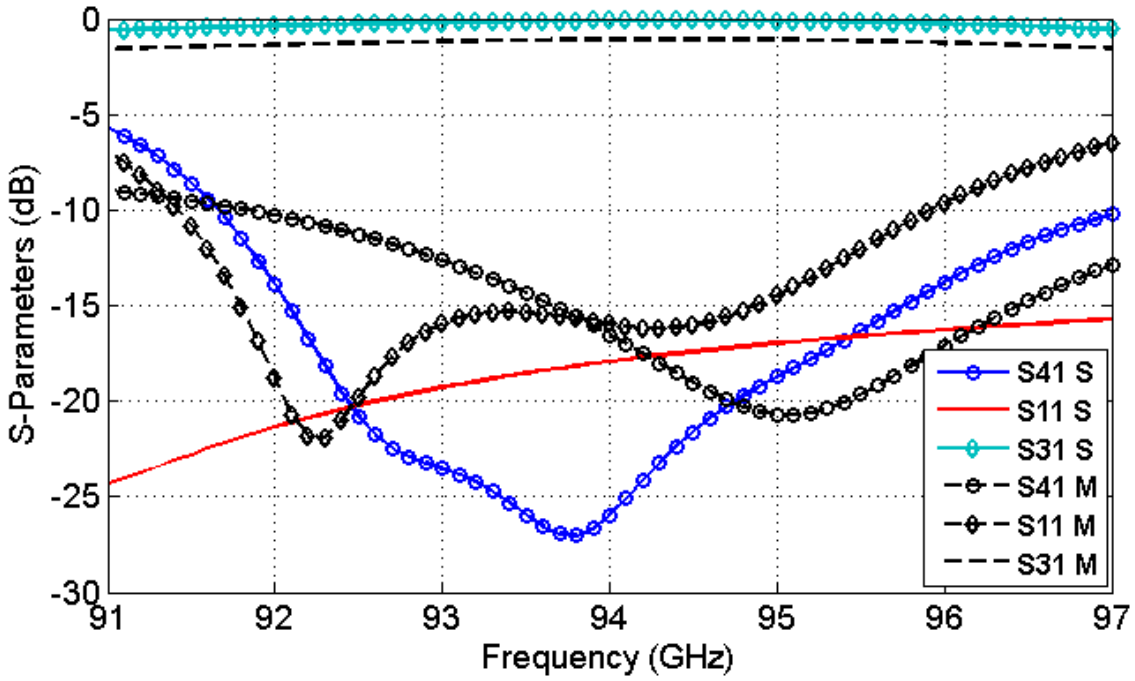

Figure 4-39: The simulated (S) and measured (M) S-parameters (TE_{20} mode).

CONCLUSION AND OUTLOOK

The evolution of communications systems and their underlying technologies continues to provide researchers with new creative ideas and pushes the current state-of-the-art to new milestones, involving active as well as passive components and devices. The state-of-the art technique for designing passive components is the substrate integrated circuits (SICs) technique, which combines planar technologies such as microstrip with waveguide technologies, such as rectangular and dielectric waveguides, in a completely planar and integrated fashion. This accelerated the design of communications systems and circuits at the millimeter and sub-millimeter wavelengths, and more recently in the terahertz frequencies.

Although the SICs is adaptable to any type of waveguide, it is most often implemented with the substrate integrated waveguide (SIW) (based on the rectangular waveguide), since it involves relatively fewer design parameters and its dominant mode is easier to excite. With increasing frequencies, however, the design flexibility of the SIW is adversely affected due to the sharp increase in losses. This is especially true in the SIW since it comprises four ground planes, and its dominant mode, namely the TE_{10} mode, is orthogonal to the top and bottom ground planes. Furthermore, the SIW does not support any *TM* mode (due to the discrete side metal walls), and hence does not exploit the full potential of the original rectangular waveguide (in terms of multi-mode operation). In addition, at the W-band and above, the dimensions of the SIW approach the fabrication tolerance of the PCB process, which limits its design to specific fabrication technologies that are not as easily accessible.

In light of the above limitations, a better alternative of the SIW at millimetre wave frequencies is the substrate integrated non-radiative dielectric (SINRD) waveguide. The SINRD guide comprises only two (top and bottom) ground planes and one of its dominant modes, the LSM_{10} mode, is predominantly parallels to the ground planes. Therefore, losses can be significantly decreased when operating with this mode. Furthermore, unlike the SIW, the SINRD guide supports all the dominant modes of the original NRD guide. In particular, the LSM_{10} mode is a *TM* mode, and together with another dominant mode, the LSE_{10} mode (which is a *TE* mode) sets the SINRD guide at a higher research potential than the SIW. Moreover, the SINRD guide also supports all the TE_{n0} modes, including the TE_{10} mode, albeit with different cut-off conditions. This means that the SINRD guide can easily substitute the SIW for millimeter-wave applications.

The anticipated transition from the SIW to the SINRD guide, however, is mainly hindered by the fact that the SINRD guide is susceptible to mode conversion between the LSM_{10} and the LSE_{10} modes at bends, which complicates the design of SINRD circuits. The two perforated side regions that flank the SINRD guiding channel further stifles its design potentials since the perforation via holes augment the total width of the guide at least threefold.

The image NRD (iNRD) guide is thus sought as an enhancement to the SINRD guide, as it involves only one perforated side regions and its central (image) metal wall suppresses the LSE_{10} mode, while still supporting the propagation of the LSM_{10} and the even TE_{n0} modes (in their half "version"). Of the latter, the TE_{20} mode can be used as an alternative to the now suppressed TE_{10} mode. Therefore, the iNRD guide is equally rich in modes, and together with the fact that it has two sidewalls of different boundary conditions, sets it at an even higher research potential than the SINRD guide (and the SIW).

In this work, the iNRD guide was for the first time designed with the SICs technique, and the resulting iSINRD guide yielded a host of novel passive components that combined the manifold advantages of the iNRD guide and the SICs technology. At first, simple iSINRD guide transmission lines with different configuration of the image wall were analysed. This was done to gauge the effect of introducing gaps in the metal wall and comparing it to the ideal case of no gap. The result of this analysis helps determine the optimum number of gaps as well as their size that best yields the desired performance. This analysis was instrumental in designing a number of iSINRD guide directional couplers. In the first coupler, the image metal wall of the iSINRD guide is shared by two iSINRD guides and a number of gaps are introduced in this wall. A 3-dB forward coupling between the two guides thus was obtained at 94 GHz, with 9% bandwidth and a good agreement between simulations and measurements. Operating this coupler with the TE_{20} mode was impeded as it requires relatively larger gaps in the metal wall.

In a second coupler configuration, the perforated side of the iSINRD guide forms the coupling sections between the iSINRD guides. Only one row of air vias with increased via-to-via spacing is used to realise this common wall. A 3-dB coupling at 94 GHz, with similar bandwidth as the first type, was obtained. In addition, the fact that the central wall is made of air vias facilitated the coupling of the TE_{20} mode. Indeed, 3-dB forward coupling at 94 GHz was obtained with the TE_{20} mode. Moreover, it was found that 0-dB coupling for both modes can be obtained at 88 GHz with

this coupler configuration. Consequently, this coupler can also be designed as a dual-mode crossover bridge, with each of the input ports being simultaneously fed with either the LSM_{10} or the TE_{20} modes. Then the two modes are collected at the diagonally opposite port. Measurements of this coupler/crossover were made at 88 GHz and 94 GHz, and a good agreement with the simulation was observed. Either, of the above two couplers could be modified by setting the length of one of the output arms to be longer that the other by quarter a wavelength. The coupler is then an 180^{o} hybrid circuit. To avoid redundancy, this hybrid was only tested with the second coupler configurations, and again satisfactory measurement results were obtained at 94 GHz.

In a similar fashion, an asymmetric iSINRD-iSIW directional coupler was also investigated, in which one of the guides is an iSINRD guide while the other is an iSIW (inverted SIW). When the LSM_{10} mode is fed into the iSINRD guide, it will convert to the TE_{01} mode in the SIW guide, since both possess the same E-field polarization in the y-direction.

All the above directional couplers require bends in order to facilitate transition to the WR10 waveguide. Therefore, an investigation of iSINRD bends based on the LSM_{10} and TE_{20} modes was carried out with satisfactory agreement of the measurement results to the simulations.

The nimbleness of the iSINRD guide was also highlighted in the design of cruciform circuits. Such couplers are designed by joining four different waveguide to a common central region. Analytically, each waveguide is assigned a different boundary (PEC or PMC) condition at this common region. Then the scattering parameters are calculated by superposing the four different scattering matrix of each individual waveguide according to the known even-odd mode analysis. The scattering parameters of the 3-dB iSINRD cruciform coupler were then calculated and plotted together with the simulated ones. Excellent agreement between the calculation and simulation was obtained which verified the design approach. The coupler was then fabricated and measured at 94 GHz; again yielding good agreement between measurement and simulation. In the above iSINRD cruciform coupler, the isolation port is exactly opposite to the input port. In other words, the isolation between them is very high, because the longitudinal component of the LSM_{10} mode must be null at the metal image plane. This fact was again used to design an iSINRD magic-T circuit, by simply extending the length of one of the output arms by quarter a wavelength. Therefore, an operation identical to that of rectangular waveguide is obtained, in which the outputs of the opposite input ports are either in-phase or out-of-phase, while signals

simultaneously fed to two input ports do not travel to the other port. Therefore, the iSINRD magic-T has very high isolation compared to a standard T-junction. Measurement results of the fabricated iSINRD magic-T verified this hypothesis. Neither the cruciform coupler nor the cruciform magic-T requires inductive posts or reflecting mirrors that otherwise required by traditional cruciform circuits.

Another investigated cruciform circuit, which also utilizes the mode richness of the iSINRD guide, is the ortho-mode transducer involving the orthogonal LSM_{10} and TE_{20} modes. This iSINRD OMT is based on the narrow-band acute angle class of OMTs. However, unlike all other OMT types, it does not require septa or tapering of any of its dimensions. More importantly, it is completely planar and features high isolation. This is a big advantage over standard OMT types that require septa or dimensional adjustments, which are very hard to conceive at W-band frequencies. Very good measurement results of this OMT were obtained at 94 GHz with little deviation from the simulation.

This work presented a unique collection of iSINRD circuits at the W-band frequencies. The satisfactory measurements obtained provide strong evidence to support the argument of replacing the SIW as an alternative waveguide at milometer and sub-millimeter wavelengths. However, due to limitations of the MHMIC fabrication technology, the full potential of the iSINRD guide could not be explored. Therefore, for future versatile realisations of the iSINRD circuits, an alternative to the MHMIC fabrication technology, for example the LTCC technology, ought to be sought. Furthermore, an alternative excitation method suitable for the W-band must be devised to replace the bulky WR10 feeding structure.

Once the fabrication issues are addressed, it is then anticipated that the iSINRD guide can be instrumental in the design of some active circuits such as balanced mixers and power amplifiers. These active circuits would make use of the passive components developed in this work, especially the magic-T and 180^{o} hybrid. Other relevant work includes multi-layer implementations of the iSINRD guide, integration with CPW and microstrip transmission lines, and hybrid implementation with the SIIG; to name a few. The quest to higher frequencies, like terahertz (THz), is naturally on the agenda, motivated by the simplified design procedure presented in this work, which is scalable to any frequency and the agility of the iSINRD guide at upper end millimeter wave frequencies compared to conventional waveguide or even the SIW.

BIBLIOGRAPHY

[1] F. K. Y. Lo, "ALMA and Sub-millimeter-wave Astronomy," *Infrared Millimeter Waves and 14th International Conference on Teraherz Electronics, 2006. IRMMW-THz 2006. Joint 31st International Conference on*. p. 3, 2006.

[2] S. G. C., "Hyper-frequency Waveguides - General Considerations and Experimental Results," *Bell Systems Technical Journal*, vol. 15, pp. 284–309, 1936.

[3] S. A. Carrson, J. R, Mead, S. P., Schelkunoff, "Hyper-frequency Waveguides - Mathematical Theory," *Bell Systems Technical Journal*, vol. 15, pp. 310–330, 1936.

[4] C. A. Balanis, *Advanced Engineering Electromagnetics*, Second. Wiley, 2012.

[5] C. H. Chandler, "An Investigation of Dielectric Rod as Waveguide," *Journal of Applied Physics*, vol. 20, pp. 1188–1192, 1949.

[6] T. Yoneyama, "Millimeter-wave integrated circuits using nonradiative dielectric waveguide," *Electronics and Communications in Japan (Part II: Electronics)*, vol. 74, no. 2, pp. 20–28, 1991.

[7] F. J. Tischer, "A waveguide structure with low losses," *Archive der Elektrischen Ubertragung*, vol. 7, pp. 592–596, 1953.

[8] F. J. Tischer, "H Guide with Laminated Dielectric Slab," *Microwave Theory and Techniques, IEEE Transactions on*, vol. 18, no. 1. pp. 9–15, 1970.

[9] K. Wu, D. Deslandes, and Y. Cassivi, "The substrate integrated circuits - a new concept for high-frequency electronics and optoelectronics," *Telecommunications in Modern Satellite, Cable and Broadcasting Service, 2003. TELSIKS 2003. 6th International Conference on*, vol. 1. p. P–III–P–X vol.1, 2003.

[10] K. Patrovsky, A., Wu, "Substrate integrated circuits (SICs)—providing a low-cost and low-loss approach for millimeter-wave circuit and system integration

(invited paper)," in *8th MINT Millimeter-Wave Int. Symp. and 9th Topical Symp. on Millimeter Waves*, 2007, pp. 9–14.

[11] K. Wu, "Towards system-on-substrate approach for future millimeter-wave and photonic wireless applications," *Microwave Conference, 2006. APMC 2006. Asia-Pacific*. pp. 1895–1900, 2006.

[12] K. Wu, "Integration and interconnect techniques of planar and non-planar structures for microwave and millimeter-wave circuits - current status and future trend," *Microwave Conference, 2001. APMC 2001. 2001 Asia-Pacific*, vol. 2. pp. 411–416 vol.2, 2001.

[13] D. Deslandes and K. Wu, "Integrated microstrip and rectangular waveguide in planar form," *Microwave and Wireless Components Letters, IEEE*, vol. 11, no. 2. pp. 68–70, 2001.

[14] F. Xu, Y. Zhang, W. Hong, K. Wu, and T. J. Cui, "Finite-difference frequency-domain algorithm for modeling guided-wave properties of substrate integrated waveguide," *Microwave Theory and Techniques, IEEE Transactions on*, vol. 51, no. 11. pp. 2221–2227, 2003.

[15] F. Xu, K. Wu, and W. Hong, "Equivalent Resonant Cavity Model of Arbitrary Periodic Guided-Wave Structures and Its Application to Finite-Difference Frequency-Domain Algorithm," *Microwave Theory and Techniques, IEEE Transactions on*, vol. 55, no. 4. pp. 697–702, 2007.

[16] L. Yan, W. Hong, K. Wu, and T. J. Cui, "Investigations on the propagation characteristics of the substrate integrated waveguide based on the method of lines," *Microwaves, Antennas and Propagation, IEE Proceedings*, vol. 152, no. 1. pp. 35–42, 2005.

[17] W. Hong, B. Liu, Y. Wang, Q. Lai, H. Tang, X. X. Yin, Y. D. Dong, Y. Zhang, and K. Wu, "Half Mode Substrate Integrated Waveguide: A New Guided Wave Structure for Microwave and Millimeter Wave Application," *Infrared Millimeter Waves and 14th International Conference on Teraherz Electronics, 2006. IRMMW-THz 2006. Joint 31st International Conference on*. p. 219, 2006.

[18] B. Liu, W. Hong, Y.-Q. Wang, Q.-H. Lai, and K. Wu, "Half Mode Substrate Integrated Waveguide (HMSIW) 3-dB Coupler," *Microwave and Wireless Components Letters, IEEE*, vol. 17, no. 1. pp. 22–24, 2007.

[19] B. Liu, W. Hong, Y. Zhang, H. J. Tang, X. Yin, and K. Wu, “Half Mode Substrate Integrated Waveguide 180° 3-dB Directional Couplers,” *Microwave Theory and Techniques, IEEE Transactions on*, vol. 55, no. 12. pp. 2586–2592, 2007.

[20] Y. Cheng, W. Hong, and K. Wu, “Half Mode Substrate Integrated Waveguide (HMSIW) Directional Filter,” *Microwave and Wireless Components Letters, IEEE*, vol. 17, no. 7. pp. 504–506, 2007.

[21] Y. Wang, W. Hong, Y. Dong, B. Liu, H. J. Tang, J. Chen, X. Yin, and K. Wu, “Half Mode Substrate Integrated Waveguide (HMSIW) Bandpass Filter,” *Microwave and Wireless Components Letters, IEEE*, vol. 17, no. 4. pp. 265–267, 2007.

[22] J. Xu, W. Hong, H. Tang, Z. Kuai, and K. Wu, “Half-Mode Substrate Integrated Waveguide (HMSIW) Leaky-Wave Antenna for Millimeter-Wave Applications,” *Antennas and Wireless Propagation Letters, IEEE*, vol. 7. pp. 85–88, 2008.

[23] Y. D. Dong, W. Hong, Z. Q. Kuai, C. Yu, Y. Zhang, J. Y. Zhou, and J.-X. Chen, “Development of Ultrawideband Antenna With Multiple Band-Notched Characteristics Using Half Mode Substrate Integrated Waveguide Cavity Technology,” *Antennas and Propagation, IEEE Transactions on*, vol. 56, no. 9. pp. 2894–2902, 2008.

[24] G. H. Zhai, W. Hong, K. Wu, J. X. Chen, P. Chen, J. Wei, and H. J. Tang, “Folded Half Mode Substrate Integrated Waveguide 3 dB Coupler,” *Microwave and Wireless Components Letters, IEEE*, vol. 18, no. 8. pp. 512–514, 2008.

[25] N. Grigoropoulos, B. Sanz-Izquierdo, and P. R. Young, “Substrate integrated folded waveguides (SIFW) and filters,” *Microwave and Wireless Components Letters, IEEE*, vol. 15, no. 12. pp. 829–831, 2005.

[26] W. Che, L. Geng, K. Deng, and Y. L. Chow, “Analysis and Experiments of Compact Folded Substrate-Integrated Waveguide,” *Microwave Theory and Techniques, IEEE Transactions on*, vol. 56, no. 1. pp. 88–93, 2008.

[27] Y. Ding and K. Wu, “A 4 × 4 Ridge Substrate Integrated Waveguide (RSIW) Slot Array Antenna,” *Antennas and Wireless Propagation Letters, IEEE*, vol. 8. pp. 561–564, 2009.

[28] A. Patrovsky and K. Wu, “Substrate integrated image guide (SIIG) - a low-loss waveguide for millimetre-wave applications,” *Microwave Conference, 2005 European*, vol. 2. p. 4 pp., 2005.

[29] Y. Cassivi and K. Wu, “Substrate integrated nonradiative dielectric waveguide,” *Microwave and Wireless Components Letters, IEEE*, vol. 14, no. 3. pp. 89–91, 2004.

[30] Y. Cassivi and K. Wu, “Substrate integrated circuits concept applied to the nonradiative dielectric guide,” *Microwaves, Antennas and Propagation, IEE Proceedings*. pp. 424–433, 2005.

[31] Y. Sugawara, N. Nakaminami, N. Ishii, and K. Ito, “A proposal of image NRD waveguide and radiation from its end,” *Electronics and Communications in Japan (Part I: Communications)*, vol. 84, no. 3, pp. 56–64, 2001.

[32] J. L. Gomez-Tornero, J. Pascual-Garcia, and A. Alvarez-Melcon, “A novel leaky-wave antenna combining an image NRD guide and a strip circuit,” *Antennas and Wireless Propagation Letters, IEEE*, vol. 4. pp. 289–292, 2005.

[33] S. A. Yahaya, M. Yamamoto, K. Itoh, and T. Nojima, “Dielectric rod antenna based on image NRD guide coupled to rectangular waveguide,” *Electronics Letters*, vol. 39, no. 15. pp. 1099–1101, 2003.

[34] T. Yoneyama, H. Tamaki, and S. Nishida, “Analysis and Measurements of Nonradiative Dielectric Waveguide Bends,” *Microwave Symposium Digest, 1986 IEEE MTT-S International*. pp. 115–117, 1986.

[35] T. Yoneyama, H. Tamaki, and S. Nishida, “Analysis and Measurements of Nonradiative Dielectric Waveguide Bends,” *Microwave Theory and Techniques, IEEE Transactions on*, vol. 34, no. 8. pp. 876–882, 1986.

[36] T. Yoneyama, M. Yamaguchi, and S. Nishida, “Bends in Nonradiative Dielectric Waveguides,” *Microwave Theory and Techniques, IEEE Transactions on*, vol. 30, no. 12. pp. 2146–2150, 1982.

[37] T. Yoneyama, S. Nishida, and M. Yamaguchi, “Bends in Nonradiative Dielectric Waveguides,” *Microwave Symposium Digest, 1982 IEEE MTT-S International*. pp. 300–301, 1982.

[38] D. Li, Y. Cassivi, P. Yang, and K. Wu, "Analysis and Design of Bridged NRD-Guide Coupler for Millimeter-Wave Applications," *Microwave Theory and Techniques, IEEE Transactions on*, vol. 53, no. 8. pp. 2546–2551, 2005.

[39] Y. Cassivi and K. Wu, "Magic Tee Junction Based on Hybrid Architecture of Microstrip Line and Non-Radiative Dielectric Waveguide," *Microwave Conference, 2001. 31st European*. pp. 1–4, 2001.

[40] U. Schmid and W. Menzel, "Planar antenna arrays using a feed network with nonradiative dielectric (NRD) waveguide," *Antennas and Propagation, 2006. EuCAP 2006. First European Conference on*. pp. 1–4, 2006.

[41] U. Schmid, W. Menzel, Y. Cassivi, and K. Wu, "Dual polarization antenna fed by a dual mode substrate integrated NRD-guide," *Antennas and Propagation Society International Symposium, 2004. IEEE*, vol. 4. pp. 4348–4351 Vol.4, 2004.

[42] M. Wong, A. R. Sebak, and T. A. Denidni, "Wideband Bezier curve shaped microstrip to H-guide transition," *Electronics Letters*, vol. 45, no. 24. pp. 1250–1252, 2009.

[43] S. K. Koul, *Millimeter wave and optical dielectric integrated guides and circuits*. John Wiley & Sons, 1997.

[44] R. E. Collin, *Field theory of guided waves*. IEEE Press, 1991.

[45] P. Bhartia and I. J. Bahl, *Millimeter wave engineering and applications*. Wiley, 1984.

[46] F. J. Tischer and M. Cohn, "Attenuation of the HE_{11} Mode in the H-Guide (Correspondence and Author's Reply)," *Microwave Theory and Techniques, IRE Transactions on*, vol. 7, no. 4. pp. 478–480, 1959.

[47] Y. Cassivi, "Etude et Development de la Technologie Hybride Circuit Planaire/Guide NRD dans le Contexte d'un Emetteur/Recepteur Onde Millimetrique," Ecole Polytechnique de Montreal, 2004.

[48] D. M. Pozar, *Microwave engineering*. Wiley, 1997.

[49] W. Menzel and J. Al-Attari, “Suspended Stripline Filters Integrated with Standard Multilayer Printed Circuit Boards,” *German Microwave Conference, 2009*. pp. 1–4, 2009.

[50] J. Tang and K. Wu, “Integrated microstrip to NRD-guide transition using a spurious mode suppressing technique,” *Microwave Symposium Digest. 2000 IEEE MTT-S International*, vol. 3. pp. 1805–1808 vol.3, 2000.

[51] ANSYS and Inc., “Ansys HFSS.” Cannonsburg, PA, 2011.

[52] CST, “Microwave Studio.” Darmstadt, Germany, 2006.

[53] C. A. Balanis, “Measurements of Dielectric Constants and Loss Tangents at E-band using a Fabry-Perot Interferometer,” *NASA Technical Note*, no. NASA TN D-5583, 1969.

[54] P. H. Bolivar, M. Brucherseifer, J. G. Rivas, R. Gonzalo, I. Ederra, A. L. Reynolds, M. Holker, and P. de Maagt, “Measurement of the dielectric constant and loss tangent of high dielectric-constant materials at terahertz frequencies,” *Microwave Theory and Techniques, IEEE Transactions on*, vol. 51, no. 4. pp. 1062–1066, 2003.

[55] M. N. Afsar, “Dielectric Measurements of Millimeter-Wave Materials,” *Microwave Theory and Techniques, IEEE Transactions on*, vol. 32, no. 12. pp. 1598–1609, 1984.

[56] M. N. Afsar, I. I. Tkachov, and K. N. Kocharyan, “A novel W-band spectrometer for dielectric measurements,” *Microwave Symposium Digest. 2000 IEEE MTT-S International*, vol. 3. pp. 1627–1630 vol.3, 2000.

[57] M. N. Afsar, I. I. Tkachov, and K. N. Kocharyan, “A novel W-band spectrometer for dielectric measurements,” *Microwave Theory and Techniques, IEEE Transactions on*, vol. 48, no. 12. pp. 2637–2643, 2000.

[58] M. N. Afsar, I. I. Tkachov, and K. Kocharyan, “A W-band spectrometer for precision dielectric measurements,” *Precision Electromagnetic Measurements Digest, 2000 Conference on*. pp. 500–501, 2000.

[59] M. N. Afsar, “Precision millimeter-wave dielectric measurements of birefringent crystalline sapphire and ceramic alumina,” *Instrumentation and Measurement, IEEE Transactions on*, vol. IM–36, no. 2. pp. 554–559, 1987.

[60] R. Corporation, “Rogers Corporation High Frequency Materials Product Selector Guide,” Chandler, Arizona, 2011.

[61] A. Patrovsky, “Hybrid Integration of Synthesized Dielectric Image Waveguides in Substrate Integrated Circuit Technology and its Millimeter Wave Applications,” Ecole Polytechnique de Montreal, 2008.

[62] Mathworks, “MATLAB.” MA, US, 2012.

[63] J. Gauthier, S. Dube, and T. Antonescu, “PCB Fabrication rule,” *Polygrames Research Center Internal Document*.

[64] F. Xu and K. Wu, “Substrate Integrated Nonradiative Dielectric Waveguide Structures Directly Fabricated on Printed Circuit Boards and Metallized Dielectric Layers,” *Microwave Theory and Techniques, IEEE Transactions on*, vol. 59, no. 12. pp. 3076–3086, 2011.

[65] F. Xu, A. Patrovsky, and K. Wu, “Fast simulation of periodic guided-wave structures based on commercial software,” *Microwave and Optical Technology Letters*, vol. 49, no. 9, pp. 2180–2182, 2007.

[66] E. Moldovan, R. G. Bosisio, and K. Wu, “W-band multiport substrate-integrated waveguide circuits,” *Microwave Theory and Techniques, IEEE Transactions on*, vol. 54, no. 2. pp. 625–632, 2006.

[67] S. E. Miller, “Coupled wave theory and waveguide applications,” *Bell Systems Technical Journal*, vol. 33, pp. 661–719, 1954.

[68] A. Ishimaru, *Electromagnetic Wave Propagation, Radiation, and Scattering*. Prentice Hall, 1991.

[69] A. Patrovsky, M. Daigle, and K. Wu, “Coupling Mechanism in Hybrid SIW-CPW Forward Couplers for Millimeter-Wave Substrate Integrated Circuits,” *Microwave Theory and Techniques, IEEE Transactions on*, vol. 56, no. 11. pp. 2594–2601, 2008.

[70] P. K. Ikalainen and G. L. Matthaei, “Design of Broad-Band Dielectric Waveguide 3-dB Couplers,” *Microwave Theory and Techniques, IEEE Transactions on*, vol. 35, no. 7. pp. 621–628, 1987.

[71] C.-Y. Huang and C.-W. Ling, “CPW feed circularly polarised microstrip antenna using asymmetric coupling slot,” *Electronics Letters*, vol. 39, no. 23. pp. 1627–1628, 2003.

[72] L. O. Wilson and F. K. Reinhart, “Coupling of nearly degenerate modes in parallel asymmetric dielectric waveguides,” *Bell Systems Technical Journal*, vol. 53, pp. 717–739, 1974.

[73] D. Deslandes and K. Wu, “Accurate modeling, wave mechanisms, and design considerations of a substrate integrated waveguide,” *Microwave Theory and Techniques, IEEE Transactions on*, vol. 54, no. 6. pp. 2516–2526, 2006.

[74] M. Bozzi, F. Xu, D. Deslandes, and K. Wu, “Modeling and Design Considerations for Substrate Integrated Waveguide Circuits and Components,” *Telecommunications in Modern Satellite, Cable and Broadcasting Services, 2007. TELSIKS 2007. 8th International Conference on*. p. P–VII–P–XVI, 2007.

[75] J. J. Taub and J. Cohen, “Quasi-optical waveguide filters for millimeter and submillimeter wavelengths,” *Proceedings of the IEEE*, vol. 54, no. 4. pp. 647–656, 1966.

[76] B. Wardrop, “Analysis of quasioptical waveguide corners,” *Electronics Letters*, vol. 6, no. 6. pp. 154–155, 1970.

[77] J. J. Campbell, “Application of the Solutions of Certain Boundary Value Problems to the Symmetrical Four-Port Junction and Specially Truncated Bends in Parallel-Plate Waveguides and Balanced Strip-Transmission Lines,” *Microwave Theory and Techniques, IEEE Transactions on*, vol. 16, no. 3. pp. 165–176, 1968.

[78] Fanfan He, “Innovative Microwave and Millimetre-Wave Components and Sub-Systems Based on Substrate Integration Technology,” Ecole Polytechnique de Montreal, 2008.

[79] L. Han, K. Wu, and S. Winkler, “Singly balanced mixer using substrate integrated waveguide magic-T structure,” *Wireless Technology, 2008. EuWiT 2008. European Conference on*. pp. 9–12, 2008.

[80] F. C. de Ronde, “A New Class of Microstrip Directional Couplers,” *Microwave Symposium, G-MTT 1970 International*. pp. 184–189, 1970.

[81] G. J. Laughlin, “A New Impedance-Matched Wide-Band Balun and Magic Tee,” *Microwave Theory and Techniques, IEEE Transactions on*, vol. 24, no. 3. pp. 135–141, 1976.

[82] C.-H. Ho, L. Fan, and K. Chang, “New uniplanar coplanar waveguide hybrid-ring couplers and magic-T’s ,” *Microwave Theory and Techniques, IEEE Transactions on*, vol. 42, no. 12. pp. 2440–2448, 1994.

[83] J. P. Kim and W. S. Park, “Novel configurations of planar multilayer magic-T using microstrip-slotline transitions,” *Microwave Theory and Techniques, IEEE Transactions on*, vol. 50, no. 7. pp. 1683–1688, 2002.

[84] M. Aikawa and H. Ogawa, “A New MIC Magic-T Using Coupled Slot Lines,” *Microwave Theory and Techniques, IEEE Transactions on*, vol. 28, no. 6. pp. 523–528, 1980.

[85] T. Hiraoka, T. Tokumitsu, and M. Aikawa, “Very small wide-band MMIC magic T’s using microstrip lines on a thin dielectric film,” *Microwave Theory and Techniques, IEEE Transactions on*, vol. 37, no. 10. pp. 1569–1575, 1989.

[86] M. Davidovitz, “A compact planar magic-T junction with aperture-coupled difference port,” *Microwave and Guided Wave Letters, IEEE*, vol. 7, no. 8. pp. 217–218, 1997.

[87] M. W. Katsube, Y. M. M. Antar, A. Ittipiboon, and M. Cuhaci, “A novel aperture coupled microstrip ‘magic-T’,” *Microwave and Guided Wave Letters, IEEE*, vol. 2, no. 6. pp. 245–246, 1992.

[88] T.-M. Shen, T.-Y. Huang, and R.-B. Wu, “A laminated waveguide magic-T in multilayer LTCC,” *Microwave Symposium Digest, 2009. MTT ’09. IEEE MTT-S International*. pp. 713–716, 2009.

[89] T.-M. Shen, T.-Y. Huang, C.-F. Chen, and R.-B. Wu, “A Laminated Waveguide Magic-T With Bandpass Filter Response in Multilayer LTCC,” *Microwave Theory and Techniques, IEEE Transactions on*, vol. 59, no. 3. pp. 584–592, 2011.

[90] W. Feng, W. Che, and K. Deng, “Compact Planar Magic-T Using E-Plane Substrate Integrated Waveguide (SIW) Power Divider and Slotline Transition,” *Microwave and Wireless Components Letters, IEEE*, vol. 20, no. 6. pp. 331–333, 2010.

[91] F. He, K. Wu, X. Chen, L. Han, and W. Hong, “A planar magic-T structure using substrate integrated circuits concept,” *Microwave Symposium Digest (MTT), 2010 IEEE MTT-S International*. p. 1, 2010.

[92] F. F. He, K. Wu, W. Hong, L. Han, and X. Chen, “A Planar Magic-T Structure Using Substrate Integrated Circuits Concept and Its Mixer Applications,” *Microwave Theory and Techniques, IEEE Transactions on*, vol. 59, no. 1. pp. 72–79, 2011.

[93] W. Feng, W. Che, and T. F. Eibert, “Compact planar magic-T using half mode substrate integrated waveguide and slotline coupling,” *Microwave Symposium Digest (MTT), 2011 IEEE MTT-S International*. pp. 1–4, 2011.

[94] F. F. He, K. Wu, W. Hong, H. J. Tang, H. B. Zhu, and J. X. Chen, “A Planar Magic-T Using Substrate Integrated Circuits Concept,” *Microwave and Wireless Components Letters, IEEE*, vol. 18, no. 6. pp. 386–388, 2008.

[95] J. Uher, J. Bornemann, and U. Rosenberg, *Waveguide components for antenna feed systems: theory and CAD*. Artech House, 1993.

[96] A. Navarrini and R. Nesti, “Symmetric Reverse-Coupling Waveguide Orthomode Transducer for the 3-mm Band,” *Microwave Theory and Techniques, IEEE Transactions on*, vol. 57, no. 1. pp. 80–88, 2009.

[97] G. Chattopadhyay, B. Philhour, J. E. Carlstrom, S. Church, A. Lange, and J. Zmuidzinas, “A 96-GHz ortho-mode transducer for the Polatron,” *Microwave and Guided Wave Letters, IEEE*, vol. 8, no. 12. pp. 421–423, 1998.

[98] S. B. Sharma, V. K. Singh, and S. Chakrabarty, “Multifrequency Waveguide Orthomode Transducer,” *Microwave Theory and Techniques, IEEE Transactions on*, vol. 53, no. 8. pp. 2604–2609, 2005.

[99] Y. Tao, Z. Shen, and G. Liu, “Closed-Form Expressions for the Equivalent Circuit Model of Square-Waveguide T-Junctions and Its Application in Ortho-Mode Transducer Design,” *Microwave Theory and Techniques, IEEE Transactions on*, vol. 58, no. 5. pp. 1167–1174, 2010.

[100] Y. Tao, Z. Shen, and G. Liu, “Equivalent circuit model of square waveguide T-junction for ortho-mode transducers,” *Microwave Symposium Digest, 2009. MTT ’09. IEEE MTT-S International*. pp. 1013–1016, 2009.

[101] Jawad Attari, Tarek Djerafi and Ke Wu, “Fast and Accurate Simulation of Novel Millimeter-Wave Circuits Based on Commercial Software Package,” *IEEE Microwave Magazine,* vol. 14, no. 2, pp. 106-111, 2013.

ANNEX 1 – Field Equations of TE_{mn}^{x} and TM_{mn}^{x} Modes in the NRD Guide

Symmetric TM_{mn}^{x} modes:

$Region\ 1,\ \varepsilon_{r1}\ (x\ <|b/2|)$

$$E_x = (A/\varepsilon_r)p^2 \sin(m\pi y/a)\cos(\beta_x x) \quad (1.1m)$$

$$E_y = -A(\beta_x/\varepsilon_r)(m\pi/a)\cos(m\pi y/a)\sin(\beta_x x) \quad (1.1\ n)$$

$$E_z = j(A/\varepsilon_r)\beta\beta_x \sin(m\pi y/a)\sin(\beta_x x) \quad (1.1\ o)$$

$$H_x = 0 \quad (1.1\ p)$$

$$H_y = -A\omega\varepsilon_0\beta \sin(m\pi y/a)\cos(\beta_x x) \quad (1.1\ q)$$

$$H_z = jA\omega\varepsilon_0(m\pi/a)\cos(m\pi y/a)\cos(\beta_x x) \quad (1.1\ r)$$

$Region\ 2,\ \varepsilon_{r2}\ (x\ >|\ b/2\ |)$

$$E_x = Ap^2 \sin(m\pi y/a)\cos(\beta_x\, b/2)e^{\varphi(b/2-|x|)} \quad (1.1\ s)$$

$$E_y = \mp A\varphi(m\pi/a)\cos(m\pi y/a)\cos(\beta_x\, b/2)e^{\varphi(b/2-|x|)} \quad (1.1\ t)$$

$$E_z = \pm jA\beta\varphi \sin(m\pi y/a)\cos(\beta_x\, b/2)e^{\varphi(b/2-|x|)} \quad (1.1\ u)$$

$$H_x = 0 \quad (1.1\ v)$$

$$H_y = -A\omega\varepsilon_0\beta\sin(m\pi y/a)\cos(\beta_x\, b/2)e^{\varphi(b/2-|x|)} \quad (1.1w)$$

$$H_z = jA\omega\varepsilon_0(m\pi/a)\cos(m\pi y/a)\cos(\beta_x\, b/2)e^{\varphi(b/2-|x|)} \quad (1.1\ x)$$

Asymmetric TM_{mn}^{x} modes:

$Region\ 1,\ \varepsilon_{r1}\ (x\ <|b/2|)$

$$E_x = (B/\varepsilon_r)p^2 \sin(m\pi y/a)\sin(\beta_x x) \quad (1.2\ m)$$

$$E_y = B(\beta_x/\varepsilon_r)(m\pi/a)\cos(m\pi y/a)\cos(\beta_x x) \quad (1.2\ n)$$

$$E_z = -j(B/\varepsilon_r)\beta\beta_x \sin(m\pi y/a)\cos(\beta_x x) \quad (1.2\ o)$$

$$H_x = 0 \quad (1.2\text{ p})$$

$$H_y = -B\omega\varepsilon_0\beta \sin(m\pi y/a)\sin(\beta_x x) \quad (1.2\text{ q})$$

$$H_z = jB\omega\varepsilon_0(m\pi/a)\cos(m\pi y/a)\sin(\beta_x x) \quad (1.2\text{ r})$$

$Region\ 2,\ \varepsilon_{r2}\ (x > |b/2|)$

$$E_x = \pm Bp^2 \sin(m\pi y/a)\sin(\beta_x b/2)e^{\varphi(b/2-|x|)} \quad (1.2\text{ s})$$

$$E_y = -B\varphi(m\pi/a)\cos(m\pi y/a)\sin(\beta_x b/2)e^{\varphi(b/2-|x|)} \quad (1.2\text{ t})$$

$$E_z = jB\beta\varphi \sin(m\pi y/a)\sin(\beta_x b/2)e^{\varphi(b/2-|x|)} \quad (1.2\text{ u})$$

$$H_x = 0 \quad (1.2\text{ v})$$

$$H_y = \mp B\omega\varepsilon_0\beta\sin(m\pi y/a)\sin(\beta_x b/2)e^{\varphi(b/2-|x|)} \quad (1.2\text{ w})$$

$$H_z = \pm jB\omega\varepsilon_0(m\pi/a)\cos(m\pi y/a)\sin(\beta_x b/2)e^{\varphi(b/2-|x|)} \quad (1.2\text{ x})$$

Symmetric TE^x_{mn} modes:

$Region\ 1,\ \varepsilon_{r1}\ (x < |b/2|)$

$$E_x = 0 \quad (1.3\text{m})$$

$$E_y = C\omega\mu_0\beta \cos(m\pi y/a)\cos(\beta_x x) \quad (1.3\text{ n})$$

$$E_z = jC\omega\mu_0(m\pi y/a)\sin(m\pi y/a)\cos(\beta_x x) \quad (1.3\text{ o})$$

$$H_x = Cp^2 \cos(m\pi y/a)\cos(\beta_x x) \quad (1.3\text{ p})$$

$$H_y = C\beta_y(m\pi y/a)\sin(m\pi y/a)\sin(\beta_x x) \quad (1.3\text{ q})$$

$$H_z = jC\beta\beta_x \cos(m\pi y/a)\sin(\beta_x x) \quad (1.3\text{ r})$$

$Region\ 2,\ \varepsilon_{r2}\ (x > |b/2|)$

$$E_x = 0 \quad (1.3\text{ s})$$

$$E_y = C\omega\mu_0\beta \cos(m\pi y/a)\cos(\beta_x b/2)\, e^{\varphi(b/2-|x|)} \quad (1.3\text{ t})$$

$$E_z = jC\omega\mu_0(m\pi y/a)\sin(m\pi y/a)\cos(\beta_x b/2)\, e^{\varphi(b/2-|x|)} \quad (1.3\text{ u})$$

$$H_x = Cp^2\cos(m\pi y/a)\cos(\beta_x b/2)e^{\varphi(b/2-|x|)} \quad (1.3\text{ v})$$

$$H_y = \pm C\varphi(m\pi y/a)\sin(m\pi y/a)\cos(\beta_x b/2)\, e^{\varphi(b/2-|x|)} \quad (1.3\text{ w})$$

$$H_z = \pm jC\beta\varphi\cos(m\pi y/a)\cos(\beta_x b/2)\, e^{\varphi(b/2-|x|)} \quad (1.3\text{ x})$$

Asymmetric TE^x_{mn} modes:

$Region\ 1,\ \varepsilon_{r1}\ (x < |b/2|)$

$$E_x = 0 \quad (1.4\text{ m})$$

$$E_y = D\omega\mu_0\beta\cos(m\pi y/a)\sin(\beta_x x) \quad (1.4\text{ n})$$

$$E_z = jD\omega\mu_0(m\pi y/a)\sin(m\pi y/a)\sin(\beta_x x) \quad (1.4\text{ o})$$

$$H_x = Dp^2\cos(m\pi y/a)\sin(\beta_x x) \quad (1.4\text{ p})$$

$$H_y = -D\beta_x(m\pi y/a)\sin(m\pi y/a)\cos(\beta_x x) \quad (1.4\text{ q})$$

$$H_z = -jD\beta\beta_x\cos(m\pi y/a)\sin(\beta_x x) \quad (1.4\text{ r})$$

$Region\ 2,\ \varepsilon_{r2}\ (x > |b/2|)$

$$E_x = 0 \quad (1.4\text{ s})$$

$$E_y = \pm D\omega\mu_0\beta\cos(m\pi y/a)\sin(\beta_x b/2)\, e^{\varphi(b/2-|x|)} \quad (1.4\text{ t})$$

$$E_z = \pm jD\omega\mu_0(m\pi y/a)\sin(m\pi y/a)\sin(\beta_x b/2)\, e^{\varphi(b/2-|x|)} \quad (1.4\text{ u})$$

$$H_x = \pm Dp^2\cos(m\pi y/a)\sin(\beta_x b/2)e^{\varphi(b/2-|x|)} \quad (1.4\text{ v})$$

$$H_y = D\varphi(m\pi y/a)\sin(m\pi y/a)\sin(\beta_x b/2)\, e^{\varphi(b/2-|x|)} \quad (1.4\text{w})$$

$$H_z = jD\beta\varphi\cos(m\pi y/a)\sin(\beta_x b/2)\, e^{\varphi(b/2-|x|)} \quad (1.4\text{ x})$$

ANNEX 2 – Field Plots for Circular-via iSINRD guide

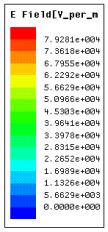

At f_c = 84 GHz, no propagation

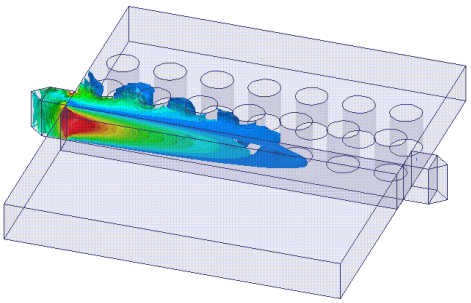

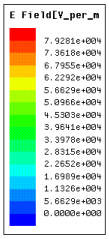

At f_g = 94 GHz, propagation of the LSM_{10} mode without leakage into the side region

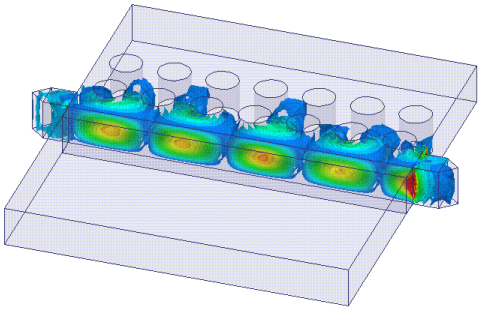

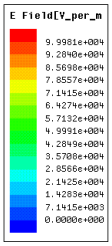

At f_x = 102.5 GHz, leakage into the perforated region is evident

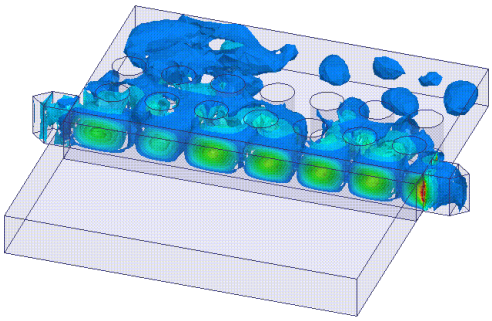

ANNEX 3 – Field Plots for Square-via iSINRD guide

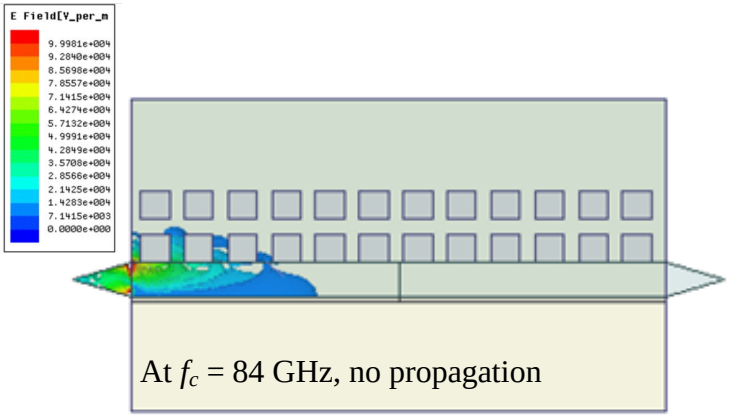

At f_c = 84 GHz, no propagation

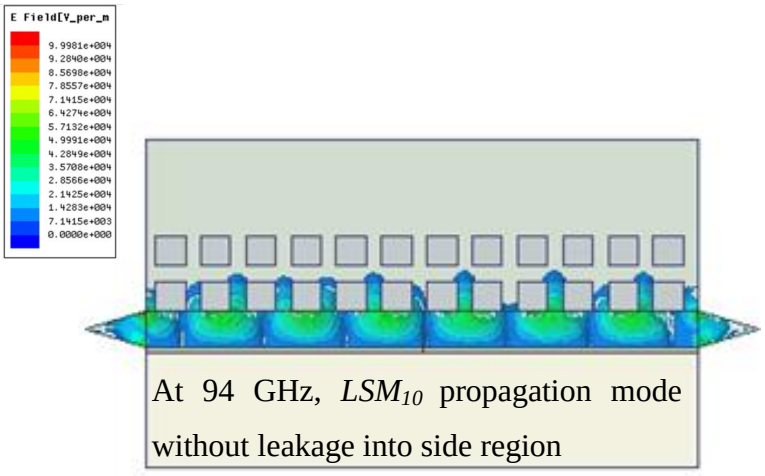

At 94 GHz, LSM_{10} propagation mode without leakage into side region

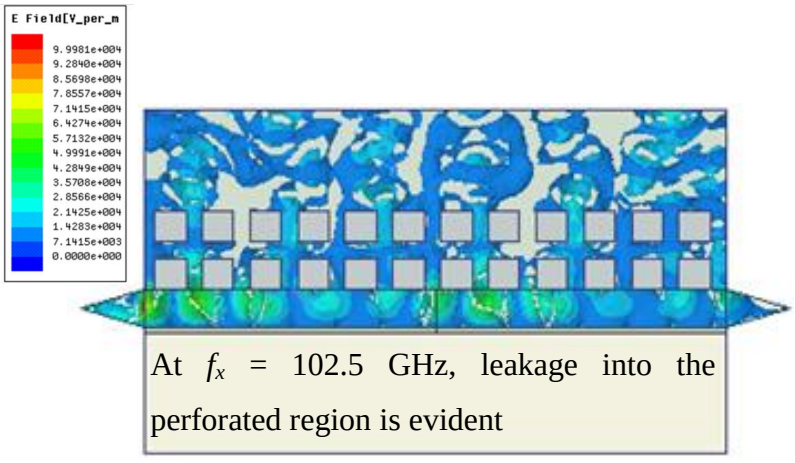

At f_x = 102.5 GHz, leakage into the perforated region is evident

ANNEX 4 – Dielectric Loss in the iSINRD Guide

Incident Power (LSM_{10})

$$P_{SINRD} = \int_{-\infty}^{+\infty}\int_{0}^{a} E_y H_x^* dydx$$

$$P_{iSINRD} = \int_{0}^{+\infty}\int_{0}^{a} E_y H_x^* dydx$$

$$P_{iSINRD} = P_{SINRD}/2$$

Dissipated Power (dielectric)

$$P_{dS} = 2\omega\varepsilon_{r1}\tan\delta_1\int_0^{b/2}\int_0^a \left|\vec{E_1}\right|^2 dydx + 2\omega\varepsilon_{r2}\tan\delta_2\int_{b/2}^{\infty}\int_0^a \left|\vec{E_2}\right|^2 dydx$$

$$P_{dS} = 2\omega\left[\varepsilon_{r1}\tan\delta_1\int_0^{b/2}\int_0^a \left|\vec{E_1}\right|^2 dydx + \varepsilon_{r2}\tan\delta_2\int_{b/2}^{\infty}\int_0^a \left|\vec{E_2}\right|^2 dydx\right]$$

$$P_{di} = \omega\left[\varepsilon_{r1}\tan\delta_1\int_0^{b/2}\int_0^a \left|\vec{E_1}\right|^2 dydx + \varepsilon_{r2}\tan\delta_2\int_{b/2}^{\infty}\int_0^a \left|\vec{E_2}\right|^2 dydx\right]$$

$$P_{di} = P_{dS}/2$$

$$\alpha_{dS}\cdot l = \frac{P_{dS}}{2P_{SINRD}}$$

$$\alpha_{di}\cdot l = \frac{P_{di}}{2P_{iSINRD}} = \frac{P_{dS}/2}{2\,P_{SINRD}/2} = \frac{P_{dS}}{2P_{SINRD}} = \alpha_{dS}\cdot l$$

$$\therefore \alpha_{di} = \alpha_{dS}$$